Aspects of Ocean Circulation with Finite Element Modelling

DISSERTATION
zur
Erlangung des Grades
Doktor der Naturwissenschaften
— Dr. rer. nat. —

dem Fachbereich I (Physik/Elektrotechnik) der
Universität Bremen
vorgelegt von

Sven Harig

April, 2004

1. Gutachter: Prof. Dr. D. Olbers
2. Gutachter: Prof. Dr. W. Hiller

Alfred-Wegener-Institut für Polar- und Meeresforschung

Übersicht

Diese Arbeit beschäftigt sich mit der Entwicklung und Evaluierung des dreidimensionalen, nichtstationären Ozeanmodells $FEOM_0$ (Basisversion des **F**inite **E**lement **O**cean **M**odel). Dieses Modell beruht auf der Methode der finiten Elemente, die es erlaubt, unstrukturierte Gitter zu verwenden die variable räumliche Auflösung erlauben. Weiterhin ermöglicht diese Methode eine realistische Diskretisierung der Küstenlinien und der Topographie.

Der erste Teil dieser Arbeit behandelt die Grundgleichungen, die mathematische Formulierung sowie die Diskretisierung. Das Modellgebiet wird in Tetraeder zerlegt, diese Form erlaubt eine sehr flexible Darstellung der Topographie. Als Basisfunktionen werden stückweise lineare Funktionen verwendet. Nach der diskreten Formulierung beschreibt ein Kapitel die numerische Umsetzung.

Im zweiten Teil der Arbeit werden verschiedene ozeanographische Fragestellungen unter idealisierten Bedingungen mit $FEOM_0$ untersucht. Damit können die Möglichkeiten des Modells und damit der Methode im direkten Vergleich mit analytischen Ergebnissen und Resultaten anderer Modelle in entsprechenden Experimenten bestimmt werden.

Zunächst wird die Ausbreitung von Wellen im geschichteten Ozean untersucht. Es zeigt sich eine gute Übereinstimmung mit theoretisch bestimmten Welleneigenschaften, sowie mit Modellergebnissen des Ozeanmodells MOM (Modular Ocean Model). Die zweite Anwendung ist die windgetriebene Zirkulation und insbesondere die vertikale Struktur des resultierenden Strömungsfeldes. Hier zeigen sich gute Übereinstimmung mit analytisch bestimmten Transporten und Randschichten. Der Einfluss von Topographie wird untersucht und das Modell reproduziert auch hier die Vorhersagen der linearen Theorie. Schließlich wird die Strömung von dichtem Wasser auf einer schiefen Ebene behandelt, die für numerische Modelle ein besonderes Problem darstellt. Die internationalen Vergleichstudie DOME (Dynamics of Overflow Mixing and Entrainment) vergleicht Modelle mit verschiedenen numerischen und physikalischen Ansätzen in einem idealisierten "Overflow Szenario". Dichtes Wasser wird auf eine Ebene mit konstantem Gefälle geleitet und bewegt sich sodann unter dem Einfluss der Corioliskraft in einer geschichteten oder homogenen Umgebung. Im homogenen Fall stellt sich ein zeitlich variabler Transport über die Schwelle ein, die theoretisch bestimmte Abhängigkeit des Transports von Coriolisparameter und Dichteschichtung ist erfüllt.

Abstract

This thesis is concerned with development and evaluation of the three dimensional, nonstationary ocean model $FEOM_0$ (basic version of the **F**inite **E**lement **O**cean **M**odel). This model is based on the Finite Element Method (FEM) which allows for the use of unstructured grids with variable resolution. A further advantage is the realistic representation of coast lines and topography with FEM.

The first part of the thesis introduces the governing equations, the mathematical formulation as well as the discretisation using FEM. The model domain is decomposed into tetrahedrons, a shape which allows for a realistic representation of topography. Basis functions are piece-wise linears. After introducing the discrete form of the equations some details on the numerical implementation are given.

The second part of the thesis contains applications of $FEOM_0$ to different oceanographic tasks under idealised conditions. Thereby insight is gained into the capabilities of the model in direct comparison to analytical results as well as to results of other numerical models in corresponding experiments.

The first application investigates the propagation of waves in a stratified ocean. The model shows nice correspondence to theoretically obtained wave properties as well as to results of the Modular Ocean Model (MOM). The second investigation considers the wind driven ocean circulation, especially the resulting vertical structure of the flow field. Again, the model shows nice correspondence with theoretically predicted transports and boundary layers. The influence of topography is examined, the results coincide with the predictions of linear theory. Finally an idealised overflow scenario is investigated. The flow of dense water on a slope poses a special problem for numerical ocean models. An international intercomparison study (DOME: Dynamics of Overflow Mixing and Entrainment) was conceived in order to gain insight into the capabilities of different numerical models in reproducing this process. $FEOM_0$ is applied to the idealised DOME setup with and without interior density stratification. In case of a homogeneous interior a variability in the overflow rate of several days shows up, the model gives a reasonable path of the plume and reproduces the theoretically obtained dependence of the overflow transport on Coriolis parameter and density structure. In experiments with interior stratification the plume reaches a level of neutral buoyancy.

Contents

List of symbols

Ω_E	Earth's Angular velocity
r_E	Earth's radius (6370 km)
x, y, z	Cartesian coordinates
$\boldsymbol{n}$	(outer) normal vector to the boundary of Ω
φ	Latitude (degree North: $-90°N \leqslant \varphi \leqslant 90°N$)
λ	Longitude (degree East: $-180°E \leqslant \lambda < 180°E$)
φ_0	central latitude
$f = 2\Omega_E \sin(\varphi)$	Coriolis parameter
$\boldsymbol{f} = (0, 0, f)$	Coriolis vector pointing radially outward
$f_0 = 2\Omega_E \sin(\varphi_0)$	Coriolis parameter at central latitude
$\beta = \frac{2\Omega_E}{r_E} \cos(\varphi)$	meridional derivative of Coriolis parameter
$\beta_0 = \frac{2\Omega_E}{r_E} \cos(\varphi_0)$	meridional derivative of Coriolis parameter at central latitude
$D_t = \partial_t + \boldsymbol{v} \cdot \mathbf{grad}$	substantial derivative
$\nabla\psi = (\partial_x\psi, \partial_y\psi)$	2D-gradient
$\mathbf{grad}\,\psi = (\nabla\psi, \partial_z\psi)$	3D-gradient
$\mathbf{rot}\,\boldsymbol{v}$	rotation of vector field $\boldsymbol{v}$
$\mathrm{curl}\,\boldsymbol{v} = \boldsymbol{k} \cdot \mathbf{rot}\,\boldsymbol{v}$	curl of vector field $\boldsymbol{v}$ (scalar)
Ω	Model domain
$\mathcal{T}_\Omega$	Discretisation of Omega into tetrahedrons
t_{Γ_s}	Discretisation of the surface into triangles
C^∞	Space of infinitely many times continuously differentiable functions
$L^2(\Omega)$	Space of (in Ω) square integrable functions
$H^1(\Omega)$	Sobolev space of functions $u \in L^2(\Omega)$ with weak first derivatives $Du \in L^2(\Omega)$
N	number of 3D-nodes
ν	number of 2D nodes (surface)
$\phi_n(x, y, z)$	3D piecewise linear basis function
$\psi_n(x, y)$	2D piecewise linear basis function
α	Cranc-Nicolson parameter ("implicitness" of the scheme)

Characteristics

$\mathrm{Ro} = \frac{U}{fL}$	Rossby number (ratio relative acceleration/Coriolis acceleration)
$\mathrm{Ro}_T = \frac{1}{fT}$	temporal Rossby number
$E_H = \frac{A_h}{fL^2}$	horizontal Ekman number (ratio friction/Coriolis)
$\tilde{\beta} = \frac{\beta_0 L}{f_0}$	dimensionless β-scale
$\mathrm{Re} = \frac{h\|\boldsymbol{u}\|}{A_h}$	Reynolds number (ratio of inertial and frictional forces)
$\mathrm{Pe} = \frac{h\|\boldsymbol{u}\|}{2A_h} = \mathrm{Re}/2$	Peclet number
$\mathrm{R}_{\mathrm{ext}} = \frac{\sqrt{gH}}{f}$	external Rossby Radius
$\mathrm{Fr} = \frac{U}{NH}$	Froude Number
$N^2 = -\frac{g\,\partial_z \rho}{\rho_0}$	squared Brunt-Väisälä frequency
$\mathrm{R} = \frac{NH}{f}$	(internal) Rossby deformation radius
$\mathrm{Co} = u\Delta t/\Delta x$	Courant number

Variables and properties

ζ	[m]	sea surface height
u	[m/s]	eastward velocity
v	[m/s]	northward velocity
w	[m/s]	vertical velocity
$\boldsymbol{u} = (u, v)$	[m/s]	horizontal velocity vector
$\boldsymbol{v} = (u, v, w) = (u_1, u_2, u_3)$	[m/s]	3D velocity vector
$\boldsymbol{U} = (U, V) = \int_{-H}^{0} \boldsymbol{u}\,\mathrm{dz}$	[m^2/s]	vertically integrated horizontal velocity
Ψ	[Sv]	Stream function (1 Sv=10^6 m^3/s)
$\rho = \rho_0 + \rho'$	[kg/m^3]	density
$p = p_0 + p'$	[Pa]	pressure
$u_h = (u_1 \dots u_N), v_h$		discrete counterparts of the variables above
$\zeta_h = (\zeta_1 \dots \zeta_\nu)$		
A_h	[m^2/s]	horizontal viscosity coefficient
A_v	[m^2/s]	vertical viscosity coefficient

Scales

L, L_x, L_y	[m]	Length scales
H	[m]	Depth scale
U	[m/s]	velocity scale
$P = fUL\rho_0$	[Pa]	pressure scale

Chapter 1

Introduction

The ocean occupies approximately two thirds of the earth surface and its interactions with the earth atmosphere play an important role in determining the earth's climate system. For a profound understanding and prediction of the earth's climate a good knowledge and reliable description of the large-scale ocean circulation and corresponding transports of heat and mass are therefore required. In large parts of the ocean, however, the amount of measured data is rather sparse and numerical models become very useful for interpretation and analysis of measurements, gaining understanding of the ocean dynamics and predicting the ocean state.

A variety of spatial and temporal scales characterise motion of water masses in the ocean. Moreover, ocean basins have complex coastlines and bottom topography which have strong influence on aspects of ocean circulation such as positions and dynamics of western boundary currents and overflows which have profound influence on the entire ocean general circulation. Modelling the ocean general circulation is thus a challenging task requiring combination of modern numerical approaches with good knowledge of physical processes, their parameterisation, observational data and geophysical fluid dynamics. Numerous ocean circulation models were developed, and new models appear with increasing realism in reproducing the ocean dynamics. A recent review of the current state of the art in ocean modelling can be found in Griffies et al. (2000).

Nowadays most numerical ocean models are based on difference techniques employing regular grids. These techniques, however, put constraints on the location of model computational nodes and thus on spatial discretisation representing coastlines in a stepwise fashion. There are three main approaches with respect to the vertical coordinate. The largest class form z-coordinate models. One example is the Modular Ocean Model MOM which originates in Bryan (1969) (see Pacanowski, 1996, for a more recent review). Other models of this family are POP (Parallel Ocean Program, Smith et al., 1992; Dukowicz and Smith, 1994) and the model hierarchy FLAME (Family of Linked Atlantic Model Experiments, FLAME Group, 1998). Further examples of z-level models are the general cir-

culation model of the Massachusetts Institute of technology MITgcm (Marshall et al., 1997) and OPA (Océan PArallélisé; Andrich, 1988)

In their general form, they represent bottom topography in a stepwise manner. Their advantage is the absence of pressure gradient errors (linked to relatively strong vertical stratification of the density field). Two recipes were suggested in order to provide more realism in representing the bottom topography in z-coordinate models. They include 'partial' cells (see Pacanowski and Gnanadesikan, 1998) which replaces full steps of topography by their best stepwise approximation and 'shaved' cells suggested by Adcroft et al. (1997).

The second group is formed by σ- or generalised vertical coordinate models, for example the Princeton Ocean Model POM (Blumberg and Mellor, 1987) or the S-Coordinate Rutgers University Model SCRUM (a manual is available at http://marine.rutgers.edu/po/models/scrum.htm) whose vertical coordinate changes from a bottom following in the deepest layer to a geopotential one at the surface. They allow smooth bottom topography, yet introduce pressure gradient errors in regions where the bottom slopes steeply. Frequently excessive smoothing is required to keep these errors at a reasonable level, which makes it difficult to set up global versions of such models. However they are successfully applied in regional studies, especially for modelling the spreading of dense overflow waters where their bottom following coordinate is of primary importance.

Finally, the third group consists of isopycnal models like the Miami Isopycnic Coordinate Ocean Model MICOM (see Bleck et al., 1992) or the Hallberg Isopycnal Model HIM (see Hallberg, 1995, 1997). These models are well suited for modelling adiabatic dynamics of deep density layers. The hybrid coordinate version (HYbrid Coordinate Ocean Model HYCOM) is based on a coordinate that is isopycnal over most of the basin yet deviates in coastal regions (see Bleck, 2002). The performance of these (level, sigma and isopycnal) approaches in the Northern Atlantic at 1/3 degree resolution was analysed in the framework of the DYNAMO project (Barnard et al., 1997). Neither of them is perfect because dynamics of the real ocean is too complex, yet each has its own advantages.

An alternative to Finite Differences and regular grids is the use of the Finite Element Method which admits a very flexible unstructured discretisation, smooth coastlines, local mesh refinements and smooth sloping topography. In the vertical, one can use z-coordinates and yet have sloping bottom in analogy with 'shaved' cells. The use of generalised s-coordinates, i.e., a combination of z- and σ-coordinates is also possible, and there might be a certain number of layers following the topography whereas other layers are geopotential in order to avoid errors in pressure discretisation. The possibility of local mesh refinement and mesh flexibility is the main motivation for using finite elements in ocean models, as many local-scale features (like Denmark Strait overflow) that have strong influence of the entire circulation could be resolved in framework of coarse models.

The first application of the FEM to physical problems dates back to the 1960's

and is connected to the field of elasticity. The big success in this branch led to applications in fluid dynamics but due to the huge computational costs a successful treatment of large problems could not be tackled before the 1980's. Since then several applications to oceanographic problems have been performed. Most of them were concerned with tidal or barotropic wind-driven oceanic flows (Myers and Weaver, 1995; LeProvost, 1986). Up to now there are only a few 3D ocean models based on the FEM, yet neither of them is designed to model the large-scale ocean circulation on decadal time scale. The two most widely used models are QUODDY (see Lynch and Naimie (1993) and Lynch et al. (1996)) and ADCIRC (see http://www.marine.unc.edu/C_CATS/adcirc). They employ finite-element discretisation only in the horizontal direction, and are designed for tidal and coastal applications within for relatively short periods of time (up to several months). 3D finite element discretisation was used in the stationary inverse model FEMSA (Finite Element Model for the South Atlantic, Dobrindt, 1999), two more examples are SEOM, the Spectral Element Ocean Model (see Iskandarani et al., 2003) and the model by Iakovlev (1996) configured for the Arctic, which makes use of a structured grid and is in this respect close (apart from some details of numerics) to finite-difference z-coordinate models. There is ongoing effort of several groups in developing finite-element or finite volume general circulation models for the ocean and atmosphere based on unstructured grids (the ICON project at DWD and MPI for Meteorology in Hamburg, see http://icon.enes.org, for other efforts, see http://wessex.eas.ualberta.ca/∼myers/FE/fe-page.html).

Intention and motivation of the thesis

Within the framework of this thesis, a primitive-equation Finite Element Ocean circulation model (FEOM_0) was developed. Motivation for this effort is to design a flexible ocean general circulation model intended for climatic studies. For reasons of flexibility, FEOM_0 uses a tetrahedral discretisation of the computational domain which allows both variable horizontal resolution and sloping bottom. The author did both the design and optimisation of the basic model version (subscript '0' means 'basic').

In order to establish a new model, its overall performance, efficiency and accuracy of its numerical algorithms should be tested and adjusted using a suite of typical problems related to the field of application. This is the motivation for the second part of the work presented in the following. Of special interest are test problems which either allow comparison to analytical results or which can be compared to the results of already established models in similar setups. For this reason numerous numerical experiments were conducted which are taken from the following fields:

- Wave propagation
- The wind-driven circulation

- Downslope flow of a dense water plume

$FEOM_0$ was further developed in the "Inverse Modelling Group" of Alfred Wegener Institute and contains now stabilisation schemes and further integration modes (rigid lid, splitting between barotropic and baroclinic mode). The extended model FEOM is documented in Danilov et al. (2004).

Outline of the thesis

The thesis is divided into two parts. The first part (chapters 2 and 3) introduces the model and the method whereas the subject of the second part (chapters 5-7) are the performed physical experiments.

Model structure

In chapter 2 the model and all principles it is based upon are presented. The goal is, to formulate the algorithm of the model in continuous, weak and discrete form, such that insight into the physical principles as well as the numerical techniques and the discrete formulation of the equations is gained. Additionally the necessary theory of the Finite Element Method is introduced.

The first topic of chapter 3 is the numerical implementation of the model. First some notes on mesh generation are given to emphasise important criteria for the choice of the nodal density. Furthermore the construction of the vertically structured grids used in the presented studies is introduced. Algorithmic techniques, concerning the construction of the matrices in the model as well as the solution of the corresponding linear systems of equations are discussed further. An important feature of the Finite Element Method is the necessity to solve huge systems of equations and therefore numerical methods applied in such problems like iterative solvers and preconditioning need to be regarded.

The second topic of chapter 3 is the performance of the advection scheme. Properties like conservation and monotonicity of the tracer under consideration are very important especially for biological simulations. In a domain with prescribed velocity field the advection of a tracer is modelled in a regular as well as in an unstructured grid. The conservation properties and occurring "overshooting" (artificial extrema) are examined.

Wave propagation

The second part of the thesis starts with chapter 4 on wave propagation. Waves are the main mechanism to propagate disturbances in the ocean and a wrong representation has impact on model results in the case of time varying forcing fields. Since the resolution of the Finite Element Model varies, also the representation of waves varies and it is of importance to make sure that a carefully generated

mesh with smooth refinements gives acceptable results in that respect. After a short introduction into the theory of waves in the ocean the model is applied to the propagation of baroclinic Rossby waves in a stratified fluid. A regular and an unstructured grid with a high and a low resolved part are used to compare the results on one hand side to the theoretically obtained wave speed and on the other hand with regard to the influence of different resolutions.

Wind-driven circulation

The wind-driven circulation is the main topic of chapter 5. It considers classical problems originating in the attempts to explain the transports arising from a given wind field. Important aspects of this topic are the boundary layers near the surface and the lateral boundaries. A proper resolution of these layers is crucial for a correct description of the resulting circulation. Whereas earlier works on this topic were two dimensional the focus in this thesis lies on both the horizontal and vertical structure of the flow field. Although the wind influences directly via turbulent exchanges only the upper layer of the ocean, it is able to set the whole water column into motion. The process responsible for this ability is the so called Ekman pumping. It is connected to the vertical velocity at the bottom of the surface layer which needs to be represented by the model.

If the density of the fluid is constant everywhere, the resulting horizontal flow field is barotropic below the surface layer, i.e., it is independent of the z-coordinate. On the other hand if the fluid is stratified, waves deforming the pycnoclines are present at the initial stage of ocean spin-up and have a huge impact on the flow field. The spin-up of a stratified ocean was considered for example by Anderson and Gill (1975), and experiments presented here are analogous to model runs performed by Olbers and Eden (2003).

Downslope flow of a dense water plume

Motivation for the modelling of dense water on a slope is linked to the problem of representing the deep circulation in the oceans. The dense water forming the lowest water masses are produced in a few regions near the poles by a loss of heat and fresh water. A part of the dense water originating from the northern polar region is transported through the Denmark Strait and forms a part of the deep western boundary current flowing along the North American coast below the Gulf Stream in southward direction. The representation of the Denmark Strait overflow is crucial for the whole thermohaline circulation, i.e. the part of the circulation driven by density differences and forming the world wide "conveyor belt circulation".

Numerical models have been found to require high resolution in the area of the strait for a good representation of the downslope flow. Additionally the quality depends especially on the formulation of the bottom boundary layer in order to

cope with the stepwise topography present in z-level FD models (Beckmann and Döscher, 1997; Killworth and Edwards, 1999). That is why there is a wish to compare the capabilities of different models with respect to the overflow problem systematically.

The DOME intercomparison study (Dynamics of Overflow Mixing and Entrainment) [1] was conceived to bring together the performance of various models in an idealised case (Phase 1), studies on Denmark strait overflow and Mediterranean outflow (Phase 2) and finally global experiments (Phase 3).

Chapter 6 is intended to contribute results of FEOM_0 to the idealised study on the propagation of dense water on a slope. A plume of dense water is injected onto a slope of prescribed constant inclination. The plume undergoes entrainment and descends under the influence of Coriolis force. Experiments with homogeneous and stratified interior are compared.

[1] working notes are available at the home page
http://www.rsmas.miami.edu/personal/tamay/DOME/dome.html

Part I

The Model – The Method

Chapter 2

Model Description

Intention of this chapter is a description of the model development from the governing equations up to the implementation ready to perform the experiments in part 2 of the thesis. The presentation is divided into three steps

- section 2.1 contains the continuous equations describing ocean dynamics as well as the applied approximations
- after a short presentation of the necessary background on the finite element theory the weak formulation of the governing equations is derived in section 2.3
- Finally the discrete equations are obtained by restricting the solution space to piecewise linears

In all steps essential properties of the equations like conservation properties or necessary boundary conditions are examined.

2.1 The governing equations

The basic quantities characterising the ocean state in the following are density ρ, pressure p, the velocity vector $\boldsymbol{v} = (u, v, w)$, sea surface height ζ, temperature T and salinity S. An Eulerian description is used, i.e., the fluid motion is given by the values of all variables at any position in time and space. The partial differential equations describing the relationship of the variables above are subject of many text books such as for example Pedlosky (1987), Gill (1982), Salmon (1998) or with direct application to ocean modelling Haidvogel and Beckmann (1999), Kantha and Clayson (2000) or Kowalik and Murty (1993). The character of the following presentation is expository and short. For a thorough treatment the reader is referred to one of these books.

2.1.1 Mass conservation and incompressibility

The equation for mass conservation is given by

$$D_t\rho + \rho \operatorname{div} \boldsymbol{v} = 0, \tag{2.1}$$

where $\boldsymbol{v}$ denotes the three dimensional velocity, $D_t = \partial_t + \boldsymbol{v}\cdot\mathbf{grad}$ is the material derivative and all operators are defined in the list of symbols. In text books on fluid dynamics it is shown that for slow motions with velocities much smaller than the speed of sound equation (2.1) can be approximated by volume conservation:

$$\operatorname{div} \boldsymbol{v} = 0 \tag{2.2}$$

up to the order $O(|\boldsymbol{v}|/c_{\text{sound}})$, where the ocean value of $c_{\text{sound}} \approx 1500$ m/s.

2.1.2 The inviscid momentum equations

This section is concerned with equations of motion which are used to calculate horizontal velocities u, v and the sea surface height ζ (using volume conservation). However, since the the topic of interest is the large scale ocean circulation, several aspects have to be taken into account. These are the presence of rotation and some properties of the ocean velocity and density field which allow the application of hydrostatic and Boussinesq approximations presented in the following.

The equations of motion of an inviscid fluid in a rotating frame of reference attached to the earth is given by

$$\rho\, D_t\boldsymbol{v} + \rho 2\boldsymbol{\Omega_E} \times \boldsymbol{v} = -\mathbf{grad}\, p - \rho\boldsymbol{g}$$

where $\boldsymbol{g} = g\boldsymbol{e}_3$. In this form the equations are independent of the coordinate system on the earth but for a description of the applied approximations it is convenient to formulate them in component form and spherical coordinates (λ, φ, r).

$$\rho(\, D_t u - \frac{uv\tan\varphi}{r} + \frac{uw}{r}) \;+\; \rho f(w\cot\varphi - v) = -\frac{1}{r\cos\varphi}\,\partial_\lambda p \tag{2.3}$$

$$\rho(\, D_t v - \frac{u^2\tan\varphi}{r} + \frac{vw}{r}) \;+\; \rho f u = -\frac{1}{r}\,\partial_\varphi p \tag{2.4}$$

$$\rho(\, D_t w - \frac{u^2+v^2}{r}) \;-\; 2\Omega_{_E}\rho u\cos\varphi = -\,\partial_r p - g\rho \tag{2.5}$$

where the Coriolis parameter

$$f = 2\Omega_{_E}\sin\varphi$$

has been introduced. The velocity components are u in eastward (zonal) direction, v in northward (meridional) direction and w radially outward.

Hydrostatic approximation

Vertical velocities are very small in the ocean. Therefore the vertical acceleration in (2.5) can be neglected. The same is true for the centrifugal acceleration term $(u^2 + v^2)/r$ and the Coriolis acceleration. These modifications result in the hydrostatic approximation to equation (2.5):

$$\partial_z p = -g\rho,$$

where $z = r - r_E$.

The Boussinesq approximation

The density fluctuations in the ocean are very small (about 1 per mil) and the main part of density variation occurs in the vertical direction. Therefore it is appropriate to decompose the density into two parts:

$$\rho(\lambda, \varphi, z) = \rho_0(z) + \rho'(\lambda, \varphi, z) \text{ with } \rho' \ll \rho_0,$$

where $\rho_0(z)$ represents the large part including the main stratification and ρ' denotes the small fluctuations linked to temperature, salinity and pressure. Now the hydrostatic approximation is used to decompose the pressure as well. Define

$$p = p_0 + p' \text{ with } p_0 = \int_z^0 g\rho_0 \,\mathrm{dz},$$

thus the hydrostatic approximation is valid for p_0,

$$\partial_z p_0 = -g\rho_0.$$

An expression for the pressure fluctuations is obtained from the vertical integral of the hydrostatic equation.

$$p'(\lambda, \varphi, z) = g \int_0^{\zeta(\lambda,\varphi)} \rho_0(z) \,\mathrm{dz} + g \int_z^{\zeta(\lambda,\varphi)} \rho'(\lambda, \varphi, z) \,\mathrm{dz}$$

Pressure fluctuations are thus given by fluctuations of the sea surface height and variations of the internal density field. The atmospheric pressure at the surface is set to zero everywhere. Substituting the expression for pressure into the momentum equations and dividing by ρ_0 gives

$$\left(1 + \frac{\rho'}{\rho_0}\right) (\, D_t \boldsymbol{u} + 2\boldsymbol{\Omega_E} \times \boldsymbol{u}) = -\frac{g}{\rho_0} \nabla \int_0^{\zeta} \rho_0 \,\mathrm{dz} - \frac{g}{\rho_0} \nabla \int_z^{\zeta} \rho' \,\mathrm{dz},$$

$$\partial_z p' = -\rho' g.$$

The Boussinesq approximation consists in neglecting the terms ρ'/ρ_0 except for the buoyancy term $g\rho'/\rho_0$. This introduces only a small error on the left hand side of the momentum equation.

Within the same order of approximation we restrict the main density part to $\rho_0 = \text{const}$ and define the pressure anomaly

$$p_\rho(\lambda, \varphi, z) = g \int_z^{\zeta(\lambda,\varphi)} \rho' \, \mathrm{dz}.$$

Putting all this together gives the approximate momentum equations

$$D_t \boldsymbol{u} + 2\boldsymbol{\Omega_E} \times \boldsymbol{u} = -g\nabla\zeta - \frac{1}{\rho_0}\nabla p_\rho,$$

$$\partial_z p_\rho = -g\rho'.$$

Further approximations

Collecting the equations with hydrostatic and Boussinesq approximations in spherical coordinates shows that further approximations have to be applied in order to get a physically sensible equation for the mechanical energy and to guarantee conservation of angular momentum (see Haidvogel and Beckmann, 1999). This requires neglecting the terms containing w in the horizontal momentum equations. Additionally the thin shell approximation replaces r in the metric terms by the constant r_E. The final result is

$$(D_t u - \frac{uv\tan\varphi}{r_E}) - fv = -\frac{1}{\rho_0 r\cos\varphi}\,\partial_\lambda(g\rho_0\zeta + p_\rho), \tag{2.6}$$

$$(D_t v - \frac{u^2\tan\varphi}{r_E}) + fu = -\frac{1}{\rho_0 r}\,\partial_\varphi(g\rho_0\zeta + p_\rho), \tag{2.7}$$

$$\partial_z p_\rho = -g\rho'. \tag{2.8}$$

β-plane approximation

The physical problems examined later will consider model domains with a rather limited meridional extent. The horizontal length scale L of the basin will be of the order 1000 km, the aspect ratio $\delta = L/r_E < 1$. In this case the planetary vorticity $f = 2\Omega_E \sin\varphi$ can be linearised around the central latitude φ_0 of the domain. In the local Cartesian coordinates

$$x = r_E\lambda\cos\varphi_0, \tag{2.9}$$

$$y = r_E(\varphi - \varphi_0). \tag{2.10}$$

The Coriolis parameter f is given in the form $f = f_0 + \beta_0 y$ with $f_0 = 2\Omega_E \sin\varphi_0$ and

$$\beta_0 = \frac{2\Omega_E\cos\varphi_0}{r_E}.$$

Details on this approximation can be found in the textbooks mentioned above and in section 5 of LeBlond and Mysak (1978).

2.1.3 The sea surface height and volume conservation

An equation for the sea surface height ζ is obtained from the continuity equation (2.1) $\partial_x u + \partial_y v + \partial_z w = 0$. Vertical integration of this equation and application of the boundary conditions

$$w = \partial_t \zeta + u\,\partial_x \zeta + v\,\partial_y \zeta \qquad \text{at the sea surface } z = \zeta(x, y), \tag{2.11}$$

$$w = -u\,\partial_x H - v\,\partial_y H \qquad \text{at the bottom } z = -H(x, y) \tag{2.12}$$

result in the expression

$$\partial_t \zeta + \nabla \cdot \int_{-H}^{\zeta} \boldsymbol{u}\,\mathrm{dz} = 0 \tag{2.13}$$

which is used to calculate ζ. The total volume conservation follows immediately from this formula by integration over the ocean surface Γ_s.

$$\partial_t \int_{\Gamma_s} \zeta\,\mathrm{d}\Gamma = -\int_{\partial\Gamma_s} \int_{-H}^{\zeta} \boldsymbol{u} \cdot \boldsymbol{n}\,\mathrm{dz}\,\mathrm{d}\gamma = 0,$$

since there is no normal flow at lateral boundaries.

2.1.4 Calculation of the vertical velocity

The vertical velocity w is obtained from the continuity equation (2.2):

$$\partial_z w = -\nabla \cdot \boldsymbol{u}$$

If the boundary condition (2.11) is used at the surface then vertical integration of the equation above gives $w(x, y, z)$ and this result at the bottom is consistent with the boundary condition (2.12) as a consequence from (2.13).

2.1.5 Temperature and salinity

The equation for potential temperature is obtained from the energy equation. Both potential temperature T and salinity S are material invariants in the absence of sources and sinks. Thus the expressions for these quantities are given by

$$D_t T = \partial_t T + \boldsymbol{v} \cdot \mathbf{grad}\, T = Q_T,$$

$$D_t S = \partial_t S + \boldsymbol{v} \cdot \mathbf{grad}\, S = Q_S,$$

where Q_T and Q_S are source terms.

2.1.6 Viscosity and diffusion

Up to now neither molecular viscosity nor molecular diffusion have been considered as these are negligibly small in typical applications. Nevertheless other processes which are related to scales usually unresolved by large scale numerical models have to be taken into account. This small scale processes would smooth the gradients of large scale fields so they are usually parameterised in terms of eddy viscosity and eddy diffusivity. We illustrate their appearance below.

Expressions for this turbulent part of the motion are obtained from a separation of the flow into a large scale motion and unresolved small sub grid eddies

$$u = \bar{\boldsymbol{u}} + \hat{\boldsymbol{u}}.$$

Inserting these expressions into the momentum equations above, evolution equations for the mean part can be derived. We use Cartesian coordinates for simplicity.

$$\partial_t \bar{u}_i + \partial_{x_j}(\bar{u}_i \bar{u}_j) + \partial_{x_j} \underbrace{(\overline{\hat{u}_i \hat{u}_j})}_{-R_{ij}} - f\epsilon_{ij3}\bar{u}_j = -\frac{1}{\rho_0}\partial_{x_i}\bar{p} - g\bar{\rho}\delta_{3i},$$

R_{ij} is called the mean eddy Reynolds stress. Subtraction from the original equations gives the fluctuation part

$$\begin{aligned}\partial_t \hat{u}_i + \partial_{x_j}(\bar{u}_i \hat{u}_j) + \partial_{x_j}(\hat{u}_i \bar{u}_j) \quad &+ \quad (\partial_{x_j}(\hat{u}_i \hat{u}_j) - \partial_{x_j}(\overline{\hat{u}_i \hat{u}_j})) - \\ &- \quad f\epsilon_{ij3}\hat{u}_j = -\frac{1}{\rho_0}\partial_{x_i}\hat{p} - g\hat{\rho}\delta_{3i}.\end{aligned}$$

Equations for large scale and sub grid scale components are not closed. A hierarchy of equations on velocity moments could be derived yet their closure at some level would be required. In first order closures the Reynolds stresses are parameterised whereas in higher order approximations prognostic equations for R_{ij} are derived and the moments of higher order are parameterised (see Haidvogel and Beckmann (1999) for an overview of subgridscale closures).

The parameterisation used in the following is the assumption of a linear dependence between the eddy Reynolds stress and the gradient of the large scale flow field.

$$\operatorname{div} \overline{\hat{\boldsymbol{v}}\hat{\boldsymbol{v}}} = -\operatorname{div}(\boldsymbol{A}\ \mathbf{grad}\,\bar{\boldsymbol{v}}),$$

$$\boldsymbol{A} = \begin{pmatrix} A_h & 0 & 0 \\ 0 & A_h & 0 \\ 0 & 0 & A_v \end{pmatrix}.$$

In the following over-bars are omitted and the final form of the momentum equa-

tions using this parameterisation is

$$D_t u - fv - \operatorname{div} \boldsymbol{A}\, \mathbf{grad}\, u + g\, \partial_x \zeta = -\frac{1}{\rho_0}\, \partial_x p_\rho, \tag{2.14}$$

$$D_t v + fu - \operatorname{div} \boldsymbol{A}\, \mathbf{grad}\, v + g\, \partial_y \zeta = -\frac{1}{\rho_0}\, \partial_y p_\rho, \tag{2.15}$$

$$\partial_z p_\rho = -g\rho'. \tag{2.16}$$

An analogous parameterisation is used in the tracer equations thus potential temperature and salinity will be obtained from advection-diffusion equations:

$$\partial_t T + \boldsymbol{v} \cdot \mathbf{grad}\, T - \operatorname{div} \boldsymbol{K}\, \mathbf{grad}\, T = 0$$

where T denotes the tracer under consideration and $\boldsymbol{K}$ has the same shape as $\boldsymbol{A}$ but takes different values. Identical coefficients will be used for temperature and salinity.

This approach is the simplest possible but leads to excessive mixing across isopycnals. A more sophisticated approach would require to use a rotated diffusion tensor (Redi, 1982). Furthermore the Gent-McWilliams parametrisation (Gent and McWilliams, 1990) is sometimes applied to account for the fact that gradients in tracer fields might not only lead to mixing but also to advective fluxes.

2.1.7 The primitive equations

For later reference all prognostic and diagnostic equations are summarised and presented together with the necessary boundary conditions. The variables used in the following are

$$\rho, p_\rho, u, v, \zeta, w, T, S$$

where ρ denotes the density anomaly. The determination of these quantities will be performed in the following order.

1. **Equation of state for the density**
   In general the density depending on temperature, salinity and pressure is calculated using the UNESCO formula (see Gill, 1982; UNESCO, 1981). In the experiments below however a linear equation of state depending only on the temperature is used

   $$\rho(T) = (\rho_{20} - \alpha(T - 20℃)) \tag{2.17}$$

   with $\rho_{20} = 998.21$ kg/m^3 and $\alpha = 0.2$ kg/(m^3 ℃). The density anomaly is determined by subtracting a reference value.

2. **The pressure $\boldsymbol{p_\rho}$** is obtained from the hydrostatic equation given the density (2.17)

$$\partial_z p_\rho = -g\rho. \tag{2.18}$$

Boundary condition: $p_\rho = 0$ in $z = \zeta(x, y)$

$$p_\rho(x, y, z) = \int_z^\zeta \rho(x, y, z')\,\mathrm{dz}' \tag{2.19}$$

However for large-scale applications ζ is usually much less than the thickness of the upper layer of the vertical discretisation. Consequently the upper limit in (2.19) is set to zero in numerical calculations below.

3. **Horizontal velocity and sea surface height** are computed with knowledge of p_ρ.

$$D_t u - fv - \operatorname{div} \boldsymbol{A}\,\mathbf{grad}\, u + g\,\partial_x \zeta = -\frac{1}{\rho_0}\,\partial_x p_\rho, \tag{2.20}$$

$$D_t v + fu - \operatorname{div} \boldsymbol{A}\,\mathbf{grad}\, v + g\,\partial_y \zeta = -\frac{1}{\rho_0}\,\partial_y p_\rho, \tag{2.21}$$

$$\partial_t \zeta + \nabla \cdot \int_{-H(x,y)}^{\zeta(x,y)} \boldsymbol{u}\,\mathrm{dz} = 0. \tag{2.22}$$

Boundary conditions:

- $A_v\,\partial_z \boldsymbol{u} = \frac{1}{\rho_0}\boldsymbol{\tau}$ at the surface, where $\boldsymbol{\tau}$ denotes the wind stress
- Dirichlet boundary conditions for u, v at lateral boundaries. Velocities $u, v = 0$ at lateral walls or prescribed values at open boundaries
- Friction $\vec{\tau}_b = c\,\rho\,|\vec{v}|\vec{v}$ or free slip boundary conditions at the bottom.

4. **The vertical velocity** is diagnosed from known horizontal velocity

$$\operatorname{div} \boldsymbol{v} = 0 \tag{2.23}$$

with boundary conditions (2.11):

$$w = D_t \zeta \text{ in } z = \zeta(x, y),$$

5. **Temperature and salinity** are computed employing the known 3D velocity field

$$\partial_t T + \boldsymbol{v} \cdot \mathbf{grad}\, T - \operatorname{div} \boldsymbol{K}\,\mathbf{grad}\, T = 0. \tag{2.24}$$

Boundary conditions: In general the heat and salt fluxes are prescribed at the ocean surface where they are responsible for the interaction between the ocean and atmosphere. However in the following all fluxes are set to zero as we explore cases where the surface temperature forcing is not important:

$$\boldsymbol{K}\,\mathbf{grad}\, T = 0 \text{ at all boundaries.}$$

Now density is recalculated with new temperature values in step 1 and the algorithm iterates until the number of time steps is reached.

2.1.8 The dimensionless equations

Scaling

For comparison to theoretical results and better understanding the relative importance of the various terms in the equations of section 2.1.7 scaling can be applied. For a detailed description of this technique see Pedlosky (1987). The main idea is to replace all variables by dimensionless counterparts (denoted by tilde) of order unity.

Let L denote the typical horizontal scale, H the typical vertical and U the typical velocity scale. Then

$$x = L\tilde{x},\ y = L\tilde{y},\ z = H\tilde{z},$$

$$u = U\tilde{u},\ v = U\tilde{v},$$

$$t = T\tilde{t} \text{ and } T = U/L.$$

The scale for ζ is chosen such that $g\,\nabla\zeta$ is of the order of the Coriolis force.

$$\zeta = \frac{f_0 L U}{g}\tilde{\zeta}.$$

The pressure scale is chosen such that the pressure gradient force is of the order of the Coriolis force

$$p_\rho = P\tilde{p_\rho} = f_0 U L \rho_0\ \tilde{p_\rho}.$$

The density scale is given by the hydrostatic equation

$$\rho = \frac{P}{Hg}\tilde{\rho}.$$

The momentum equations on β-plane are given by

$$D_t\boldsymbol{u} + f_0(1 + \frac{\beta_0}{f_0}y)\boldsymbol{k} \times \boldsymbol{u} - \operatorname{div} \boldsymbol{A}\,\mathbf{grad}\,\boldsymbol{u} + g\nabla\zeta = -\frac{1}{\rho_0}\nabla p_\rho.$$

Using the scaled quantities above, dropping all tildes and dividing by $U f_0$ these equations can be written in dimensionless form as

$$\mathrm{Ro}\, D_t\boldsymbol{u} + (1 + \hat{\beta}y)\boldsymbol{k} \times \boldsymbol{u} - \operatorname{div} \boldsymbol{E}\,\mathbf{grad}\,\boldsymbol{u} + \nabla\zeta = -\nabla p_\rho$$

where $\hat{\beta} = \beta_0\, L/f_0$. All quantities are dimensionless and all terms are of the order unity except for $\mathrm{Ro} = U/(f_0 L)$, $\hat{\beta}y$ and $\boldsymbol{E} = 1/(f_0 L^2)\boldsymbol{A}$ with components

$E_h = A_h/(f_0 L^2)$, $E_v = A_v/(f_0 H^2)$. If scaling is applied to all equations of the dynamical part the result is

$$\begin{aligned}
\mathrm{Ro}\, D_t u - (1+\hat{\beta}y)v - \mathrm{div}\, \boldsymbol{E}\, \mathbf{grad}\, u + \partial_x \zeta &= -\partial_x p_\rho && (2.25)\\
\mathrm{Ro}\, D_t v + (1+\hat{\beta}y)u - \mathrm{div}\, \boldsymbol{E}\, \mathbf{grad}\, v + \partial_y \zeta &= -\partial_y p_\rho && (2.26)\\
\partial_z p_\rho &= -\rho && (2.27)\\
\mathrm{div}\, \boldsymbol{v} &= 0 && (2.28)\\
\mathrm{Ro}\left(\frac{L}{\mathrm{R}}\right)^2 \partial_t \zeta + \nabla \cdot \boldsymbol{U} &= 0 && (2.29)
\end{aligned}$$

where $\mathrm{R} = \sqrt{gH}/f_0$ denotes the external Rossby radius and the transport is defined as

$$\boldsymbol{U} = \int_{-H}^{\zeta} \boldsymbol{u}\, \mathrm{dz}. \qquad (2.30)$$

Typical quantities for the large scale circulation are $\mathrm{Ro} \approx 10^{-4}$, $E_h \approx 10^{-5}$, whereas $\hat{\beta}y \approx 10^{-1}$, thus the main balance in the equation of motion at mid-latitudes is between Coriolis force and pressure gradient force. It is called the geostrophic balance and ocean circulation roughly follows this balance outside the equatorial belt. In the equatorial region nonlinear and viscosity terms are important to balance pressure gradient terms but this case is not considered here. The size of the external Rossby radius is about 2000 km. This implies, given the smallness of Ro, that the first term in (2.29) can be neglected in those cases where fast oscillations of the sea surface height are to be filtered out. Doing this and changing (2.11) to $w = 0$ leads to the so called rigid lid approximation. We use full (2.29) for numerical stability.

Dimensionless boundary conditions

If the scale of the wind stress is chosen to be

$$T_\tau = \frac{\rho_0 A_v U}{H}$$

the surface boundary condition can be written as

$$\partial_z \boldsymbol{u} = \tau.$$

2.1.9 The Stream function-Vorticity Formulation

In many studies we are interested in the volume transports in the model domain in the case of vanishing vertical velocity at the surface. According to (2.29) $\nabla \cdot \boldsymbol{U} = 0$ and a transport stream function can be defined such that

$$U = -\partial_y \Psi, V = \partial_x \Psi.$$

The transport stream function could also be defined for time mean transport. Then it is not necessary to assume smallness of $\partial_t \zeta$.

By introducing the vorticity

$$\omega_z = \partial_x V - \partial_y U$$

and calculating the curl of the vertically integrated equations (2.20)-(2.21) the following formula for Ψ is obtained

$$\partial_t \omega_z + J(\Psi, \omega_z) + \beta \partial_x \Psi = \frac{1}{\rho_0} \mathrm{curl}\,(\boldsymbol{\tau} - \boldsymbol{\tau}_b) + \frac{1}{\rho_0} J(P, H) + A_h \nabla^4 \Psi, \tag{2.31}$$

where P denotes the bottom pressure and the corresponding Jacobian takes nonzero values only if the bottom is not flat (compare section 5.4). This formula can be written in terms of the stream function alone since $\omega_z = \nabla^2 \Psi$.

2.2 The Finite Element Method

2.2.1 Some words on the Finite Element Technique

In the preceding sections the partial differential equations describing geophysical fluid motion have been presented. Numerical approaches to these equations have to represent the solutions (∞-dimensional) by a finite number of values in nodes discrediting the model domain. Most of the ocean models today do this by applying difference methods. The derivatives are approximated by difference quotients

$$\partial_x u \approx \frac{u(x + \Delta x) - u(x - \Delta x)}{2\Delta x} + \dots$$

where Δx denotes the spacial grid step with given order of approximation. By applying these quotients, the differential equation is turned into a difference equation that can be solved numerically. This method puts constraints on the location of nodes, local mesh refinement is usually not straightforward.

The Finite Element approach is different in several respects. For a thorough treatment of the method the reader is referred to the textbooks Johnson (1990), Schwarz (1991), Zienkiewicz and Taylor (2000a), Zienkiewicz and Taylor (2000b) and Girault and Raviart (1986). The general approach is exemplified by the following problem: Solve the second order differential equation

$$\mathcal{L}\boldsymbol{u} = f \text{ in a domain } \Omega \qquad \text{(D)}$$

$$\boldsymbol{u} = \boldsymbol{u}_0 \text{ on the boundary } \partial\Omega = \Gamma.$$

The following steps are applied.

1. First a function space V is chosen in which the problem (D) is tractable. Generally for a second order problem this space is a Sobolev space $H^1(\Omega)$, the space of square integrable functions such that a weak derivative [1] exists which is again square integrable.

2. Now the differential equation (D) is projected into V by applying the L^2-scalar product in the following way: equation (D) is multiplied by a 'test function' $\tilde{\boldsymbol{u}} \in V$ and integrated

$$\int_\Omega \mathcal{L}\boldsymbol{u}\ \tilde{\boldsymbol{u}}\,\mathrm{d}\Omega =: a(\boldsymbol{u}, \tilde{\boldsymbol{u}}) = (f, \tilde{\boldsymbol{u}}).$$

   In this step usually integration by parts can be applied, and finally there are only derivatives up to first order although (D) is of second order.

3. After this manipulation (D) can be written in variational form:
   Find $\boldsymbol{u} \in V$ such that for each $\tilde{\boldsymbol{u}} \in V$

$$a(\boldsymbol{u}, \tilde{\boldsymbol{u}}) = (f, \tilde{\boldsymbol{u}}) \qquad \text{(V)}$$

4. The formulation (V) is more accessible to techniques of pure and applied mathematics however for numerical treatment the problem has to be discretized. This is done using the Galerkin method by first choosing a finite dimensional subspace V_h of V. Functions in V_h are represented by a finite number of basis functions.

$$V_h \ni u_h = \sum_{i=1}^{N} u_i \phi_i$$

   where u_i are coefficients, $\{\phi_i\}_{i=1\ldots N}$ denotes a basis of V_h and N its dimension. Possible choices for V_h are piecewise polynomials of given degree or spectral spaces. The major requirement of Galerkin method is that (V) holds for each $\tilde{u} = \Phi_i$, in other words, the residual is orthogonal to any basis function of V_h.

5. With the chosen representation the variational problem (V) can be written as a linear system of equations

$$\boldsymbol{A}\boldsymbol{u} = \boldsymbol{r}$$

[1] A weak derivative u of a function f is a function which satisfies the partial integration

$$\int_\Omega u\tilde{u} = -\int_\Omega f\tilde{u}'\,\mathrm{d}\Omega$$

for any test function $\tilde{u} \in C^\infty$ which takes zero boundary values and has the derivative $\tilde{u}'$.

where the matrix $\boldsymbol{A}$ is called stiffness matrix and the entries of $\boldsymbol{A}$ are given by

$$\boldsymbol{A}_{ij} = a(\phi_i, \phi_j),$$

whereas

$$\boldsymbol{r}_i = \sum_{j=1}^{N} f_j(\phi_i, \phi_j).$$

There are several remarks to be made:

- In the finite element approach **boundary conditions** are treated in a natural way: they appear in the integrals of $a(\boldsymbol{u}, \boldsymbol{v})$, have to be evaluated and be put to the right hand side of the resulting system of equations. In case of the Poisson problem $\Delta u = f$ in Ω with **Neumann conditions** the weak formulation is

  $$(\nabla u, \nabla \tilde{u}) = (f, \tilde{u}) + \int_{\partial\Omega} \tilde{u} \nabla u \cdot \boldsymbol{n} \, \mathrm{d}\Gamma$$

  and the integral on the right is evaluated using the Neumann conditions for u.

  On the other hand **Dirichlet conditions** can be implemented in strong or weak form. In strong implementations test functions with vanishing boundary values are chosen and the solution is restricted to the subspace of the solution space in which the Dirichlet conditions are exactly satisfied. Weak treatment leaves more freedom since there is no restriction on the test functions and the boundary conditions are satisfied in a mean sense (see for example Johnson (1990)).

- The variational problem (V) is equivalent to a minimisation problem

  $$\text{Minimise the functional } F(\boldsymbol{u}) = \frac{1}{2} a(\boldsymbol{u}, \boldsymbol{u}) - (f, \boldsymbol{u})$$

  which can be physically interpreted as energy minimisation (the norm $||u||^2 = a(\boldsymbol{u}, \boldsymbol{u})$ is called the energy norm).

- The approach presented above can be used to investigate the existence and uniqueness of solutions of the differential equations arising from geophysical problems, see for example Lewandowski (1997).

2.3 Weak and discrete formulation of the governing equations

2.3.1 The actually used function spaces

In the following the method presented above is applied to the governing equations. First of all the appropriate function space V to handle the differential equations needs to be chosen. Although the equations contain terms of up to second order, the Sobolev space $H^1(\Omega)$ of square integrable functions with square integrable weak derivatives of first order is sufficient.

Galerkin's method consists in choosing a finite dimensional subspace V_h of V. To do so the model domain Ω is decomposed into tetrahedrons, since these are well suited to represent shore lines and topography. For more details on mesh generation the reader is referred to chapter 3. The discretisation $\mathcal{T}_\Omega$ contains N nodes and all discretized variables v_h are assumed to be piecewise linear i.e. v_h is given by

$$v_h \in P_1(\mathcal{T}_\Omega)$$

$$v_h(x,y,z) = \sum_{n=1}^{N} v_n \phi_n(x,y,z)$$

where $v_n = v(n)$ denotes the model value in node n and the functions $\{\phi_n\}_{n=1\ldots N}$ form a basis of the space $V_h = P_1(\mathcal{T}_\Omega)$ of piecewise linears which is actually a subspace of $V = H^1(\Omega)$. The function ϕ_n takes value 1 in node n, value zero in all other nodes and is piecewise linear in between.

Analogously the surface Γ_s is decomposed into triangles by the triangulation t_{Γ_s} with ν nodes. Variables defined only in Γ_s like the sea surface height ζ_h are given by

$$\zeta_h(x,y) = \sum_{n=1}^{\nu} \zeta_n \psi_n(x,y)$$

where ψ_n is a basis function of the space $P_1(t_{\Gamma_s})$. It is defined analogously to ϕ_i and is visualised in figure 2.1. The coefficients v_n, ζ_n coincide with nodal values of discretized fields.

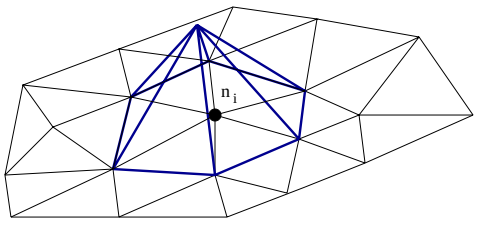

Figure 2.1: The shape of the 2D-basis function corresponding to node n_i.

2.3.2 Implementation of boundary conditions

There are four kinds of boundaries as shown in figure 2.2 At the surface Γ_s

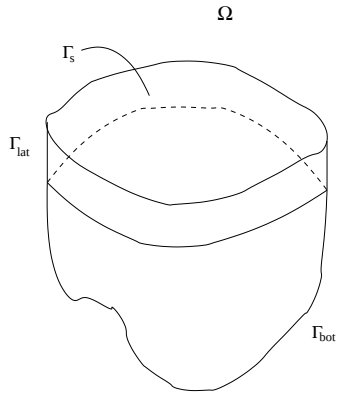

Figure 2.2: The model domain Ω. There are four kinds of boundaries: The surface Γ_s, lateral boundaries Γ_{lat}, the bottom Γ_{bot} and open boundaries Γ_{op}.

usually wind stress is applied in form of a Neumann condition. Lateral boundaries Γ_{lat} are vertical borders next to the surface where usually no slip conditions are implemented. On the bottom Γ_{bot} no normal flow is prescribed and finally there may be open boundaries Γ_{op} where for example the inflow rate is given.

2.3.3 The dynamical part

The variational form of the equations of motion and integrated volume conservation is obtained by projecting the differential equations into $H^1(\Omega)$ via the L^2-scalar product. Multiplication of equations (2.20)-(2.21) by a 'test function' $\tilde{u} \in H^1(\Omega)$ and integration over Ω (and analogously multiplication of (2.22) by $\tilde{\zeta} \in H^1(\Gamma_1)$ with Γ_s-integration) gives

$$\int_\Omega \tilde{u}\ \partial_t u \,\mathrm{d}\Omega - \int_\Omega \tilde{u}(fv + \operatorname{div} \boldsymbol{A}\ \mathbf{grad}\, u - g\,\partial_x \zeta)\,\mathrm{d}\Omega = \int_\Omega \tilde{u}\,\frac{1}{\rho_0}\,\partial_x p_\rho - \tilde{u}\,\boldsymbol{v}\cdot\mathbf{grad}\, u\,\mathrm{d}\Omega,$$

$$\int_\Omega \tilde{v}\ \partial_t v \,\mathrm{d}\Omega + \int_\Omega \tilde{v}(fu - \operatorname{div} \boldsymbol{A}\ \mathbf{grad}\, v + g\,\partial_y \zeta)\,\mathrm{d}\Omega = \int_\Omega \tilde{v}\,\frac{1}{\rho_0}\,\partial_y p_\rho - \tilde{u}\,\boldsymbol{v}\cdot\mathbf{grad}\, v\,\mathrm{d}\Omega,$$

$$\int_{\Gamma_s} \tilde{\zeta}\ \partial_t \zeta \,\mathrm{d}\Gamma + \int_{\Gamma_s} \tilde{\zeta}\ \nabla \cdot \int_{-H(x,y)}^{\zeta(x,y)} \boldsymbol{u}\,\mathrm{d}z\,\mathrm{d}\Gamma = 0.$$

Integration by parts of the second order terms reduces the highest order of derivatives by one:

$$\begin{aligned}\int_\Omega \tilde{u}\,\mathrm{div}\,\boldsymbol{A}\,\mathbf{grad}\,(u)\,\mathrm{d}\Omega &= \int_{\partial\Omega} \tilde{u}\,\boldsymbol{A}\,\mathbf{grad}\,(u)\cdot\boldsymbol{n}\,\mathrm{d}\Gamma - \\ &- \int_\Omega \mathbf{grad}\,(\tilde{u})\,\boldsymbol{A}\,\mathbf{grad}\,(u)\,\mathrm{d}\Omega\end{aligned}$$

Boundary conditions are implemented by evaluating the boundary integral. There are Dirichlet conditions prescribed on all lateral boundaries. These are implemented in strong form, therefore $\tilde{u}$ is chosen to be zero on all boundaries except for Γ_s (compare section 2.3.2) and Γ_{bot} if a quadratic bottom stress is to be used. The surface and bottom integrals are evaluated by using the wind stress and bottom boundary condition:

$$\begin{aligned}\int_{\Gamma_s\cup\Gamma_{\mathrm{bot}}} \tilde{u}\,\boldsymbol{A}\,\mathbf{grad}\,(u)\cdot\boldsymbol{n}\,\mathrm{d}\Gamma &= \int_{\Gamma_s\cup\Gamma_{\mathrm{bot}}} \tilde{u}\,A_v\,\partial_z u\,\mathrm{d}\Gamma \\ &= \int_{\Gamma_s} \tilde{u}\,\frac{1}{\rho_0}\tau_x\,\mathrm{d}\Gamma + \int_{\Gamma_{\mathrm{bot}}} \tilde{u}\,\tau_x^b\,\mathrm{d}\Gamma,\end{aligned}$$

where $\boldsymbol{\tau}^b = c^b|\boldsymbol{u}|\boldsymbol{u}$ denotes the bottom stress. The last integrals are evaluated and put to the right hand side.

The integral for sea surface height is evaluated and finally split up in a lateral boundary part which is zero due to the no normal flow conditions and a remaining volume integral.

$$\begin{aligned}\int_{\Gamma_s} \tilde{\zeta}\,\nabla\cdot\int_{-H(x,y)}^{\zeta(x,y)} \boldsymbol{u}\,\mathrm{d}z\,\mathrm{d}\Gamma &= \int_{\Gamma_s} \nabla\cdot\left(\tilde{\zeta}\int_{-H}^{\zeta}\boldsymbol{u}\,\mathrm{d}z\right) - \nabla\tilde{\zeta}\cdot\int_{-H}^{\zeta}\boldsymbol{u}\,\mathrm{d}z\,\mathrm{d}\Gamma \\ &= \int_{\partial\Gamma_s}\int_{-H}^{\zeta}\tilde{\zeta}\,\boldsymbol{u}\cdot\boldsymbol{n}\,\mathrm{d}z\,\mathrm{d}\gamma - \int_{\Gamma_s}\int_{-H}^{\zeta}\nabla\tilde{\zeta}\cdot\boldsymbol{u}\,\mathrm{d}\Gamma\,\mathrm{d}z \\ &= \underbrace{\int_{\Gamma_{\mathrm{lat}}}\tilde{\zeta}\,\boldsymbol{u}\cdot\boldsymbol{n}\,\mathrm{d}\Gamma}_{=0} + \int_{\Gamma_{\mathrm{open}}}\tilde{\zeta}\,\boldsymbol{u}\cdot\boldsymbol{n}\,\mathrm{d}\Gamma - \int_\Omega \nabla\tilde{\zeta}\cdot\boldsymbol{u}\,\mathrm{d}\Omega.\end{aligned}$$

The open boundary integral has to be evaluated using the inflow conditions. Putting together all integrations above the weak form of the dynamical problem is summarised in component form:

Find $(u, v, \zeta) \in H^1(\Omega) \times H^1(\Omega) \times H^1(\Gamma_1)$ such that

$$\begin{aligned}
\int_\Omega \tilde{u}\ \partial_t u \,\mathrm{d}\Omega \ &+\ \int_\Omega -f\tilde{u}\, v + \mathbf{grad}\,\tilde{u}\boldsymbol{A}\,\mathbf{grad}\, u + g\,\partial_x\zeta\,\tilde{u}\,\mathrm{d}\Omega = \\
&= \int_\Omega \tilde{u}(\frac{1}{\rho_0}\,\partial_x p_\rho - \boldsymbol{v}\cdot\mathbf{grad}\, u)\,\mathrm{d}\Omega + \frac{1}{\rho_0}\int_{\Gamma_s}\tilde{u}\tau_x\,\mathrm{d}\Gamma + \int_{\Gamma_{\mathrm{bot}}}\tilde{u}\,\tau_x^b\,\mathrm{d}\Gamma \\
\int_\Omega \tilde{v}\ \partial_t v \,\mathrm{d}\Omega \ &+\ \int_\Omega f\tilde{v}\, u + \mathbf{grad}\,\tilde{v}\boldsymbol{A}\,\mathbf{grad}\, v + g\,\partial_y\zeta\,\tilde{v}\,\mathrm{d}\Omega = \\
&= \int_\Omega \tilde{v}(\frac{1}{\rho_0}\,\partial_y p_\rho - \boldsymbol{v}\cdot\mathbf{grad}\, v)\,\mathrm{d}\Omega + \frac{1}{\rho_0}\int_{\Gamma_s}\tilde{v}\tau_y\,\mathrm{d}\Gamma + \int_{\Gamma_{\mathrm{bot}}}\tilde{v}\,\tau_y^b\,\mathrm{d}\Gamma
\end{aligned}$$

$$\int_{\Gamma_s}\tilde{\zeta}\ \partial_t\zeta\,\mathrm{d}\Gamma - \int_\Omega \nabla\tilde{\zeta}\cdot\boldsymbol{u}\,\mathrm{d}\Omega = 0$$

holds for all test functions $(\tilde{u}, \tilde{v}, \tilde{\zeta}) \in H^1_{\mathrm{bnd}}(\Omega)\times H^1_{\mathrm{bnd}}(\Omega)\times H^1(\Gamma_1)$. The 'test space' $H^1_{\mathrm{bnd}}(\Omega)$ is the space of functions in $H^1(\Omega)$ that take value zero on all Dirichlet boundaries.

For further investigations it is advantageous to formulate this problem in a form which is more accessible for mathematical analysis. With the bilinear forms

$$\mathfrak{a} : H^1(\Omega)\times H^1(\Omega)\to\mathbb{R} \text{ and } \mathfrak{b} : H^1(\Gamma_1)\times H^1(\Omega)\to\mathbb{R}$$

$$\mathfrak{a}(\boldsymbol{u},\tilde{\boldsymbol{u}}) = \int_\Omega \boldsymbol{f}\times\boldsymbol{u}\cdot\tilde{\boldsymbol{u}} + \mathbf{grad}\,\tilde{\boldsymbol{u}}\boldsymbol{A}\,\mathbf{grad}\,\boldsymbol{u}\,\mathrm{d}\Omega$$

$$\mathfrak{b}(\zeta,\tilde{\boldsymbol{u}}) = g\int_{\Gamma_s}\nabla\zeta\cdot\tilde{\boldsymbol{u}}\,\mathrm{d}\Gamma$$

and the right hand side terms

$$\boldsymbol{R}_p = -\frac{1}{\rho_0}\nabla p_\rho \qquad \boldsymbol{R}_\tau = \frac{1}{\rho_0}\boldsymbol{\tau}$$

the dynamical problem can be written as

$$(\,\partial_t\boldsymbol{u},\tilde{\boldsymbol{u}}) + \mathfrak{a}(\boldsymbol{u},\tilde{\boldsymbol{u}}) + \mathfrak{b}(\zeta,\tilde{\boldsymbol{u}}) = (\boldsymbol{R}_p,\tilde{\boldsymbol{u}}) + (\boldsymbol{R}_\tau,\tilde{\boldsymbol{u}})_{\Gamma_s} \tag{2.32}$$

$$(\,\partial_t\zeta,\tilde{\zeta})_{\Gamma_s} - \mathfrak{b}(\tilde{\zeta},\boldsymbol{u}) = 0 \tag{2.33}$$

Temporal derivatives

The discretisation of time derivatives is not implemented in Finite Element sense. Instead a Cranc-Nicolson method (see for example Johnson (1990)) is applied.

Although in all model runs a fully implicit scheme is used the general form of the method is presented. Consider the problem

$$(\,\partial_t u, \tilde{u}) + a(u, \tilde{u}) = (f, \tilde{u}) \tag{2.34}$$

Expanding u into a Taylor series with respect to t gives for a factor $\alpha \in [0, 1]$ and $\beta = 1 - \alpha$:

$$\begin{aligned} \alpha u_{n-1} &= \alpha(u_n - \Delta t\, \partial_t u(n)) + O(\Delta t^2) \\ \beta u_n &= \beta(u_{n-1} + \Delta t\, \partial_t u(n-1)) + O(\Delta t^2) \end{aligned}$$

where n denotes the time step. The difference of the equation above gives

$$\alpha\, \partial_t u(n) + \beta\, \partial_t u(n-1) = \frac{u_n - u_{n-1}}{\Delta t} + O(\Delta t)$$

and applying this expression to (2.34) results in

$$\alpha(-a(u, \tilde{u}) + (f, \tilde{u}))_n + \beta(-a(u, \tilde{u}) + (f, \tilde{u}))_{n-1} = (u_n - u_{n-1}, \tilde{u})/\Delta t + O(\Delta t).$$

- $\alpha = 0$ gives the fully explicit scheme
- $\alpha = 0.5$ gives the semi implicit Cranc Nicholson scheme (even of second order centred around $t_{n-1/2}$)
- $\alpha = 1$ gives the fully implicit scheme

Introducing the expression above into the variational problem and putting all known terms of time step t_{n-1} onto the right hand side gives

$$\begin{aligned} \frac{1}{\Delta t}(u(t_n), \tilde{u}) + \alpha a(u(t_n), \tilde{u}) = \frac{1}{\Delta t}(u(t_{n-1}), \tilde{u}) &- \beta a(u(t_{n-1}), \tilde{u}) + \\ &+ (\alpha f(t) + \beta f(t_{n-1}), \tilde{u}) \end{aligned}$$

Discrete equations

The discrete formulation of the dynamical part (2.32)-(2.33) is obtained by replacing the functions u, v, ζ and the corresponding test functions with piecewise linears u_h, v_h, ζ_h introduced in section 2.3.1. Since each basis function ϕ_n is different from zero only in elements neighbouring node n (compare figure 2.1) the integrations occurring in (2.32)-(2.33) can be split up into a sum of integrals as exemplified for the Coriolis term

$$\begin{aligned} \int_\Omega -fv\phi_i \,\mathrm{d}\Omega &= -\int_\Omega \sum_{j=1}^{N} f\phi_i\phi_j v_j \,\mathrm{d}\Omega = \sum_{j=1}^{N} \left[\int_\Omega -f\ \phi_i\phi_j \,\mathrm{d}\Omega\right] v_j \\ &= \sum_{j=1}^{N} \left[\sum_{n=1}^{N(i)} \int_{\Omega_n} -f\ \phi_i\phi_j \,\mathrm{d}\Omega\right] v_j \end{aligned} \tag{2.35}$$

where $N(i)$ denotes the set of tetrahedrons containing node i and Ω_n denotes a particular tetrahedron on this set. The Coriolis parameter is assumed to be constant in each element (mean of nodal values). These integrals as a whole form a linear system of equations. Each discrete variable $v_h \in P_1(\mathcal{T}_\Omega)$ or $\zeta_h \in P_1(t_{\Gamma_s})$ is identified by a vector of length N or ν and finally problem (2.32)-(2.33) is discretized in the form: Find (u_h, v_h, ζ_h) such that

$$\begin{pmatrix} S^{uu} & S^{uv} & S^{u\zeta} \\ S^{vu} & S^{vv} & S^{v\zeta} \\ S^{\zeta u} & S^{\zeta v} & S^{\zeta\zeta} \end{pmatrix} \begin{pmatrix} u_h \\ v_h \\ \zeta_h \end{pmatrix} = \begin{pmatrix} r_u \\ r_v \\ r_\zeta \end{pmatrix}$$

The following notation is introduced:

$$\boldsymbol{S}_{ij}^{uu} = \boldsymbol{S}_{ij}^{vv} = \frac{1}{\Delta t} \int_\Omega \phi_i \phi_j \, \mathrm{d}\Omega + \int_\Omega \mathbf{grad}\, \phi_i \boldsymbol{A}\, \mathbf{grad}\, \phi_j \, \mathrm{d}\Omega \tag{2.36}$$

$$\boldsymbol{S}_{ij}^{uv} = -\boldsymbol{S}_{ij}^{vu} = -\int_\Omega f \phi_i \phi_j \, \mathrm{d}\Omega \tag{2.37}$$

$$\boldsymbol{S}_{ik}^{u\zeta} = -\boldsymbol{S}_{ki}^{\zeta u} = g \int_\Omega \phi_i \, \partial_x \psi_k \, \mathrm{d}\Omega \tag{2.38}$$

$$\boldsymbol{S}_{ik}^{v\zeta} = -\boldsymbol{S}_{ki}^{\zeta v} = g \int_\Omega \phi_i \, \partial_y \psi_k \, \mathrm{d}\Omega \tag{2.39}$$

$$\boldsymbol{S}_{kl}^{\zeta\zeta} = \frac{1}{\Delta t} \int_{\Gamma_s} \psi_k \psi_l \, \mathrm{d}\Omega \tag{2.40}$$

where $i, j = 1 \ldots N$ and $k, l = 1 \ldots \nu$

The system corresponding to the dynamical part is shown in figure 2.3. It can be separated into the so called mass matrix part describing the temporal derivatives (first term of (2.36) and (2.40)) and the stationary stiffness matrix. The mass matrix contributions are denoted by M^{uu}, M^{vv} and $M^{\zeta\zeta}$, the whole system is given by

$$\begin{pmatrix} S^{uu} & S^{uv} & S^{u\zeta} \\ S^{vu} & S^{vv} & S^{v\zeta} \\ S^{\zeta u} & S^{\zeta v} & S^{\zeta\zeta} \end{pmatrix} = \begin{pmatrix} M^{uu} & 0 & 0 \\ 0 & M^{vv} & 0 \\ 0 & 0 & M^{\zeta\zeta} \end{pmatrix} + \begin{pmatrix} St^{uu} & St^{uv} & St^{u\zeta} \\ St^{vu} & St^{vv} & St^{v\zeta} \\ St^{\zeta u} & St^{\zeta v} & 0 \end{pmatrix}$$

Since large-scale ocean flows are approximately geostrophic, the off diagonal block of the dynamical matrix dominate, which makes the problem difficult to solve. The mass matrix is symmetric and can improve the bad condition number of the system. In section 3.2 some remarks on the numerical implementation and solution of the linear systems will be given.

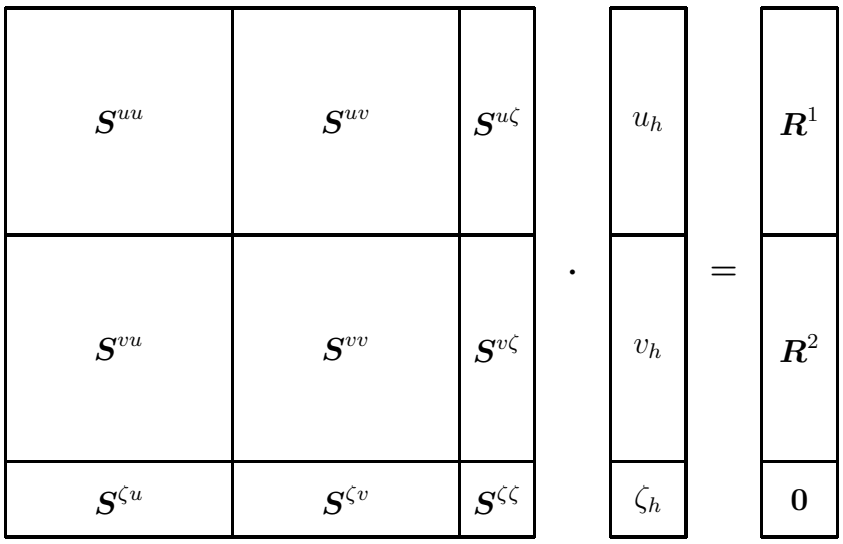

Figure 2.3: Schematic representation of the linear system of equations corresponding to the dynamical part of the model, solving for u, v and ζ.

2.3.4 Calculation of the vertical velocity

The vertical velocity is diagnosed from the horizontal velocity field using volume conservation. From the variational formulation it will be seen that global volume conservation is ensured but it is necessary to consider in which sense local conservation holds.

As it was pointed out in section 2.1.4, the continuity equation together with the surface boundary condition gives a solution which is consistent with the bottom boundary condition used for determination of ζ. Obtaining w by numerical integration however produces errors which accumulate at the bottom and lead to inconsistencies (see, for example, Lynch and Naimie (1993)). Therefore in the model the z-derivative of the continuity equation

$$\partial^2_{zz} w = -\,\partial_z(\,\partial_x u + \,\partial_y v) \tag{2.41}$$

with two boundary conditions (2.11) and (2.12) is used. This method results in smaller numerical errors.

Since the resulting linear systems are formally equivalent (they differ only numerically) the conservation properties are described with respect to the weak continuity equation.

The Dirichlet boundary conditions (2.11) and (2.12) are implemented in weak form since this allows the use of the same test functions in the vertical velocity calculation as in the tracer part where only Neumann conditions are prescribed. The discrete variational problem reads:

find $w_h \in P_1(\mathcal{T}_\Omega)$ such that

$$\int_\Omega \tilde{w}_h \mathrm{div}\, \boldsymbol{v}_h \,\mathrm{d}\Omega + \int_{\Gamma_s} \tilde{w}_h \, w_h \,\mathrm{d}\Gamma = \int_{\Gamma_s} \tilde{w}_h \, D_t\zeta_h \,\mathrm{d}\Gamma$$

holds for each $\tilde{w}_h \in P_1(\mathcal{T}_\Omega)$. Choosing $\tilde{w}_h = 1$ gives

$$\int_\Omega \mathrm{div}\, \boldsymbol{v}_h \,\mathrm{d}\Omega = \int_{\Gamma_s} (\, D_t\zeta_h - w_h) \,\mathrm{d}\Gamma$$

thus globally the error in volume conservation given by the numerical discrepancy in satisfying the boundary conditions. The local conservation however needs further attention. Since velocity is piecewise linear, the derivatives are constant in elements. The goal of zero divergence in each element however can not be reached since in general, in three dimensions the number of tetrahedrons is approximately 6 times larger than the number of nodes. A typical example is the grid of an experiment in chapter 6 (6.3) with 31320 nodes and 166650 elements. A possible technique to obtain zero divergence element wise is the use of nonconforming elements that is, using basis functions which are not continuous along sides of tetrahedrons but only in one point of the edges. By doing so the number of degrees of freedom in the velocity part is sufficiently enlarged (see for example Thomasset (1981)). In the following however continuous basis functions are used and consequently volume conservation can not be expected in each element.

However by examining the variational problem above it can be seen that each row of the resulting linear system contains the integral of the divergence over the cluster of elements neighbouring a node, which is set to zero or to a value corresponding to the boundary conditions. As a result the field satisfies the continuity equation integrally in clusters of elements neighbouring each node.

Finally the discrete variational problem of the $z-$derivative of the continuity equation is given. Multiplying this equation by a test function $w \in H^1(\Omega)$ and discrediting gives: Find $w_h \in P_1(\mathcal{T}_\Omega)$ such that

$$-\int_\Omega \partial_z \tilde{w}_h \,\mathrm{div}\, \boldsymbol{v}_h \,\mathrm{d}\Omega + \int_{\Gamma_s} (\tilde{w}_h \mathrm{div}\, \boldsymbol{v}_h)|_0 - (\tilde{w}_h \mathrm{div}\, \boldsymbol{v}_h)|_{-H} \,\mathrm{d}\Gamma = 0$$

holds for all $\tilde{w}_h \in P_1(\mathcal{T}_\Omega)$. The boundary conditions are implemented by adding the surface and bottom integrals.

$$\int_{\Gamma_s} \tilde{w}_h \, w_h \,\mathrm{d}\Gamma = \int_{\Gamma_s} \tilde{w}_h \; D_t\zeta_h \,\mathrm{d}\Gamma$$

$$\int_{\Gamma_{\mathrm{bot}}} \tilde{w}_h \, w_h \,\mathrm{d}\Gamma = -\int_{\Gamma_{\mathrm{bot}}} \tilde{w}_h \; D_t H \,\mathrm{d}\Gamma$$

2.3.5 The tracer part

The discretisation of the advection diffusion equation (2.24) in the same manner as in previous sections gives the variational formulation:
Find $T_h \in P_1(\mathcal{T}_\Omega)$ such that

$$\int_\Omega \tilde{T}_h(\,\partial_t T_h + \boldsymbol{v}_h \cdot \mathbf{grad}\, T) + \mathbf{grad}\,\tilde{T}_h \boldsymbol{K}\ \mathbf{grad}\, T_h \,\mathrm{d}\Omega = \int_{\partial\Omega} \tilde{T}_h \boldsymbol{K}\ \mathbf{grad}\, T_h \cdot \boldsymbol{n}\,\mathrm{d}\Gamma \tag{2.42}$$

holds for all $\tilde{T} \in P_1(\mathcal{T}_\Omega)$ As boundary condition usually the diffusive flux at the surface is prescribed

$$\boldsymbol{K}\ \mathbf{grad}\, T \cdot \boldsymbol{n} = Q_s \text{ on } \Gamma_s.$$

The term Q_s is substituted into the integral on the right hand side of equation (2.42).

The corresponding linear system of equations is given by

$$\boldsymbol{T}\, T_h = \boldsymbol{r}_T,$$

the entries in matrix $\boldsymbol{T}$ are given by

$$\begin{aligned}\boldsymbol{T}_{ij} = \frac{1}{\Delta t}\int_\Omega \phi_i\phi_j \,\mathrm{d}\Omega \quad &+ \quad \int_\Omega \phi_i \sum_{k=1}^{N} \phi_k \boldsymbol{v}_k \cdot \mathbf{grad}\,\phi_j \,\mathrm{d}\Omega \\ &+ \quad \int_\Omega \mathbf{grad}\,\phi_i \boldsymbol{K}\ \mathbf{grad}\,\phi_j \,\mathrm{d}\Omega\end{aligned}$$

where $i, j = 1 \ldots N$. The vector $\boldsymbol{v}_k$ in the term corresponding to the advection part denotes the velocity vector in node k. Also this integral contains only contributions from neighbouring elements. Due to the terms containing the velocity field the matrix is not symmetric. However the necessary time for the tracer part is relatively small and once the tracer stiffness matrix is calculated it is possible to apply it to an arbitrary number of passive and active tracers (with identical diffusion coefficients).

Tracer conservation

The conservation properties of the continuous equations are obtained by volume integration and the use of volume conservation.

$$\begin{aligned}\partial_t \int_\Omega T \,\mathrm{d}\Omega = \int_\Omega \partial_t T \,\mathrm{d}\Omega &= -\int_\Omega \boldsymbol{v} \cdot \mathbf{grad}\, T - \operatorname{div} \boldsymbol{K}\ \mathbf{grad}\, T \,\mathrm{d}\Omega \\ &= -\int_\Omega \operatorname{div}(T\boldsymbol{v}) - \operatorname{div} \boldsymbol{K}\ \mathbf{grad}\, T \,\mathrm{d}\Omega \\ &= -\int_{\partial\Omega} T\boldsymbol{v} \cdot \boldsymbol{n} - \boldsymbol{K}\ \mathbf{grad}\, T \cdot \boldsymbol{n}\,\mathrm{d}\Gamma\end{aligned}$$

The first term in the second integral vanishes because of the no normal flow condition and the second term equals the diffusive flux across the boundary and vanishes when the flux is zero. Under this condition the total tracer is conserved.

Choosing the test function $\tilde{T}_h = 1$ in (2.42) gives global tracer conservation of the Finite Element formulation in the same sense as in case of volume conservation. The global error is given by the numerical discrepancy in satisfying the boundary conditions. Local conservation holds in the same sense as local volume conservation in the previous section. The tracers are conserved locally in any cluster of elements sharing one node.

Chapter 3

Numerical implementation of the model and performance of the advection scheme

An important aspect of Finite Element Modelling using unstructured grids is the high computational cost. This is explained by the fact that the information about neighbouring nodes has to be taken from lookup tables. In the following this point is discussed and quantified, and strategies of assembling matrices and right hand sides is outlined. For experiments of later chapters the size of stiffness matrices as well as condition numbers and some additional characteristics are given. In the final section the performance of the advection scheme is discussed for experiments with prescribed velocity fields.

3.1 Some notes on mesh generation

The first task using the FEM is the generation of a grid well suited for the problem under consideration. It is a crucial step since several factors concerning accuracy and performance of the model rely heavily on the quality of the mesh and its capability to represent important features of the flow field to be modelled. There are two kinds of constraints on the surface grid: physical and computational ones. From computational point of view the surface grid should be of Delaunay type, i.e. a circle containing three nodes of a triangle should not contain any other nodes. Furthermore especially "long" triangles (large ratio of longest side length to radius of inner circle) should be avoided. From physical viewpoint it is important to choose the nodal density in a way such that places with large gradients of topography and strong variability of oceanic fields are highly resolved. Another criterion for high resolution is the existence of steep fronts of modelled variables in a region.

The meshes used in the following are created in two steps. At first a tri-

angulation of the surface is constructed. This 2D mesh must take into account all the numerical and physical aspects mentioned above. There are several free packages available for the creation of a two dimensional Delaunay triangulation with prescribed nodal density. For the Cartesian grids the free available package TRIANGLE (see http://www-2.cs.cmu.edu/∼quake/triangle.html) was used. Yet there are also mesh generators constructing grids on the sphere, for example the one described in Legrand et al. (2000).

In general however the automatic grid generation is not sufficient and in situations with complicated and irregular domains a lot of hand tuning is necessary to arrange the nodes and boundaries in an appropriate way.

After the surface triangulation is created, a 3D mesh is built by forming prisms below each surface triangle. The height of the top and bottom faces of the prisms are given by the vertical discretisation. In principle there are no limitations the realisation of the vertical discretisation. It can be z, σ or any combination of them. The choice is motivated by the problem under consideration. For example in chapter 6 where dense water downslope flow is examined it is appropriate to implement several layers following the topography (compare figure 6.5). Therefore bottom and top sides of the prisms are not necessarily perpendicular to the vertical faces. Especially the shape of the lowest prism in each column is prescribed by topography (see figure 3.1).

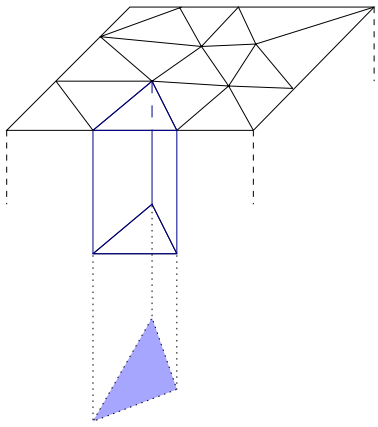

Figure 3.1: Construction of prisms below each surface triangle The height of the prisms is given by the vertical discretisation

Finally each sub-prism is divided into three tetrahedrons (see figure 3.2). In case of the lowest prism in each column however the number of subdividing tetrahedrons depends on the shape of the bottom. There might be one, two or three tetrahedrons such that the tetrahedral discretisation provides large flexibility with respect to the representation of topography. It allows also the realisation of a sloping bottom within a z-level mesh. This is advantageous when compared to the framework of finite differences where techniques like “partial cells” or “shaved

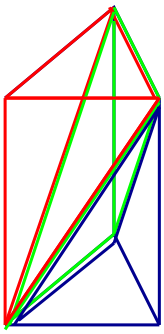

Figure 3.2: Decomposition of a prism into three tetrahedrons (indicated by colours).

cells" have to be applied, to obtain a more realistic representation of topography.

3.2 Computational Aspects

3.2.1 Assembling the stiffness matrix

After the mesh has been created the global scalar products in equations (2.36)-(2.40) must be evaluated and used to facilitate assembling the stiffness matrix. This operation is performed by decomposing the global integral into a sum of the integrals over elements (see formula 2.35) which are computed as follows (see also Schwarz, 1991).

Standard elements

The first step is the definition of standard basis functions in 2D and 3D simplexes $\hat{\tau}$ and $\hat{T}$. Simplexes and the corresponding node numbering are shown in figure 3.3

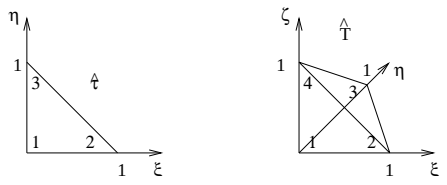

Figure 3.3: Standard elements (simplexes) $\hat{\tau}$ in 2D and $\hat{T}$ in 3D.

The piecewise linear basis functions $\hat{\psi}_i$, $\hat{\phi}_i$ taking value 1 in node i and 0 in

all other nodes are given by

$$\begin{array}{cc} 2D & 3D \\ \hat{\psi}_1 = 1 - \xi - \eta & \hat{\phi}_1 = 1 - \xi - \eta - \zeta \\ \hat{\psi}_2 = \xi & \hat{\phi}_2 = \xi \\ \hat{\psi}_3 = \eta & \hat{\phi}_3 = \eta \\ & \hat{\phi}_4 = \zeta \\ \xi, \eta \in [0,1] & \xi, \eta, \zeta \in [0,1] \end{array}$$

The corresponding gradients are

$$\begin{array}{cc} 2D & 3D \\ \nabla\hat{\psi}_1 = (-1,-1) & \mathbf{grad}\,\hat{\phi}_1 = (-1,-1,-1) \\ \nabla\hat{\psi}_2 = (1,0) & \mathbf{grad}\,\hat{\phi}_2 = (1,0,0) \\ \nabla\hat{\psi}_3 = (0,1) & \mathbf{grad}\,\hat{\phi}_3 = (0,1,0) \\ & \mathbf{grad}\,\hat{\phi}_4 = (0,0,1) \end{array}$$

Transformation to mesh triangles in 2D

The standard elements with nodes as shown in figure 3.3 have to be mapped to the actual elements in the mesh with nodes (x_i, y_i), $i = 1, 2, 3$. This is done by means of a linear transformation which is illustrated in figure 3.4 and in 2D given by

$$\Psi_\tau : \hat{\tau} \to \tau$$

$$\Psi_\tau : \begin{pmatrix} \xi \\ \eta \end{pmatrix} \mapsto \begin{pmatrix} x_1 \\ y_1 \end{pmatrix} + \xi \begin{pmatrix} x_2 - x_1 \\ y_2 - y_1 \end{pmatrix} + \eta \begin{pmatrix} x_3 - x_1 \\ y_3 - y_1 \end{pmatrix}$$

Using these transformation the gradients of local basis functions can be evaluated

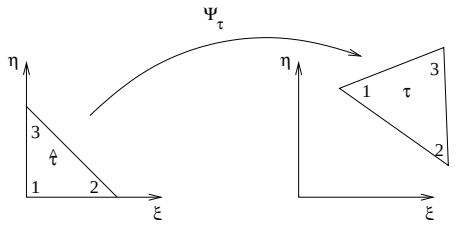

Figure 3.4: Linear transformation Ψ_τ of standard element $\hat{\tau}$ to an arbitrary triangle τ in the mesh.

in each element

$$\psi_i|_\tau = \hat{\psi}_i \circ \Psi_\tau^{-1}$$

$$\nabla\psi_i|_\tau = \nabla\hat{\psi}_i(\nabla\Psi_\tau)^{-1}$$

All local derivatives are stored and areas of triangles are stored too. Given them the scalar products are computed in the following way:

$$(\psi_i, \psi_j)_\tau = 2(\hat{\psi}_i, \hat{\psi}_j)_{\hat{\tau}} \cdot \text{area}(\tau), \tag{3.1}$$

and the global integrals in section 2.3 are evaluated as a sum over all triangles. The 3D procedure is completely analogous where additionally we need scalar products involving derivatives of 3D and 2D functions. For example, scalar products involving derivatives of 3D functions are treated as follows:

$$\begin{aligned}(\nabla\psi_i, \psi_j)_\tau &= 2\nabla\psi_i|_\tau(1, \hat{\psi}_j)_{\hat{\tau}}\ \text{area}(\tau)\\ (\nabla\psi_i, \nabla\psi_j)_\tau &= 2\nabla\psi_i|_\tau\nabla\psi_j|_\tau\ \text{area}(\tau)\end{aligned}$$

Matrix setup in the code

Unless viscosity coefficients are changed during model execution the stiffness matrix of the dynamical part has to be set up only once. But since the velocity field changes in each time step the stiffness matrix of the tracer part has to be constructed in each time step and therefore the process of matrix assembly should work as fast as possible.

Since all matrices are sparse, the row wise compressed storage format (CSR) is used, that is, a matrix $A \in \mathbb{R}^{n\times n}$ with n_z not vanishing entries is stored by saving only the values A_{ij} different from zero in a vector `values`, the corresponding column indexes j in a vector `colind` and a vector `rowptr` of length n pointing to the first value in each row. In this format only $2n_z + n$ numbers have to be stored, compared to n^2 for a full matrix.

In order to avoid time consuming if-statements in the matrix assembly information concerning the 'neighbourhood' of each node is stored. There are data structures `neighbouring_nodes` and `node_in_elements` containing for each node the neighbouring nodes and elements respectively. The situation is shown in figures 3.5 and 3.6.

In the following as an example the assembly of the matrix $S_{ij} = \int_{\Gamma_s} \psi_i\psi_j \,\mathrm{d}\Omega$ is explained with reference to figure 3.5. The matrix is filled row wise. In order to fill row 24 of this matrix the scalar product of ψ_{24} with all basis functions $\{\psi_j\}_{j=1\ldots\nu}$ has to be determined but from the shape of these functions it is clear that only the basis functions in neighbouring triangles $\tau_l \in N(24) =$ `node_in_elements`(24) will contribute entries into the matrix

$$S_{24,j} = \int_{\Gamma_s} \psi_{24}\psi_j \,\mathrm{d}\Gamma = \sum_{l=1}^{\lambda} \int_{\tau_l} \psi_{24}\psi_j \,\mathrm{d}\Gamma = \sum_{l\in N(24)} \int_{\tau_l} \psi_{24}\psi_j \,\mathrm{d}\Gamma, \tag{3.2}$$

where λ denotes the number of triangles. The last integral is calculated with the formula given in (3.1), multiplying the scalar products of the corresponding standard basis functions by the volume of triangle τ_l. Finally in row 24 there are

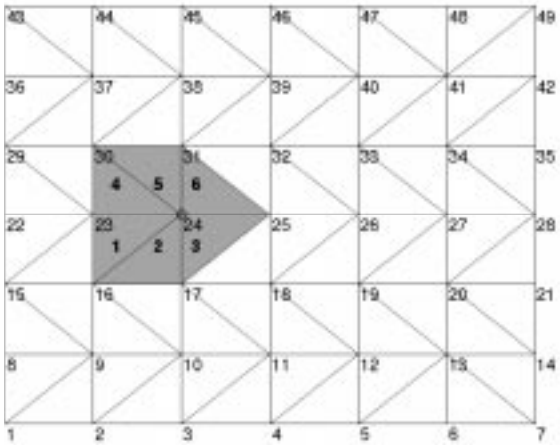

Figure 3.5: Cluster of elements sharing node 24. The 24. row of the data structure `neighbouring_nodes` contains the numbers 16, 17, 23, 24, 30, 31, the field `node_in_elements` contains the numbers of the 6 neighbouring triangles. The function ψ_{24} is one at node 24 and zero at nodes 16, 17, 23, 25, 30 and 31. The assembly should run over all triangles spanned by the test function.

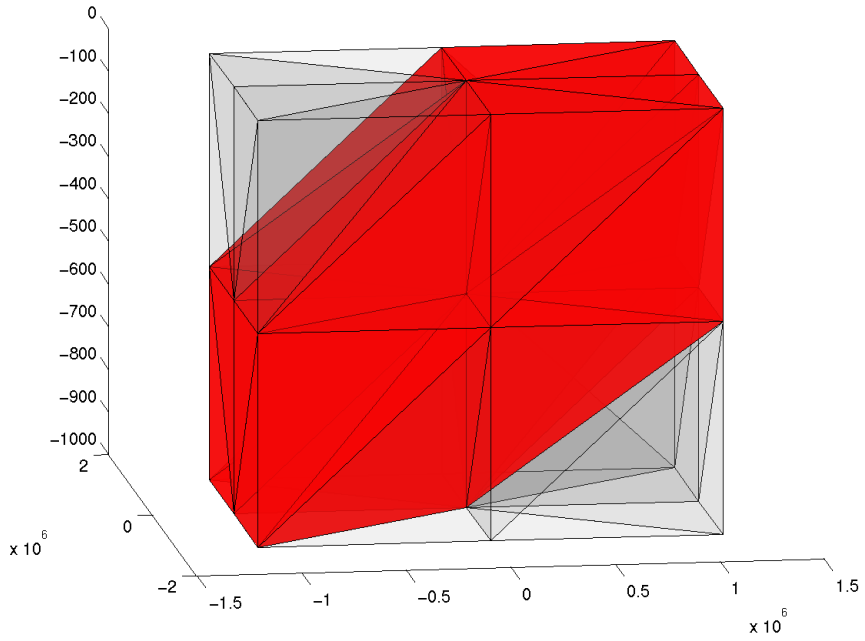

Figure 3.6: Cluster of elements sharing one node in 3D. The assembly follows the same strategy as in the 2D-case (see figure 3.5).

entries in columns 16, 17, 23, 24, 30 and 31. The entry in column 16 contains contributions from the elements τ_1 and τ_2 and the diagonal element $S_{24,24}$ is the only entry with 6 contributing elements. The algorithm works as follows:

- cycle over elements spanned by test function at node i.
- cycle over nodes of elements to compute the scalar products on element.
- Determine the position of the entry into sparse format matrix. This step needs indirect addressing and requires mapping of node number to the position in the matrix.

Since all scalar products are positive the diagonal element is the largest in this case and the matrix is diagonal dominant. It is not necessarily the case if derivatives are contained in the integrals. The gradients of local basis functions take positive and negative values and for example the setup of the first order continuity equation for w-calculation leads necessarily to zero entries on the diagonal. Also from this point of view it is advantageous to solve a corresponding second order problem. The procedure of matrix assembly however is even simpler since the derivatives are constant in each element. The gradients of basis functions in all elements are calculated in advance and stored.

Right hand sides are assembled in a similar way: integrals like in formula 3.2 are calculated, but the result is multiplied by the vector of boundary values resulting in the right hand side vector. This can be done by precalculating the operator calculating the right hand side from boundary values, thus replacing the loop over elements by a matrix multiplication.

3.2.2 Solving large sparse systems

The procedure of the previous chapter prepares the left and right hand sides of the linear systems presented in section 2.3. The main numerical burden of the Finite Element Method consists in solving these systems at each time step. The amount of necessary computations is described in this section on the example of a rather small problem.

Consider a square basin discretized regularly into $20 \times 20 \times 7 = 2800$ nodes and in an unstructured way with comparable resolution ($550 \times 7 = 3850$ nodes). The surface grids are shown in figure 3.7.

In these grids the dynamical problem is solved. The corresponding stiffness matrices have dimension 6615 (8250) and the number of nonzero entries is 247185 (311928) for regular (unstructured) grid. The ratio of the number of non-vanishing entries and the squared dimension 0.6 % (0.5 %) point up that both matrices are sparse. The pattern of entries in the stiffness matrices is shown in figure 3.8. As we have already mentioned, the main difficulty arises from terms involving sea surface height in momentum and continuity equation. These terms

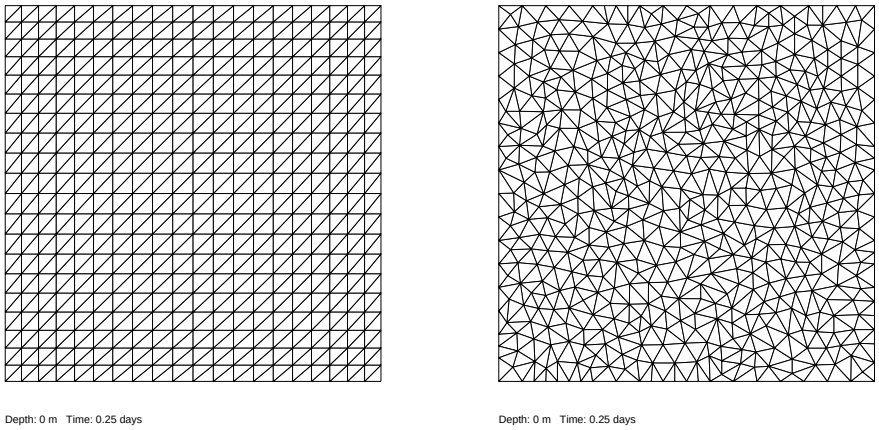

Figure 3.7: Example of surface grids used to illustrate the computational burden.

are contained in rows and columns with numbers greater than twice the number of 3D nodes 5600 (7700). As we can see the matrices is relatively dense in these rows and columns. The structure of the matrices is symmetric but the entries are not.

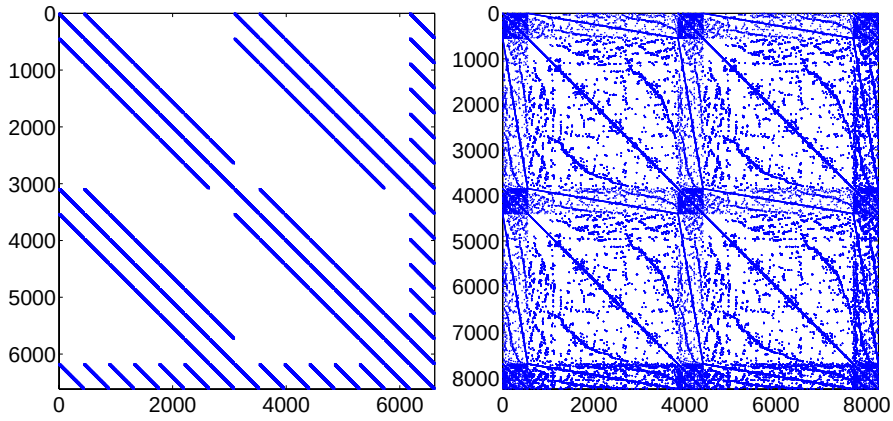

Figure 3.8: Pattern of entries in stiffness matrices corresponding to the dynamical part for determination of u,v and ζ. The left panel displays the matrix corresponding to the regular grid, whereas the right panel corresponds to the unstructured grid (compare figure 3.7).

There are various techniques developed to solve such sparse systems of equations (see Hackbusch (1993)). Mostly iterative methods are used to solve the preconditioned system. Instead of solving $\boldsymbol{S}x = b$ directly the system is preconditioned by multiplication by a matrix W^{-1} that is close to the inverse of $\boldsymbol{S}$.

$$W^{-1}\boldsymbol{S}x = W^{-1}b$$

W is called the precondition matrix and since the optimal case $W^{-1} = \boldsymbol{S}^{-1}$ is out of reach some approximation has to be chosen. The matrix $\boldsymbol{S}$ is not symmetric, thus Jacobi- and SSOR preconditioners (see Hackbusch, 1993) cannot be used. A possible choice for unsymmetrical matrices is $W = \tilde{L}\tilde{U}$ where $\tilde{L}\tilde{U}$ denotes an approximation to the standard decomposition into an upper and a lower triangular matrix $S = LU$. The standard decomposition is not feasible since L and U are not sparse even if S is. Therefore the so called incomplete LU-decomposition is performed

$$S = \tilde{L}\tilde{U} + R$$

where R denotes a residual which might be determined by fixing a drop tolerance for entries into the decomposition or prescribing a maximum number of fill-ins (additionally allowed entries in a row). By choosing a small drop tolerance the condition number of $W^{-1}\boldsymbol{S}$ is close to 1 thus the system can be solved in a small number of iterations. This might be feasible for problems of small size, for large systems however a compromise has to be found, since a smaller drop tolerance leads to higher number of fill-ins and thus a higher memory use and greater time consumption for matrix factorisation.

3.2.3 Solving $\boldsymbol{S}x = b$ in FEOM$_0$ applications

Factorisation

h The matrices above are accessible to analysis with standard tools like MATLAB provided the size of the problem is sufficiently small. Below some details on the performance of the preconditioner are given. The condition number κ gives a measure for the "quality" of a matrix $\boldsymbol{S}$. It is defined by $\kappa(\boldsymbol{S}) = \rho(\boldsymbol{S})\rho(\boldsymbol{S}^{-1})$, where $\rho(\boldsymbol{S}) = \max\{|\lambda|; \lambda \text{ is eigenvalue of } \boldsymbol{S}\}$ denotes the spectral radius of $\boldsymbol{S}$. Only a condition number close to one ensures that for a small residual $||\boldsymbol{S}x - b||$ also the error $||x - x_*||$ between found solution x and true solution x_* is small. Estimates of the condition numbers for the matrices of the dynamical part are given in table 3.1. Condition numbers of matrices at all stages of FEOM$_0$ suffer from the highly variable element size in the three dimensional case. The dynamical part was chosen for an investigation since these are the largest and highly unsymmetrical. unsymmetrical. The large values even for this small sized problem show that preconditioning of the system is necessary. This is exemplified using the UMFPACK package (see Davis, 2003; Davis and Duff, 1997, and http://www.cise.ufl.edu/research/sparse/umfpack/) for factorising the matrices shown in figure 3.8. UMFPACK calculates an LU-decomposition, but reduces the number of fill-ins by first constructing permutation matrices $\boldsymbol{P}$ and $\boldsymbol{Q}$ and then determining the LU-decomposition of the reordered matrix $\boldsymbol{PSQ}$. The reordered matrices are shown in figure 3.9. Table 3.1 contains also an estimate of the norm $||\boldsymbol{PSQ} - \boldsymbol{LU}||$ showing good representation of $\boldsymbol{S}$ by the $\boldsymbol{LU}$ decomposition.

	Regular	Unstructured
Number of nodes	3087	3850
Dimension of matrix	6615	8250
nnz(S)	247185	311928
Sparsity	0.5%	0.4%
condition number estimate	$8.4479 \cdot 10^{9}$	$3.1789 \cdot 10^{9}$
estimate of $\|\|\boldsymbol{PSQ} - \boldsymbol{LU}\|\|/\|\|\boldsymbol{S}\|\|$	$1.5199 \cdot 10^{-12}$	$5.3052 \cdot 10^{-13}$
nnz(LU); nnz(LU)/nnz(S)	1755058; 7.1	2652341; 8.5

Table 3.1: Comparison of quantities characterising the matrices shown in figure 3.8 arising from the dynamical part. The sparsity is given by the ratio of the number of nonzero entries (nnz) and the squared dimension. The permutation matrices P and Q as well as the LU decomposition were calculated with UMFPACK.

The number of fill-ins given in table 3.1 is large, but the good representation mentioned above enables a direct solution or leads to convergence of an iterative method after one step.

In larger systems such a high number of fill-ins is prohibited, therefore this number is reduced by for example choosing a drop tolerance and omitting smaller entries. Such procedures result in an incomplete LU decomposition (ILU) as already mentioned in section 3.2.2. Consequently the $||\boldsymbol{PSQ} - \boldsymbol{LU}||$ takes bigger values and an iterative solver preconditioned with the incomplete LU decomposition needs more steps for a given accuracy. For comparison ILU-decompositions of the matrix corresponding to the regular mesh are calculated with different drop tolerances employing the 'luinc' function of MATLAB without permuting the matrix. The norm estimates $||\boldsymbol{S} - \boldsymbol{LU}||/||\boldsymbol{S}||$ as a function of the drop tolerance are plotted in figure 3.10, the corresponding number of nonzero elements is given in figure 3.11. Comparison to table 3.1 points up that permutation of the stiffness matrix reduces the number of fill-ins considerably. The LU-decomposition with $1.7 \cdot 10^{6}$ entries of the permuted system corresponds to a term $||\boldsymbol{PSQ} - \boldsymbol{LU}||/||\boldsymbol{S}||$ of $1.5 \cdot 10^{-12}$, whereas a drop tolerance in the unpermuted case gives $||\boldsymbol{S} - \boldsymbol{LU}||/||\boldsymbol{S}|| \approx 10^{-8}$ and more than $8 \cdot 10^{6}$ entries.

Solving

Since the matrices we have to cope with are not symmetric, special care has to be taken with respect to the iterative algorithm. The standard conjugate gradient method cannot be applied but many methods suitable for indefinite and non symmetric problems were developed (see, for example, Hackbusch, 1993; Saad, 1996). Two methods were applied to the systems arising from FEOM_0: The Generalised Minimal Residuum Method (GMRES) and the Bi-Conjugate Gradient Stabilised Algorithm (BICGSTAB). Both methods are implemented in the PILUT pack-

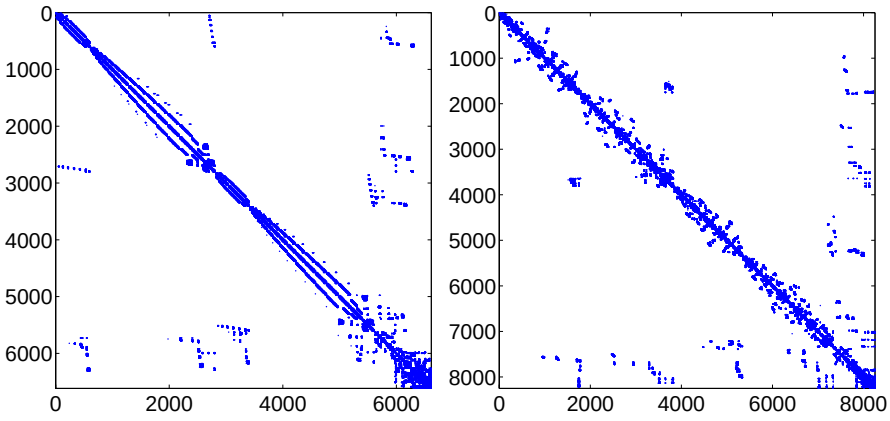

Figure 3.9: As in figure 3.8 but after reordering with UMFPACK (shown is the permutation $\boldsymbol{PSQ}$). The left panel displays the matrix corresponding to the regular grid, whereas the right panel corresponds to the unstructured grid (compare figure 3.7).

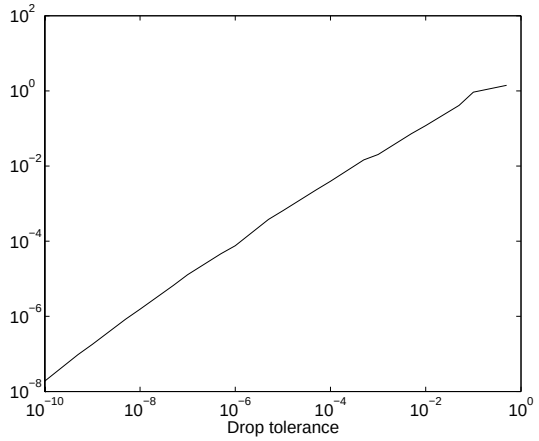

Figure 3.10: The norm $||\boldsymbol{S} - \boldsymbol{LU}||/||\boldsymbol{S}||$ in dependence on the drop tolerance for the system corresponding to the regular grid using the 'luinc' function of MATLAB for ILU calculations.

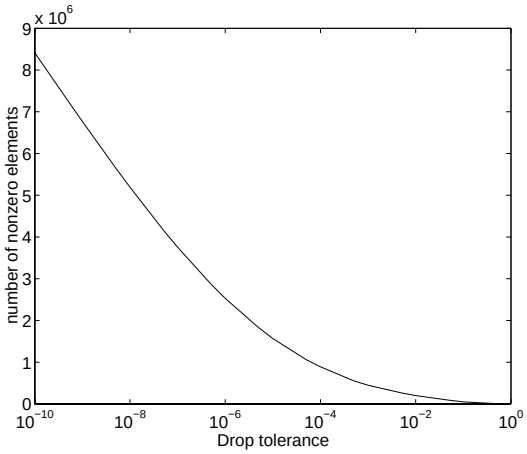

Figure 3.11: The number of nonzero elements in dependence on the drop tolerance for the system corresponding to the regular grid using MATLAB for ILU calculations.

age (Parallel Threshold-based ILU Factorisation, see Karypis and Kumar, 1998) which is used in FEOM for factorisation and solving. [1] Interfacing FEOM_0 to PILUT was carried out in collaboration with the computing centre of AWI (compare also the Family of Simplified Solver Interfaces by Stephan Frickenhaus) [2] Both methods perform comparable, however in these applications BICGSTAB was found to be about 10% faster than GMRES.

3.3 The advection scheme

Although FE discretisation is different from Finite Difference (FD) discretisation, it results in a set of difference equations. It is then instructive to compare the numerical properties of FE discretisation with those of FD. This section presents a simple analysis performed for the advection-diffusion equation (2.24)

$$\partial_t T + \boldsymbol{v} \cdot \mathbf{grad}\, T - \operatorname{div} \boldsymbol{K}\, \mathbf{grad}\, T = 0.$$

Various algorithms were developed to solve this equation in FD as well as in FE context (see Budgell et al. (2003) for a FE-overview)

In Gerdes et al. (1991) three different advection schemes are applied in a model of the large scale circulation and it is shown that there is a huge impact on the model results especially if long time scales are considered.

The advection schemes examined in Gerdes et al. (1991) are central difference scheme, upwind scheme and flux corrected scheme. These are very prominent

[1] For further information on solvers available at AWI the reader is referred to http://www.awi-bremerhaven.de/InfoCenter/IT/WorkingGroups/SciComp/SSolversUG.html.

[2] http://www.awi-bremerhaven.de/InfoCenter/IT/WorkingGroups/SciComp/FoSSI.html

schemes in a huge set of developed algorithms of first or higher order. Most important properties are

- the central difference scheme is of second order, conserves the tracer amplitude but introduces unphysical extrema, which might lead to negative concentrations of biological tracers.
- the first order upstream scheme replaces the central space derivative by a difference quotient using only upstream information. As a consequence the scheme is **monotonic** (it does not introduce erroneous extrema). As a disadvantage it introduces implicit diffusion (see Haidvogel and Beckmann, 1999, and figure 3.12).
- the flux corrected scheme is a compromise between the two schemes above. It corrects the result of the upstream procedure by adding the flux difference of central difference and upstream scheme (the anti-diffusive flux). Adding the full difference leads to ripples and thus the anti-diffusive flux has to be limited locally to give maximal flux correction without introducing overshoots.

In the following the dispersion relation of the scheme implemented in FEOM_0 is compared to the central difference scheme (CTCS, central in time, central in space) and the upstream scheme (FTUS, forward in time, upstream scheme). We restrict the setting to the one dimensional case without diffusion. An analogous comparison for FEOM in included in Danilov et al. (2004). In section 3.3.2 the complete advection diffusion problem is examined in three dimensions by solving a simple advection problem.

3.3.1 The dispersion relation in 1D

In order to compare dispersion properties of advection schemes the 1D advection equation

$$\partial_t T + u\,\partial_x T = 0$$

with prescribed constant velocity u is discretized in a regular grid. The resolution in space is Δx, the time step is Δt. Seeking for a solution in the form

$$T = T_0 \exp i(kx - \omega t)$$

one obtains the true dispersion relation given by

$$\omega = ku.$$

Discretisation of the advection equation using the FD CTCS scheme gives

$$\frac{T_j^{n+1} - T_j^{n-1}}{2\Delta t} + u\frac{T_{j+1}^n - T_{j-1}^n}{2\Delta x} = 0$$

where the upper index is the time step and the lower index gives the position. Inserting the solution gives the discrete dispersion relation

$$(\omega\Delta t)_{\mathrm{CTCS}} = \sin^{-1}(\mathrm{Co}\,\sin(k\Delta x))$$

where $\mathrm{Co} = u\Delta t/\Delta x$ is the Courant number.

Doing the same calculations for the FD upstream- and finite element scheme used by FEOM_0 gives the dispersion relations

$$(\omega\Delta t)_{\mathrm{FTUS}} = i\log(1 - \mathrm{Co}(1 - \exp(-ik\Delta x)))$$

$$(\omega\Delta t)_{\mathrm{FEM}} = -i\log\left(1 + \frac{i\,3\,\mathrm{Co}\,\sin(k\Delta x)}{2 + \cos(k\Delta x)}\right)$$

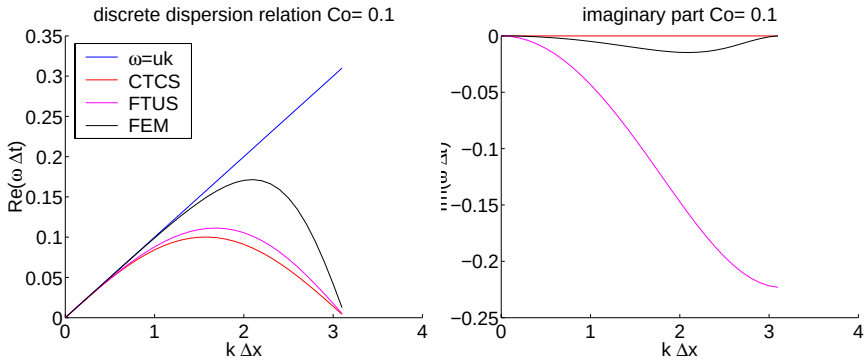

Figure 3.12: Dispersion relations for the CTCS (centred in time, centred in space) scheme, the FTUS (upwind) scheme and the scheme used in FEOM_0 . The Courant number is 0.1.

The corresponding graphs are shown in figure 3.12. The finite difference schemes need $\mathrm{Co} < 1$ to be stable, otherwise the imaginary part of ω takes positive values. It can be seen that for low Courant numbers the finite element scheme performs better than both CTCS and FTUS. In all schemes there is a drop of the real part for high wave numbers, as a consequence signals containing a short wavelength part will disperse. However CTCS and FTUS are able to represent waves of length $> 4\pi\Delta x$ correctly whereas FEM can reproduce waves of half this length. The imaginary part shows that FEM introduces some implicit diffusion but it is relatively small compared to the FTUS diffusion and leads to damping of those wavelengths which are not or badly resolved. If stabilisation techniques like Galerkin Least Squares (GLS, see Hughes et al., 1989) are used, the dispersion relation can be further improved as shown in Danilov et al. (2004).

But figure 3.13 shows that the implicit FEOM_0 advection scheme becomes very diffusive if the Courant number reaches one (it should be reminded that it is only first order in time). In this case the solution remains stable but the solution is correct only in the stationary regime. FTUS becomes slightly too fast and

compares best to the true dispersion curve. Thus it is important to choose the space-time discretisation such that Co is sufficiently small. However in typical situations (velocities not larger than 1 m/s, $\Delta t \leqslant 1$ h, $\Delta x \geqslant 20$ km) the Courant number is less than 0.2.

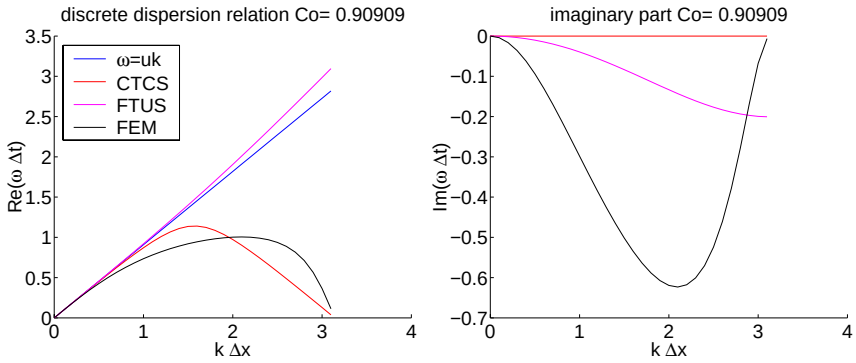

Figure 3.13: As in figure 3.12, but here Co = 0.9.

3.3.2 Advection experiment

The investigation of the previous section gives some hint on the properties of the advection scheme used in FEOM$_0$ in comparison to simple FD advection schemes. However three dimensional problems and unstructured grids cannot be examined in the traditional way. For this reason the model's advection scheme is tested numerically with an advection experiment of the following kind: a Gaussian temperature anomaly reaching from top to bottom is placed in a basin with prescribed, divergence free, depth independent velocity field. This problem is solved numerically using a regular and an unstructured grid. Important questions are:

- Is the result depending upon the structure of the grid?
- how conservative is the scheme, does any overshooting occur?

The velocity field is consistent with the no normal flow boundary condition and given by

$$\begin{pmatrix} u \\ v \end{pmatrix} = \begin{pmatrix} -u_0 \sin(x\pi/L)\cos(y\pi/L) \\ u_0 \cos(x\pi/L)\sin(y\pi/L) \end{pmatrix}$$

where $u_0 = 0.5\ m/s$ and $x, y \in [0, L]$. The divergence of this field is zero and the corresponding stream function is given by

$$\Psi(x, y) = u_0 L/\pi \sin(x\pi/L)\sin(y\pi/L),$$

the isolines are shown in figure 3.15.

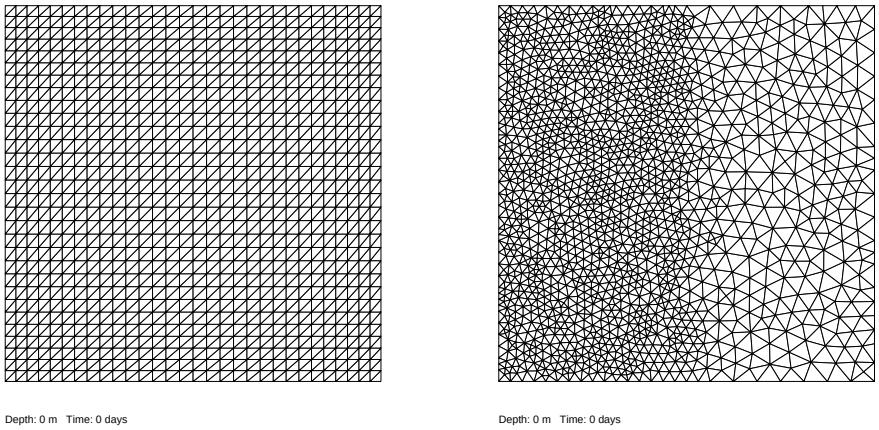

Figure 3.14: Surface grids for advection experiments. The basin size L is 2000km.

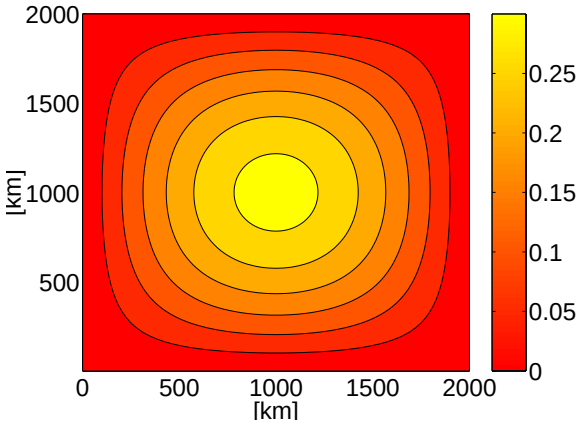

Figure 3.15: Streamlines (in Sv) of the velocity field in the advection experiment. This field is independent of depth and satisfies the no normal flow conditions at the boundaries.

Figure 3.16 compares the results obtained with the two grids. Shape and magnitude are in close agreement. Even on the passage through the low resolved region of the unstructured mesh the model is able to represent the temperature anomaly rather well.

3.3.3 Tracer conservation and overshooting

The presence of artificial extrema in tracer fields is called overshooting and its minimisation is an especially important aspect when biological tracers are modelled. In finite difference context unphysical oscillations can be traced back to the Peclet number $\mathrm{Pe} = h\,|\boldsymbol{u}|/(2A_h) = \mathrm{Re}/2$ (see, e.g., Roache, 1972). It can be shown that oscillations occur if the Peclet number increases 1. In the following we investigate occurrence of temperatures below the lowest initial temperature in the model. Figure 3.17 displays the structure of temperature values below the minimum initial temperature of 20°C . A time series of the lowest temperature at each time step is shown in figure 3.18, in the unstructured case especially strong overshoots are associated to situations where most of the anomaly is located in the low resolved area. The magnitude of overshooting takes bigger values in the unstructured grid which can be explained by the size of Peclet numbers shown in figure 3.19. Thanks to diffusion the overshooting decays with increasing time and becomes negligible after sufficient integration. The minimal temperature increases with time due to spreading of the temperature anomaly.

Tracer conservation

Figure 3.20 compares the relative error in total tracer content for both grids. In the regular case the error saturates and ends with a relative error of 10^{-8}. In the unstructured grid the error is somewhat bigger and reaches about 10^{-5} after about three years of integration. This value although much bigger than in the regular case is still small when compared to the error in determining boundary conditions from observations or our knowledge of the mean ocean state.

3.3.4 Conclusions

The results of this section can be summarised as follows.

- Like in the CTCS scheme overshoots occur in the FEOM_0 advection scheme if the cell Peclet number is larger than one.
- FEM scheme advects an anomaly with comparable result in shape and magnitude independent of the structure of the grid.
- If the Courant number is close to one or bigger, the FEOM_0 scheme is stable but develops huge implicit diffusion. To provide sufficient accuracy it should be used with small Courant numbers.

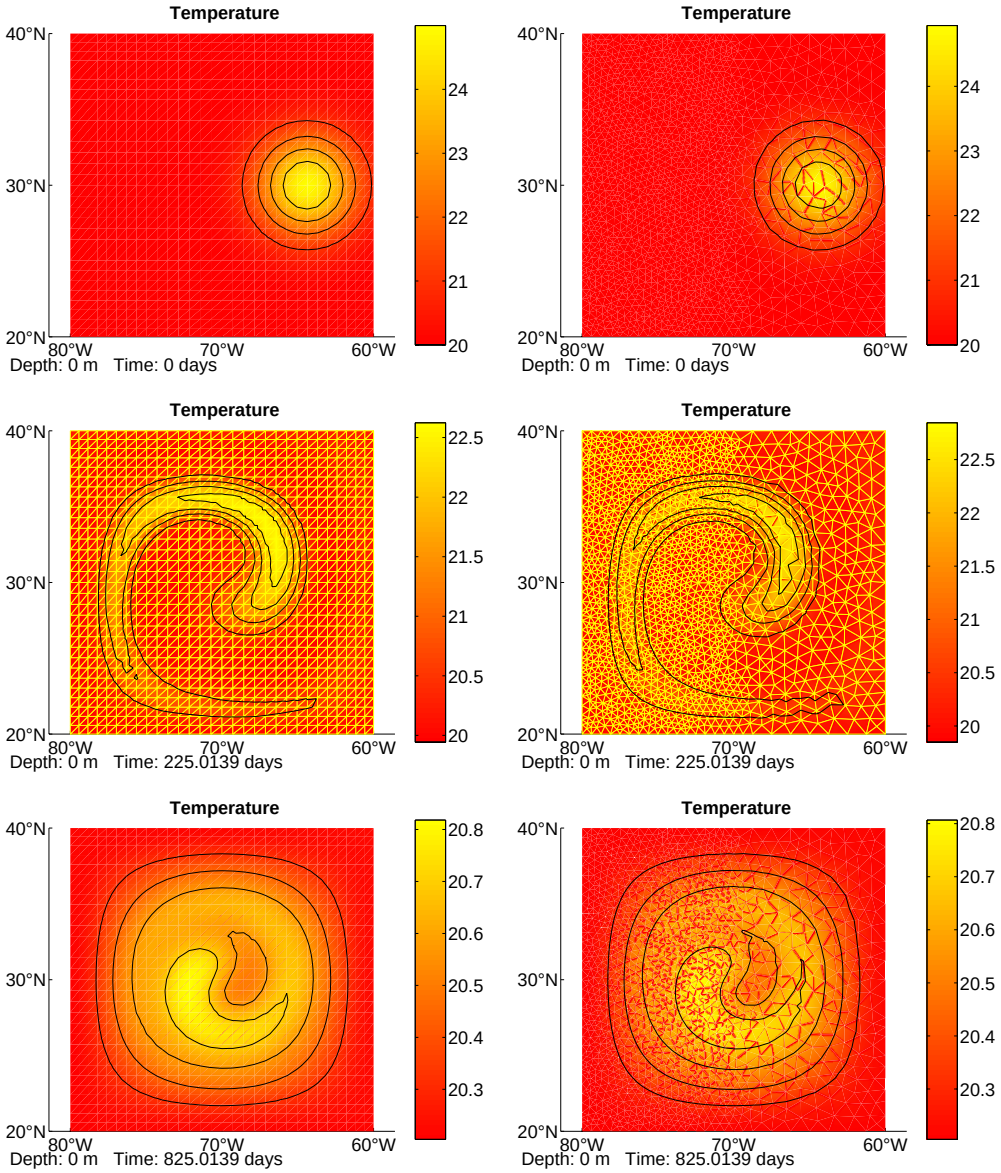

Figure 3.16: Temperature field (in °C) during advection experiment after 0, 225 and 800 days. The spreading of the anomaly is due to the finite diffusivity $K_h = 500$ m^2/s

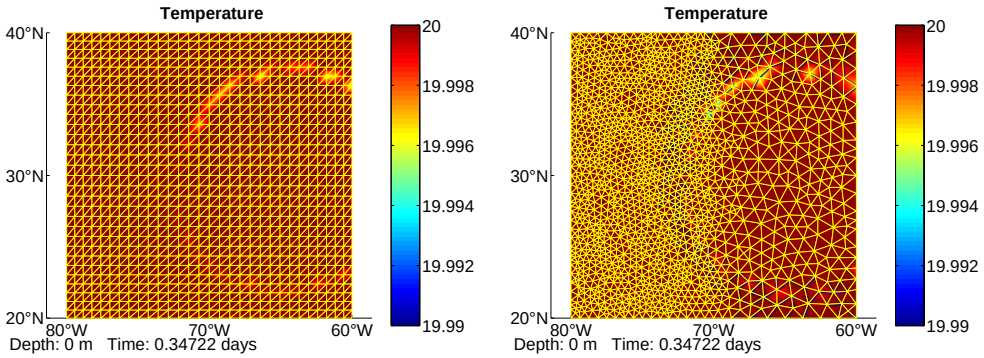

Figure 3.17: Initial structure of unphysical minimums in the temperature field (given in °C) resulting from deficiencies in reproducing the prescribed shape of the anomaly in the regular (left) and unstructured (right) grid. The main error is associated with large triangles in the unstructured case.

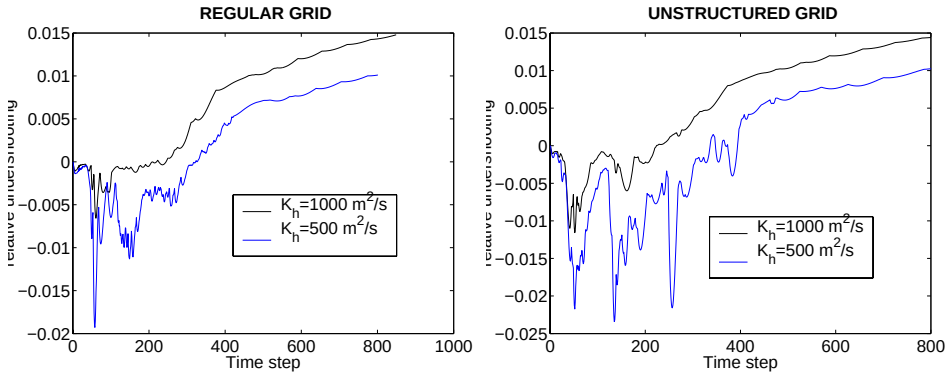

Figure 3.18: Time series of overshooting relative to 20°C in unstructured and regular grid. The positive trend at large time is due to diffusive spreading of anomaly.

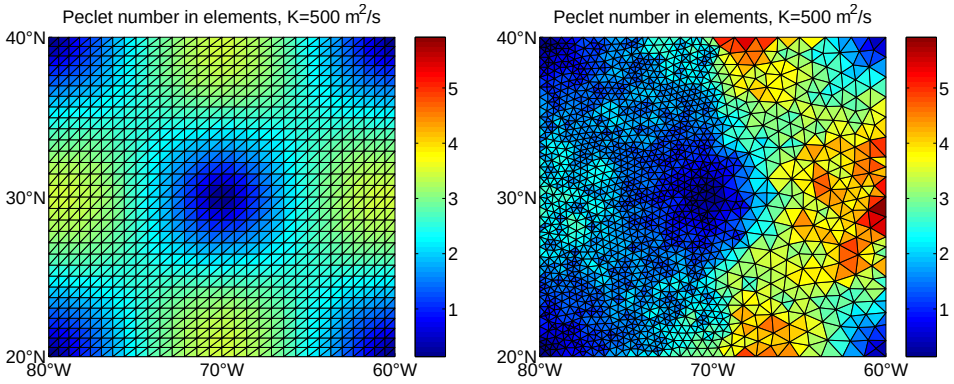

Figure 3.19: Peclet numbers in case of regular and unstructured grid for diffusivity $K_h = 500$ m^2/s.

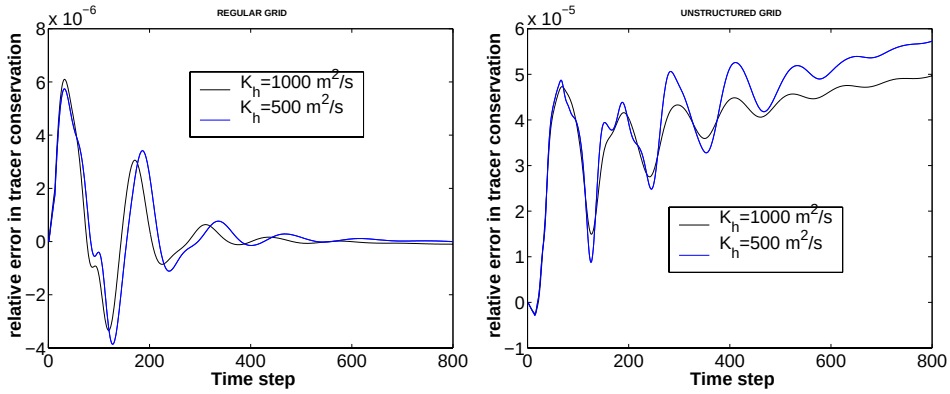

Figure 3.20: Relative error in globally integrated tracer content for about 800 days of integration time.

Part II

The Experiments

Chapter 4

Wave Propagation

4.1 Introduction

Wave phenomena are observed in the ocean in a vast range of temporal and spatial scales. The hierarchy of oceanic waves reaches from ripples on the surface due to surface tension up to planetary waves with periods of several months. The major restoring forces are gravity, Coriolis- and buoyancy force. Waves are the main means to propagate disturbances and a systematically wrong representation of waves in a numerical model leads to faulty response to time varying forcing fields.

- **waves independent of rotation**
  - gravity waves
- **only existing in the presence of rotation ($f \neq 0$)**
  - Kelvin waves (only at the equator or along lateral boundaries)
  - Poincaré waves
- **only existing in the presence of a meridional variation of the Coriolis force ($\beta \neq 0$)**
  - Rossby waves

Table 4.1: Some types of waves in the ocean

A thorough theoretical treatment of ocean waves can be found in the text books by LeBlond and Mysak (1978), Pedlosky (1987) or Cushman-Roisin (1994),

the content of the next section is restricted to a presentation of the background for the performed model runs.

Numerical aspects

There are numerous studies on the numerical representation of waves in finite difference models (see, e.g., Hsieh et al. (1983), Dukowicz and Smith (1994)). For regular grids dispersion properties can be computed and the representation of different kinds of waves depends on the arrangement of variables on the grid and space-time discretisation. The most common grids are the so-called Arakawa "A-", "B-" and "C-"grids (see Arakawa (1966) or p. 94 of Haidvogel and Beckmann (1999)) which use different staggering of the variables in the mesh. The arrangement of variables in the finite element model corresponds to the Arakawa A-grid but for unstructured meshes it is generally impossible to write down a dispersion relation, and different parts of the domain could have different wave propagation properties.

Indeed a frequently mentioned criticism of FEM as applied to ocean modelling is the problem of unphysical wave scattering in unstructured grids (see for example Griffies et al. (2000)). Therefore it is necessary to investigate the propagation of waves relevant to large scale ocean modelling on grids with varying nodal density. It is the purpose of this chapter to contribute some experiments to the discussion on this subject.

The wave propagation problem treated in this chapter were chosen from an inter comparison between the spFLAME version of the widely used primitive equation model MOM (**M**odular **O**cean **M**odel) and the low order model BARBI performed by Dirk Olbers and Carsten Eden (see Olbers and Eden, 2003).

4.2 Some theoretical background on waves in the ocean

While investigating wave phenomena in the ocean we will consider motions of small amplitude, (i.e. low Rossby numbers) that evolve rather quickly in time. Therefore in the following we will neglect viscosity and nonlinear terms in governing equations but retain temporal derivatives.

4.2.1 Barotropic Kelvin waves

Barotropic waves involve motion of the fluid column as a whole. The density stratification is then not important and could be neglected to simplify derivations. In this case the momentum and vertically integrated continuity equations (2.20)-(2.22) reduce to the linearised rotating shallow water equations for quasi 2D

motions. In this section the meridional variation of the Coriolis parameter (β-effect) will be ignored, $f = f_0 = \text{const}$.

$$\partial_t u - f_0 v = -g\,\partial_x \zeta,$$

$$\partial_t v + f_0 u = -g\,\partial_y \zeta,$$

$$\partial_t \zeta + H \nabla \cdot \boldsymbol{u} = 0.$$

Kelvin waves need the support of a lateral boundary. If this boundary is directed into positive y direction and the cross border velocity u is chosen to be zero everywhere, the elimination of the surface displacement leads to a single equation for v:

$$\partial_{tt}^2 v = c^2\,\partial_{yy}^2 v,$$

where

$$c = \sqrt{gH}.$$

General solutions of this wave equation are readily obtained and substitution into the equation for ζ gives the solution localised in the vicinity of the western wall (x=0).

$$u = 0,$$

$$v = cF(y + ct)\exp(-x/R),$$

$$\zeta = -HF(y + ct)\exp(-x/R),$$

where

$$R = \frac{c}{f_0} \tag{4.1}$$

is known as the external Rossby deformation radius and F is an arbitrary function. This solution corresponds to a wave that propagates southward. There is another branch, with $v = cG(y - ct)\exp(x/R)$, $\zeta = -HG(y - ct)\exp(x/R)$, which represents a wave localised along the eastern boundary and propagating northward. Thus the direction of propagation is always with the boundary to the right in the northern hemisphere.

Kelvin waves are non dispersive, the dispersion relation is shown below in figure 4.1. Waves of this kind are present along boundaries of all models but the representation of the phase velocity depends heavily on the resolution of the Rossby radius. Also H is never constant which modifies the solution. Taking $H = 4000$ m one obtains $c = 200$ m/s. Thus barotropic Kelvin waves are very fast compared to typical velocities observed in the ocean. The same H results in $R \approx 2000$ km which gives an estimate on the spatial localisation scale.

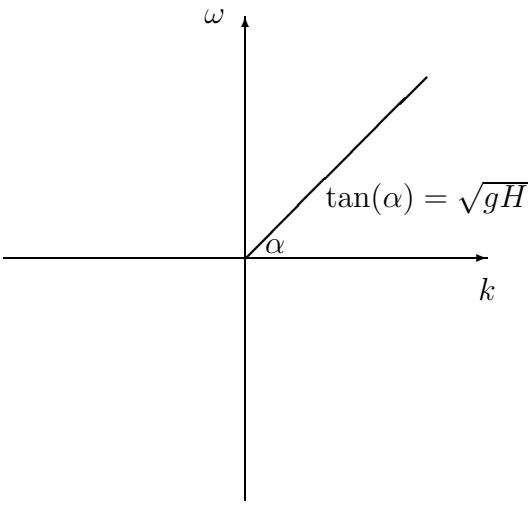

Figure 4.1: Dispersion relation of Kelvin waves.

4.2.2 Barotropic Rossby waves

Now the β-plane approximation will be reconsidered, that is f_0 in the linearised, rotating shallow water equations of the preceding section will be replaced by

$$f = f_0 + \beta_0 y.$$

The result is a set of differential equations with non constant coefficients but after some manipulations a Fourier type solution can be obtained with the dispersion relation

$$\omega = -\beta_0 R^2 \frac{k_x}{1 + R^2({k_x}^2 + {k_y}^2)} \tag{4.2}$$

where R is given by (4.1) and k_x and k_y are the wave numbers in x- and y-direction. It is called the barotropic Rossby wave. The zonal wave speed is given by

$$c_x = \frac{\omega}{k_x} = \frac{-\beta_0 R^2}{1 + R^2({k_x}^2 + {k_y}^2)}.$$

This expression is always negative and implies a westward phase propagation. Nevertheless the zonal component of the group velocity $\nabla_{\boldsymbol{k}}\omega$ can have both signs.

Long waves $R^2({k_x}^2 + {k_y}^2) \ll 1$ propagate strictly westward with a phase velocity

$$c = -\beta_0 R^2.$$

which is about -40 m/s, and does not depend on l and m. These waves are relatively fast and cross for example the zonal extent of the Northern Atlantic in about two days.

4.2.3 Baroclinic Rossby waves

The experiments below are mostly concerned with the propagation of the first baroclinic mode of a Rossby wave in a stratified ocean. These slow waves depend strongly on the density stratification of the water column so we will consider a layer of stratified fluid with $\rho = \bar{\rho}(z)$. In the presence of waves, the corresponding density field contains a large part due to the main stratification and a small correction term

$$\rho(x, y, z, t) = \bar{\rho}(z) + \rho'(x, y, z, t),$$

where $|\rho'| \ll \bar{\rho}$. The stratification is characterised by the buoyancy frequency as follows. If a parcel of fluid is displaced vertically from its equilibrium position in stratified fluid it is counteracted by the buoyancy force proportional to the displacement. As a result, it will start an oscillation with a frequency that is determined by the ambient density derivative. For a linear equation of state which depends only on temperature the frequency is given by (see, e.g. Salmon, 1998)

$$N^2 = -\frac{g\ \partial_z \bar{\rho}}{\rho_0}.$$

N is known as the Brunt-Väisälä frequency. For a linear temperature stratification and the equation of state given by (2.17) the Brunt-Väisälä frequency is constant in depth.

The simplest way to introduce the baroclinic Rossby wave is to use the quasi-geostrophic approximation (see Pedlosky (1987), Salmon (1998)). To this end it is assumed that there is a background density stratification $\bar{\rho}$ maintained against time and small disturbances ρ'. The corresponding pressure disturbance p' gives rise to motion which is assumed to be mainly geostrophic, i.e., the circulation is approximately given by

$$u = -\frac{1}{f_0 \rho_0}\, \partial_y p', \quad v = \frac{1}{f_0 \rho_0}\, \partial_x p'$$

with small ageostrophic corrections. These corrections are necessary since the assumption of geostrophy results for a flat bottom in zero vertical velocities. The quasi-geostrophic approximation requires some balance of these corrections in the limit of small Rossby numbers. These approximations allow a reformulation of the equations of motion in terms of the stream function

$$\Psi = \frac{1}{\rho_0 f_0} p'.$$

The result is the quasi-geostrophic vorticity equation

$$\partial_t q + J(\Psi, q) = 0, \tag{4.3}$$

(see chapter 15 of Cushman-Roisin, 1994, for details). J denotes the Jacobi operator and q is called the quasi-geostrophic potential vorticity. It is given by

$$q = \nabla^2\Psi + \frac{f_0^2}{N^2}\,\partial_{zz}^2\Psi + f_0 + \beta_0 y.$$

The potential vorticity contains the relative vorticity $\nabla^2\Psi = \nabla \times \boldsymbol{u}$, the planetary vorticity term $f_0 + \beta_0 y$ and a term representing vortex tube stretching in a stratified fluid. Once Ψ is determined the velocity vector is given by

$$u = -\,\partial_y\Psi, \;\; v = \,\partial_x\Psi, \;\; w = -\frac{f_0}{N^2}(\,\partial_{tz}^2\Psi + J(\Psi,\,\partial_z\Psi)), \tag{4.4}$$

whereas pressure- and density anomalies are given by

$$p' = \rho_0 f_0 \Psi, \;\; \rho' = \frac{\rho_0 f_0}{g}\,\partial_z\Psi. \tag{4.5}$$

Restriction to small amplitude motions allows a linearisation of equation (4.3)

$$\partial_t(\nabla^2\Psi + \frac{{f_0}^2}{N^2}\,\partial_{zz}^2\Psi) + \beta_0\,\partial_x\Psi = 0.$$

We assume that there are no lateral boundaries and the boundary conditions at the sea surface and at the bottom are given by

$$\partial_t\zeta = w \quad \text{in} \quad z = 0, \tag{4.6}$$

$$w = 0 \quad \text{in} \quad z = -H. \tag{4.7}$$

Assuming a solution with separated dependencies of the kind

$$\Psi(x, y, z, t) = a(z)\cos(k_x x + k_y y - \omega t)$$

gives an equation for a:

$$\frac{d^2a}{dz^2} - \frac{N^2}{{f_0}^2}\left({k_x}^2 + {k_y}^2 + \frac{\beta_0 k_x}{\omega}\right)a = 0$$

with translated boundary conditions

$$\frac{da}{dz} + \frac{N^2}{g}a = 0 \quad \text{in} \quad z = 0, \tag{4.8}$$

$$\frac{da}{dz} = 0 \quad \text{in} \quad z = -H. \tag{4.9}$$

The solution $a(z)$ is given by

$$a(z) = A\cos(k_z(z+H)) \tag{4.10}$$

and the dispersion relation

$$\omega = -\frac{\beta_0 k_x}{k_x^2 + k_y^2 + \frac{k_z^2 f_0^2}{N^2}}.$$

An expression for the vertical wavenumber k_z is obtained from the boundary conditions

$$\tan k_z H = \frac{N^2 H}{g}\frac{1}{k_z H}.$$

The last expression gives an infinite number of solutions. The first one is obtained under the assumption that $k_z H \ll 1$ and is approximated by

$$k_{z,0} = \frac{N}{\sqrt{gH}}, \;\; \omega_0 = -\frac{\beta_0 k_x}{k_x^2 + k_y^2 + \left(\frac{f_0}{\sqrt{gH}}\right)^2}.$$

This dispersion relation coincides with (4.2) and thus represents the barotropic wave. Indeed for typical ocean parameters $N = 10^{-3}$ s^{-1}, $H = 4000$ m, $k_z H = 0.02$, and $\cos(k_z(z+H))$ is very close to unity. It could be easily inferred that $k_z H = 0$ in the rigid lid case.

All further solutions represent baroclinic waves, the wave numbers are approximately

$$k_{z,n} = n\pi/H, \;\; n = 1, 2, 3, \ldots$$

with dispersion relations

$$\omega_n = -\frac{\beta_0 k_x}{k_x^2 + k_y^2 + \left(n\pi\frac{f_0}{NH}\right)^2} \tag{4.11}$$

and westward phase velocities

$$c_n = \frac{\omega_n}{k_x} = -\frac{\beta_0}{k_x^2 + k_y^2 + \left(n\pi\frac{f_0}{NH}\right)^2}.$$

The quantities $R_n = NH/(f_0 n)$ are called internal Rossby deformation radii. They are much smaller than R, so baroclinic Rossby waves propagate much slower than the barotropic one. In the limit of long waves, $c_1 \approx -\beta_0 R_1^2/\pi^2$ is several cm per second.

4.2.4 Numerical representation of planetary waves

Numerical solutions of the propagation of Rossby waves in two dimensions were investigated in Dukowicz (1995) (see also Haidvogel and Beckmann, 1999). For different staggered grids with constant step size the resulting numerical dispersion relations can be calculated and the resulting frequency error $(\omega_A - \omega)/\omega$ in dependence on horizontal wave numbers for the Arakawa A-grid are shown in figure 4.2. Here ω is the true frequency and ω_A denotes the approximation on A-grid. Because of the westward propagation of these waves only negative k_x values are considered. Furthermore the analysis is restricted to waves with wavelength longer than four times the grid step, and the ratio $\Delta x/R$ equals 1. The frequency is mostly underestimated.

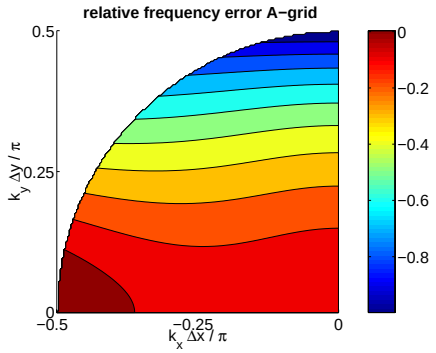

Figure 4.2: Relative frequency error (colour) in A-grid in representing the frequency of Rossby waves as a function of the wave numbers, according to Dukowicz (1995). Due to the westward propagation of these waves only negative x-wave numbers are taken into account.

Figure 4.3 shows the relative frequency error in dependence upon the resolution of the Rossby radius. A very good resolution leads to too high frequencies whereas a bad resolution leads to low frequencies. As already mentioned such an analysis is not straightforward in unstructured grids but the resulting frequencies and thus wave speeds should be expected to depend on the grid resolution.

4.3 The experiments

The experiments in the following consider the propagation of a temperature disturbance in a stratified ocean on a β-plane. The bottom is flat, the linear equation of state (2.17) is used, the background stratification is linear and nonlinear terms are neglected. The temperature anomaly is horizontally Gaussian as shown in figure 4.4. As follows from (4.5) the density perturbation is linked to Ψ_z, which is negligible in the barotropic mode. That is why it excites only slow baroclinic Rossby waves. The vertical structure in experiment DIST1 is z-independent and

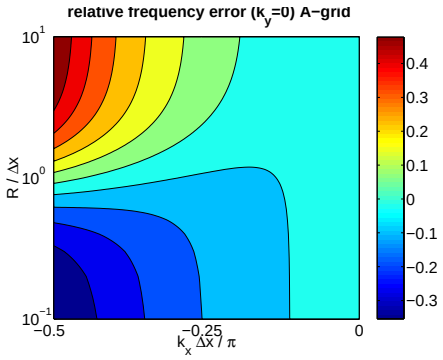

Figure 4.3: Relative frequency error in A-grid for l=0 as a function of the resolution of the Rossby radius according to Dukowicz (1995).

in experiment DIST2 exponentially decaying in the vertical with an e-folding scale of 500 m.

Experiment DIST1 was performed using a regular horizontal grid and the unstructured grid already used in the advection experiment, it is shown in figure 3.14. The characteristics of both experiments are summarised in table 4.2. Density (temperature) perturbation excites baroclinic Rossby waves. This can be

Experiment	DIST1	DIST2
depth [m]	4000	5375
#levels	20	46
ΔT [K]	18.5	18.5
$\Delta\bar{\rho}$ [kg/m^3]	3.7	3.7
d$\bar{\rho}$/dz [kg/m^4]	9.26 10^{-4}	6.89 10^{-4}
N [1/s]	0.003	0.0026
R_{center} [km]	126.4	117.6
c_1 [m/s]	0.032	0.028

Table 4.2: Parameters of the wave propagation experiments. The parameters of DIST2 are close to those of the corresponding MOM experiment.

easily seen in the rigid lid approximation as there is no projection of barotropic mode on Ψ_z (which according to (4.5) describes the density perturbation). This remains true in the free surface case yet showing it is not straightforward as $a'(z)$ corresponding to different $k_{z,n}$ are not orthogonal.

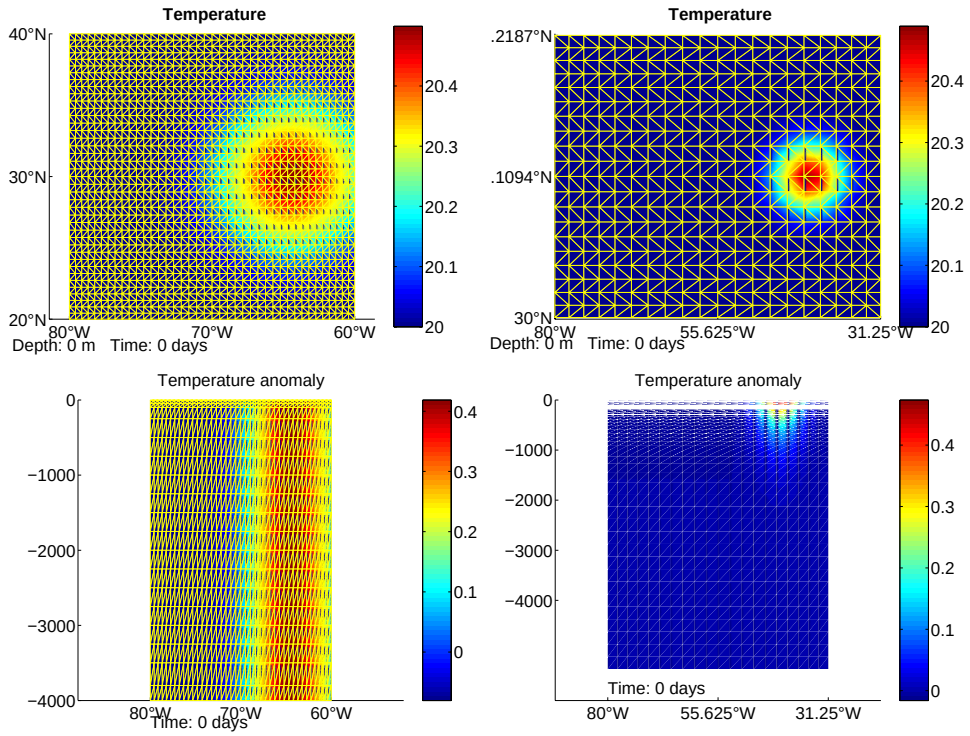

Figure 4.4: Initial temperature perturbation in horizontal and vertical section for experiments DIST1 (left panels) and DIST2. In the vertical a linear background stratification is prescribed.

4.3.1 Experiment DIST1

Stratification

The temperature stratification is chosen to be linearly decreasing with 20 °C at the surface and 2 °C at the bottom.

From (2.17), the z-derivative of the density can be evaluated:

$$\partial_z \rho = -7.2 \cdot 10^{-4} \text{ kg/m}^4$$

and for a mean density of 1000 kg/m^3 the Brunt-Väisälä frequency takes the value

$$N = 0.003 \text{ s}^{-1}.$$

The depth of the basin is 4000 m, $f_0 = 7.27 \cdot 10^{-5}$ s^{-1}. This gives for the Rossby radius of the first baroclinic mode

$$R_1 = \frac{NH}{f_0} = 126.4 \text{ km}$$

and

$$c_1 = \frac{\beta_0 R^2}{\pi^2} = 0.032 \text{ m/s} = 2.8 \text{ km/d}$$

for its westward phase velocity with $\beta_0 = 2 \cdot 10^{-11}$ (ms)$^{-1}$.

Initial velocity field

The initial temperature disturbance in experiment DIST1 results after 2 days of integration in the velocity field shown in figure 4.5. In order to explain what

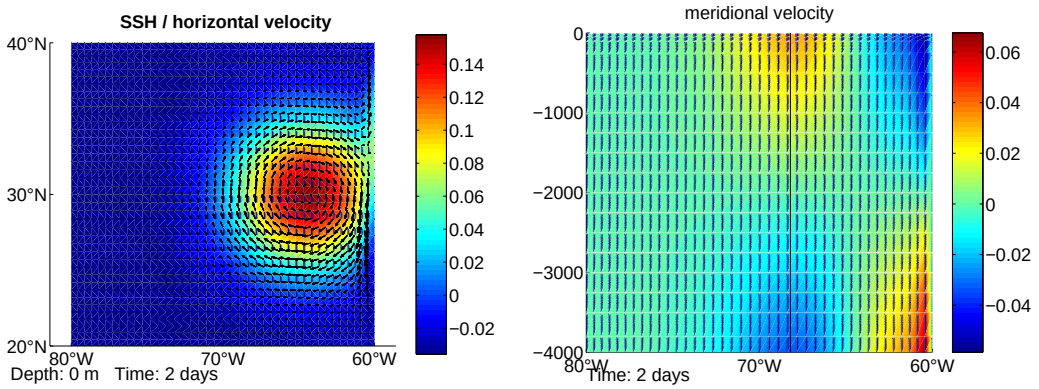

Figure 4.5: Sea surface height (SSH in [m]) and horizontal velocity fields (in m/s) after 2 days of integration. The left panel shows SSH and velocity at the surface. In the right panel the meridional velocity in the central zonal section is depicted. It shows a vortex with anticyclonic rotation in the upper half and the rotation of opposite sense in the lower half.

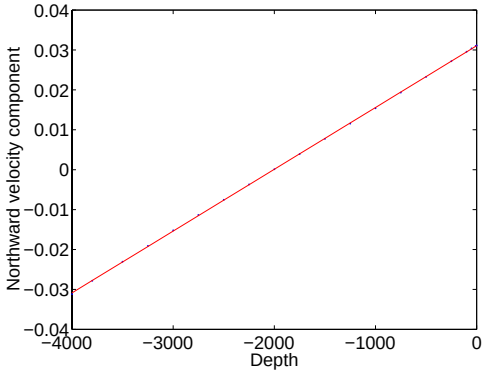

Figure 4.6: Northward velocity component (in m/s) in the line indicated in figure 4.5. The line is a regression curve fitted to the model results. It shows that the model reproduces the linear dependency very well.

is going on initially, it is convenient to consider the density anomaly $\Delta\rho(x, y)$ in a horizontally unbounded domain on an f-plane. In this case the thermal wind relation (obtained by combining geostrophic and hydrostatic approximations, see

Pedlosky (1987), Salmon (1998)) gives

$$\partial_z u = -\frac{g}{f\rho_0}\,\partial_y \Delta\rho(x,y), \quad \partial_z v = \frac{g}{f\rho_0}\,\partial_x \Delta\rho(x,y).$$

Vertical integration results in the velocity field

$$u = -\frac{gz}{f\rho_0}\,\partial_y \Delta\rho + u_0, \quad v = \frac{gz}{f\rho_0}\,\partial_x \Delta\rho + v_0.$$

This is a rotation starting from u_0, v_0 at the surface with a linear dependence on depth. However initially the relative vorticity in the whole domain is zero and it is impossible to change the barotropic vorticity with internal forcing given as gradients at all as can be seen from the momentum equations

$$\partial_t \boldsymbol{u} + \boldsymbol{f} \times \boldsymbol{u} + \nabla(p/\rho_0 + g\zeta) = 0,$$

as vertical integration and calculation of the curl gives

$$\partial_t \int \boldsymbol{\omega}_z \,\mathrm{dz} + \boldsymbol{f}\nabla \cdot \boldsymbol{U} = \partial_t \int \boldsymbol{\omega}_z \,\mathrm{dz} = 0.$$

Now, requiring $\int \omega_z \,\mathrm{dz} = 0$ gives

$$\mathrm{curl}\,\boldsymbol{u}_0 = -\frac{H}{2}\mathrm{curl}\,(-\,\partial_y \Delta\rho,\, \partial_x \Delta\rho)$$

with the solution

$$u_0 = -\frac{gH}{2f\rho_0}\,\partial_y \Delta\rho, \quad v_0 = \frac{gH}{2f\rho_0}\,\partial_x \Delta\rho.$$

By substituting this solution into the momentum equation one obtains

$$g\nabla\zeta = -\nabla p/\rho_0|_{z=-H/2},$$

and hence

$$\zeta(x,y) = -\frac{\Delta\rho(x,y)}{\rho_0}\frac{H}{2}.$$

The actual velocity field is given by

$$u = -\frac{g\,\partial_y \Delta\rho}{f\rho_0}(z + H/2), \tag{4.12}$$

$$v = \frac{g\,\partial_x \Delta\rho}{f\rho_0}(z + H/2). \tag{4.13}$$

Pressure gradient and sea surface height work together in such a way that the resulting circulation is linear with depth and cancels at mid depth.

Although the experiments below are carried out on a β-plane the arguments presented above remain approximately valid as can be seen in figure 4.6.

Propagation of the disturbance

The goal of this section is some understanding of the propagation by expanding the initial disturbance into a series with respect to the eigenmodes (4.10). To simplify the discussion we consider the rigid-lid approximation where $k_{z,0} = 0$ and expressions for $k_{z,n}$ are exact for $n > 0$.

The density disturbance in experiment DIST1 is z-independent and given in a coordinate system with origin in the centre of the disturbance by

$$\rho_{ini} = -\Delta\rho \exp(-|\boldsymbol{r}|^2/2\alpha^2)$$

where α is given by the radius of the disturbance, $\Delta\rho$ denotes the maximal density difference and $\boldsymbol{r} = (x, y)$. Representing ρ_{ini} as $\rho_{ini} = \rho_{ini}(z)\rho_{ini}(x, y)$ we can expand $\rho_{ini}(z)$ as

$$\rho_{ini}(z) = \sum_{n=1}^{\infty} A_n a_n'(z)$$

where $a_n(z)$ are the eigenmodes $a(z)$ corresponding to $k_{z,n}$ and ω_n of section 4.2.3. Since the functions $a_n'(z)$ are orthogonal in the rigid-lid case, one finds

$$A_n = \Delta\rho \frac{\int a_n'(z)\,\mathrm{dz}}{\int (a_n')^2\,\mathrm{dz}} = -\frac{4\Delta\rho H}{(\pi n)^2},$$

such that

$$\Psi_{ini}(z) = \frac{g}{f_0\rho_0} \sum_{n=1}^{\infty} A_n a_n(z).$$

Expanding now the horizontal part of ρ_{ini} (or Ψ_{ini}) by means of the Fourier integral into wave vectors $\boldsymbol{k} = (k_x, k_y)$, we can write the solution for Ψ in all subsequent moments of time as

$$\Psi = \frac{g}{f_0\rho_0} \sum_{n=1}^{\infty} \int_{\mathbb{R}^2} A_n \exp(-i\omega_n(\boldsymbol{k})t + i\boldsymbol{k}\cdot\boldsymbol{r})\hat{\Psi}_{ini}(\boldsymbol{k})\,\mathrm{d}\boldsymbol{k},$$

where

$$\hat{\Psi}_{ini}(\boldsymbol{k})\,\mathrm{d}\boldsymbol{k} = \frac{2}{(2\pi)^2} \int_{\mathbb{R}^2} \rho_{ini}(x, y) \exp(-i\boldsymbol{k}\cdot\boldsymbol{r})\,\mathrm{d}\boldsymbol{r}.$$

The solution for Ψ is thus given by

$$\Psi(x, y, z, t) = \frac{g\Delta\rho}{\rho_0 f_0} \frac{\alpha}{8\sqrt{\pi}} \sum_{n=0}^{\infty} \frac{4H}{(2n+1)^2\pi^2} \cos((2n+1)\pi z/H) \int_{\mathbb{R}^2} \exp(-\alpha^2|\boldsymbol{k}|^2/2) \exp i(\boldsymbol{k}\cdot\boldsymbol{r} - \omega_n(\boldsymbol{k})t)\,\mathrm{d}\boldsymbol{k}, \tag{4.14}$$

where $\omega_n(\boldsymbol{k})$ is given by (4.11). Such integrals can be approximated for large t by the method of stationary phase. We will not use it noting instead that since

the temperature anomaly is large compared to the Rossby radius we can neglect the terms $k_x^2 + k_y^2$ in the denominator of (4.11) and approximate

$$\omega_n \approx -\frac{\beta_0 k_x}{(n\pi)^2}\left(\frac{NH}{f_0}\right)^2 = -\frac{\beta_0 R_1^2 k_x}{n^2\pi^2}$$

The corresponding phase velocity in x-direction of the first baroclinic mode results in

$$c_1 = -\frac{\beta_0 R^2}{\pi^2} = -3.2 \text{ cm/s}.$$

Equation (4.14) describes a superposition of baroclinic eigenmodes propagating at constant velocities. Since A_1 is the largest and c_1 takes the biggest value, the first baroclinic mode will dominate the wave solution. The spatial structure of the first baroclinic mode with the cylindrical initial anomaly can be obtained for $n = 0$ from the solution above

$$\begin{aligned}
\Psi_1(x,y,z,t) &= \frac{g\Delta\rho}{\rho_0 f_0}\frac{\alpha}{8\sqrt{\pi}}\frac{4H}{\pi^2}\cos(\pi z/H) \\
&\quad \int_{\mathbb{R}^2} \exp(-\alpha^2|\boldsymbol{k}|^2/2)\exp i(\boldsymbol{k}\cdot\boldsymbol{r} - \omega_1(\boldsymbol{k})t)\,\mathrm{d}\boldsymbol{k}, \qquad (4.15)\\
w_1(x,y,z,t) &= -\frac{f_0\,\partial_{tz}^2\Psi_1}{N^2} = -\frac{g\Delta\rho}{\rho_0 N^2}\frac{4}{\pi}\sin(\pi z/H) \\
&\quad \int_{\mathbb{R}^2} \exp(-\alpha^2|\boldsymbol{k}|^2/2)\omega_1(\boldsymbol{k})\exp i(\boldsymbol{k}\cdot\boldsymbol{r} - \omega_1(\boldsymbol{k})t)\,\mathrm{d}\boldsymbol{k}, \qquad (4.16)\\
\rho_1(x,y,z,t) &= \frac{\rho_0 f_0}{g}\,\partial_z\Psi_1 = -\Delta\rho\frac{\alpha}{8\sqrt{\pi}}\frac{4}{\pi}\sin(\pi z/H) \\
&\quad \int_{\mathbb{R}^2} \exp(-\alpha^2|\boldsymbol{k}|^2/2)\exp i(\boldsymbol{k}\cdot\boldsymbol{r} - \omega_1(\boldsymbol{k})t)\,\mathrm{d}\boldsymbol{k}. \qquad (4.17)
\end{aligned}$$

The signature of the vertical velocity is shown in figure 4.7. The sinus shaped profile results in a deformation of the density surfaces which is largest at mid depth.

The propagation of the velocity anomaly is shown in figure 4.7. The cosine shaped vertical velocity profile obtained from $v_1 = \partial_x\Psi_1$ and (4.15) is well reproduced.

The cylindrical anomaly is expanded into eigenmodes as sketched in figure 4.8. The propagation of the density is depicted in figure 4.9 and in a three dimensional view at the end of the chapter in figure 4.16. It shows the signature of the first mode of this expansion. The phase velocity coincides very well with the theoretical value as can be seen in the left panel of figure 4.10 and figure 4.12. The propagation of the patches at the surface and bottom should be close to the phase velocity of the second mode $c_2 = c_1/4$. Figure 4.10 shows a comparison of the propagations of the temperature anomaly at mid depth (2000 m) and close

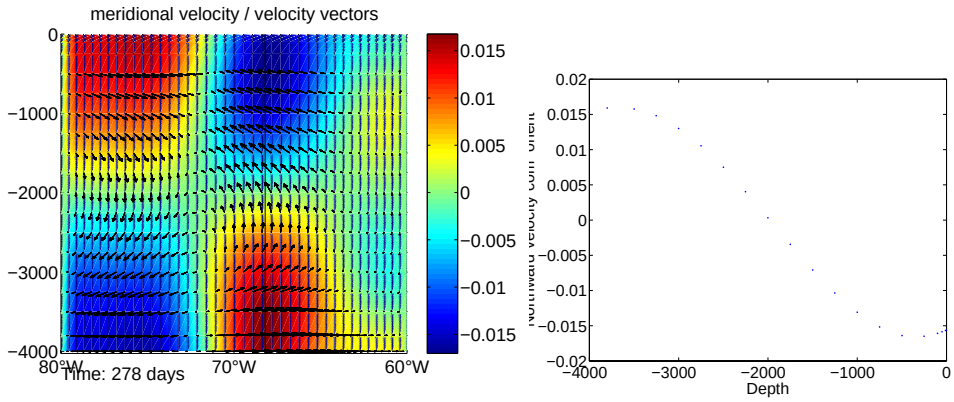

Figure 4.7: Signature of propagating first baroclinic mode after 278 days of integration. The left panel shows the meridional velocity (in m/s) together with the velocity vectors in the central zonal section. In the right panel the vertical profile of the v-component is shown in the line indicated in the left panel. It reproduces the predicted cosine shape rather well. Compare also the initial linear profile shown in figure 4.6.

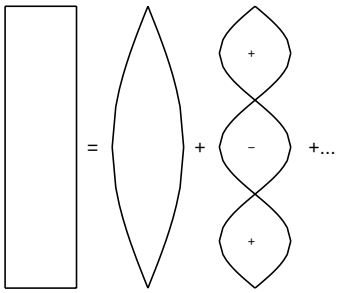

Figure 4.8: Sketch of the decomposition of the cylindrical anomaly into a series of sinus components.

to the surface (250 m). The propagation in upper ocean is slightly faster than c_2 but at this depth a superposition of first and second order modes leads to a faster motion.

Another point of interest is a comparison of structured and irregular grids. A comparison of model results for the temperature anomaly in runs with structured and unstructured grid is presented in figure 4.11. Shape and magnitude are fairly similar. However in obtaining the result it was very important to resolve the vertical structure of the wave fairly well. In the presented experiments 20 levels in the vertical were used, in experiments with 12 levels it turned out that the model was not able to represent the wave after about 80 days. Moreover in this case a bigger difference between structured and unstructured grids showed up. Nevertheless from the experiment shown in figure 4.11 it can be concluded that for resolved Rossby radius ($R_1/\Delta x \geq 1$) and an anomaly larger than R_1

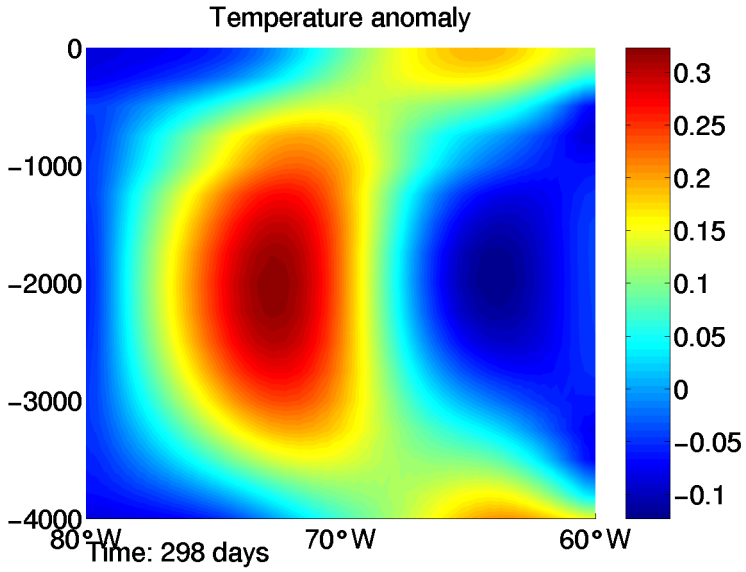

Figure 4.9: Signature of propagating wave after 298 days of integration. The temperature anomaly (in °C) is shown reproducing the vertical structure of the first baroclinic mode.

the results in structured and unstructured grid coincide very well provided the vertical resolution is sufficient.

Phase velocities in both grids are compared in Hovmöller diagrams in figure 4.12. It seems that the problem of different phase velocities in different parts of the grid is not severe in this case where the anomaly is well resolved in both parts of the grid. In the right panel only a slight increase of phase velocity is detected.

The boundary trapped wave

Davey et al. (1983) considered boundary trapped waves in the presence of lateral and vertical viscosity. In analytical considerations they found a wave which behaves like a Kelvin wave but shows a different phase velocity and obeys another dispersion relation. The same authors examined in Hsieh et al. (1983) the representation of such waves in numerical models with B- and C-grids.

In experiments DIST1 and DIST2 the resolution along the boundaries is too coarse to resolve Kelvin waves as described in section 4.2.1 with a time step of one hour. However "pseudo Kelvin waves" are present in model results. Such a wave moving around the basin starts from the initial disturbance at the eastern boundary. It is already present in figure 4.5 and the further propagation is shown in figure 4.13 for horizontally structured grids with resolutions 40×40 (left panel) and 20×20. Again the phase velocity depends on the resolution. The geometrically estimated phase velocities are 1.78 and 1.13 m/s. The same wave in the

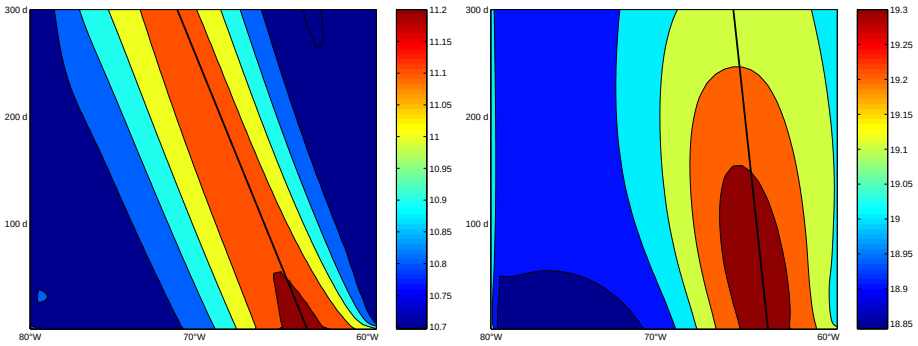

Figure 4.10: Propagation of temperature spot (in °C) in 2000 m (left panel) and 250m depth. The lines indicate first and second order phase velocities c_1 and c_2 respectively.

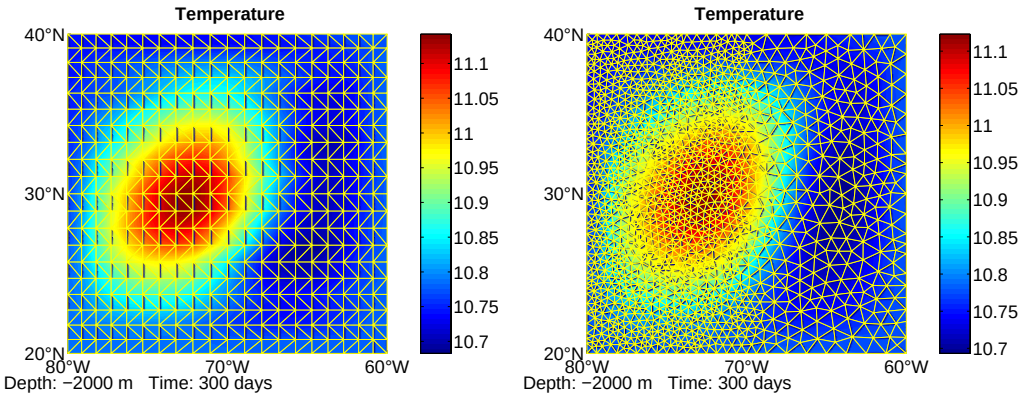

Figure 4.11: Comparison of the temperature field (in °C) in mid depth for structured and unstructured grid

unstructured grid is shown in figure 4.14. An increase of phase velocity occurs whenever the wave enters the high resolved part of the grid.

4.3.2 Experiment DIST2

A closely related experiment concerned with the propagation of the first baroclinic Rossby wave mode is investigated by Olbers and Eden (2003) for a comparison between the spFLAME version of the primitive equation ocean model MOM and a low order model (BARBI). In this case a vertically decaying anomaly is placed near the eastern boundary (see figure 4.4). The parameters are given in table 4.2. These experiments give a numerical reference solution well suited for a comparison to the results of the Finite Element Model. The initial conditions result in a propagation of a perturbation in the density structure that is visualised

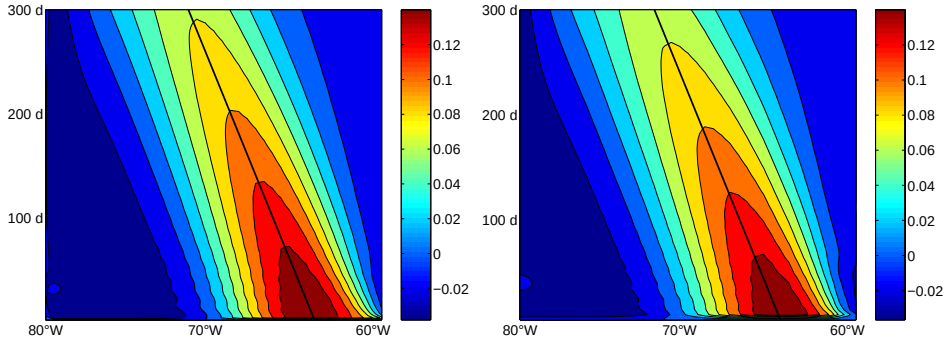

Figure 4.12: Comparison of Hovmöller diagrams for structured (left panel) and unstructured grid. The lines indicate the velocity of the first baroclinic mode c_1.

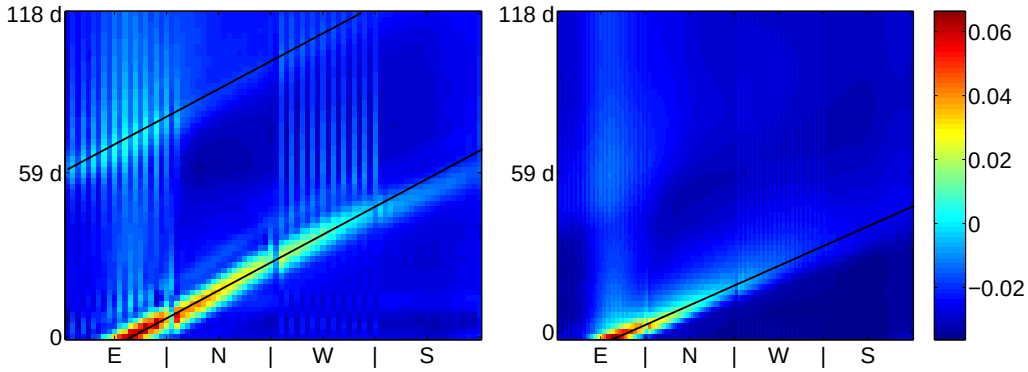

Figure 4.13: Comparison of Hovmöller diagrams of the boundary wave for low (20×20, left) and high resolution (40×40, right panel). It shows the displacement of sea surface height (in m) travelling around the basin. The sections along the abscissa indicate eastern, northern, western and southern boundaries.

by determining the first moment of the density field

$$\int_{-H}^{0} \rho(x, y, z) z \, \mathrm{dz}.$$

The propagation of this anomaly in MOM and FEOM_0 is compared in figure 4.15 which indicate that both models show comparable performance in modelling the wave propagation.

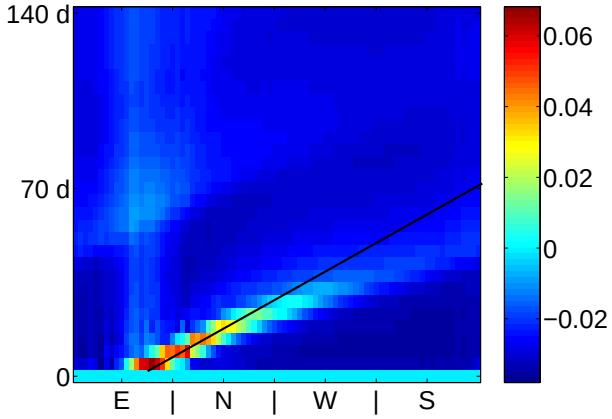

Figure 4.14: As in figure 4.13 but for the unstructured grid

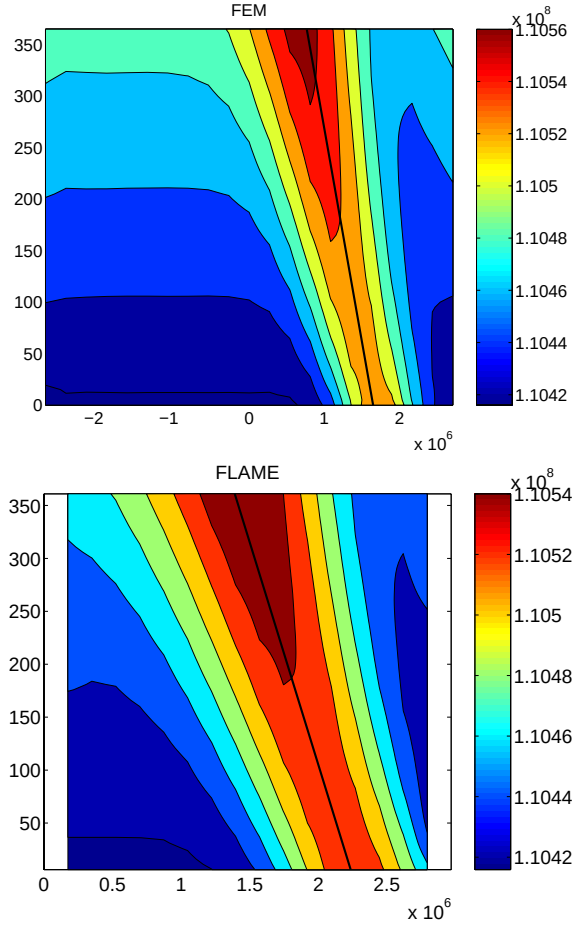

Figure 4.15: Comparison of the propagation of the anomaly in the first density moment in FEM and MOM. The line indicates in both cases the theoretical value of $c_1 = 28$ cm/s.

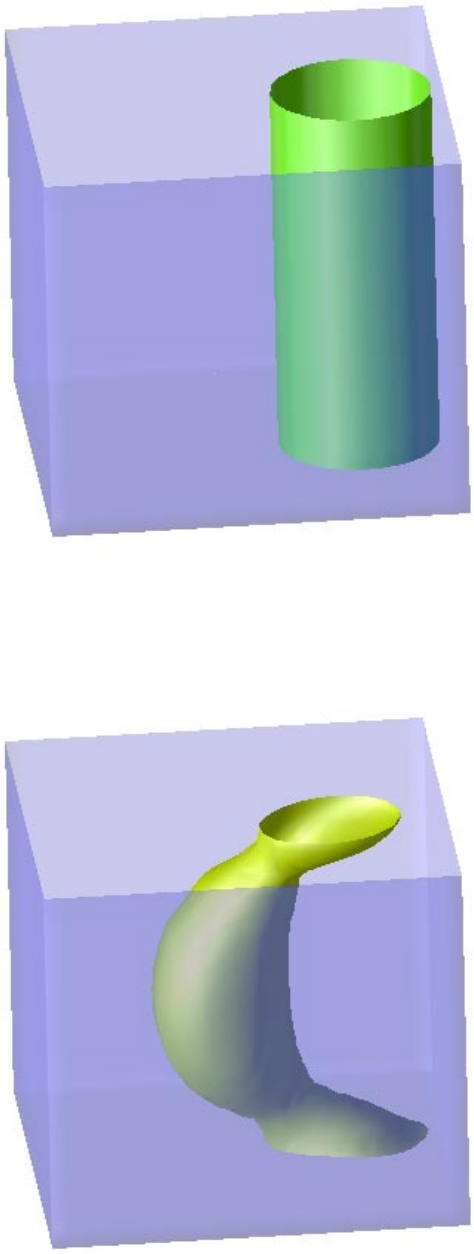

Figure 4.16: Three dimensional view of the 0.2 K isoline of the temperature anomaly in experiment DIST1 initially and after 200 days

Chapter 5

The Wind-Driven Circulation

5.1 Introduction

The next application of the finite element model is an ocean forced by wind stress at the surface. The first important contribution to this problem was due to Ekman (1905) who explained theoretically Fritjof Nansen's observation that sea ice is not moving parallel to the wind but with an angle to the wind direction.

The aim of later works was to explain the oceans vertically integrated transport by using observed wind fields. This large scale circulation in the upper ocean is characterised by large gyres in the main basins which show an intense current at the western coast for example the Gulf Stream in the North Atlantic and are diffuse and weak in the eastern parts.

In the forties Sverdrup (1947) considered the interior part of the ocean outside the western boundary current and derived a simple relationship between the meridional transport and the curl of the wind stress at the surface. Stommel (1948) and Munk (1950) considered the whole circulation in idealised settings and showed that the existence of a western boundary current is due to the meridional variation of the Coriolis force.

Since Bryan (1969) numerous studies considered the wind-driven circulation in analytical and numerical approaches taking into account the role of topography, stratification, nonlinearity and other topics. In particular, the two-dimensional problem of wind-driven circulation with finite elements was studied by LeProvost (1986).

Numerical intentions

One motivation for applying FEOM_0 to problems of the wind-driven circulation is the existence of analytical solutions for the (vertically integrated) transport as well as the vertical structure in special cases. These findings are well suited for a comparison to the model results. Although several features of these solutions are academic in nature and do not occur in real world applications (for example

boundary layers due to vertical walls), they nevertheless result from the governing equations and should be represented by the model.

On the other hand cases where analytical solutions are not easily accessible have been addressed with already established models. A comparison to the results of a numerical experiment using MOM that deals with the circulation of a stratified ocean in presence of a ridge (see Olbers and Eden, 2003) is contained in section 5.5.2.

5.2 Experimental setup

The problem under consideration in this chapter is the circulation in a rectangular domain under the influence of prescribed wind stress. The area of the basin is about 2000×2000 km^2, the depth in different experiments is 1 or 4 km.

The wind stress field is sine shaped in zonal direction as shown in the figure below. The origin of the Cartesian coordinates is chosen to be in the centre of the model domain, thus the wind stress is given by

$$\boldsymbol{\tau} = \begin{pmatrix} \tau_0 \sin\left(y\frac{\pi}{L_y}\right) \\ 0 \end{pmatrix}. \tag{5.1}$$

Boundary conditions

The wind stress enters equations of motion (2.20)-(2.22) through the boundary condition at the ocean surface given by

$$A_v\, \partial_z \boldsymbol{u}|_{z=0} = \frac{1}{\rho_0}\tau. \tag{5.2}$$

The boundary conditions will be chosen 'traditionally' as no normal flow on solid walls, no slip at eastern and western boundaries and free slip for the meridional velocity component at northern and southern boundaries. This choice reflects the situation of an ocean part bounded by continents in East and West but without lateral boundaries in North and South. Free slip boundary condition is assumed at the bottom.

Topics of interest

Although the wind stress directly affects only the upper layer via turbulent stresses it sets into motion the whole water column. The responsible mechanism is the convergence of surface water leading to a change in sea surface height. This implies a change of the barotropic pressure which affects fluid motion at all depths.

The questions addressed in section 5.3 are

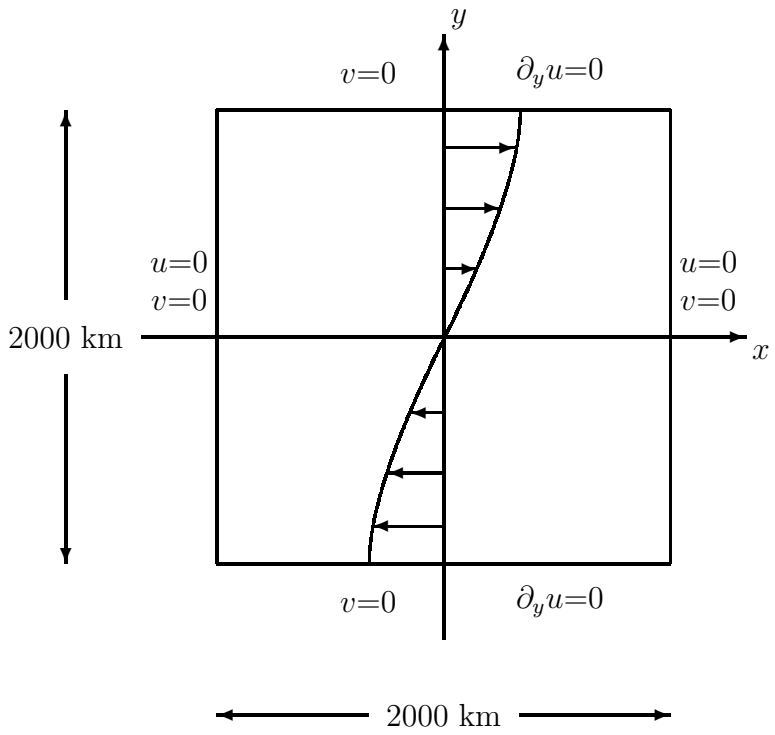

Figure 5.1: Surface of the model domain ($-L_x/2 \leqslant x \leqslant L_x/2$, $-L_y/2 \leqslant y \leqslant L_y/2$), boundary conditions and wind field

- What is the (vertically integrated) transport resulting from a given wind field?
- What is the vertical structure of the flow field?

These predictions are compared in section 5.5 to results of numerical simulations.

5.3 Theory for the case of homogeneous ocean with flat bottom

In the case of homogeneous fluid, the problem of wind-driven circulation is reduced to the dynamical part of the model. Starting point of our considerations are the equations of motion (2.20)-(2.22) in linearised form for an ocean of constant density. Since the focus is on the large scale circulation we assume both Rossby- and Ekman number to be small:

$$\mathrm{Ro} = \frac{U}{fL} \ll 1 \text{ and } E_H = \frac{A_h}{fL^2} \ll 1.$$

We consider stationary flows, as a consequence $w = 0$ at the surface, and divergence of vertically integrated transport is zero. Equations under consideration are therefore

$$\boldsymbol{f} \times \boldsymbol{u} = -g\nabla\zeta + \operatorname{div} \boldsymbol{A}\, \mathbf{grad}\, \boldsymbol{u}, \tag{5.3}$$
$$\operatorname{div} \boldsymbol{v} = 0,\ \nabla \cdot \boldsymbol{U} = 0$$

with boundary conditions specified above.

The dimensionless form of (5.3) (compare (2.25)-(2.26)) highlights the special structure of these equations: the highest derivatives are multiplied by very small coefficients (Ekman numbers). Therefore the geostrophic balance holds in most of the basin but in order to satisfy all boundary conditions the second order terms though multiplied by a small factor are important in thin layers close to the boundaries. In general such equations are treated by boundary layer methods (see for example Salmon, 1998, chapter 3.3) but first of all we consider the geostrophic part neglecting the effect of viscosity.

5.3.1 Vertically integrated transport

Sverdrup (1947) (see also chapter 1 of Pedlosky, 1996) considered the vertically integrated flow in the ocean interior arising from a given wind field. The assumptions are

- advection of momentum is neglected
- the horizontal viscosity is negligible
- the vertical velocity at the surface and at the bottom of the ocean is zero

In this case the stream function-vorticity equation (2.31) (obtained by taking the curl of (5.3) is given by

$$\beta\, \partial_x \Psi = \frac{1}{\rho_0} \operatorname{curl} \boldsymbol{\tau}. \tag{5.4}$$

The boundary conditions for U, V translate into

$$\Psi = 0 \qquad \text{on the whole lateral boundary,} \tag{5.5}$$
$$\partial_x \Psi = 0 \qquad \text{on eastern and western boundary,} \tag{5.6}$$
$$\partial^2_{yy} \Psi = 0 \qquad \text{on northern and southern boundary.} \tag{5.7}$$

Equation 5.4 is the famous Sverdrup balance linking the meridional transport velocity to the wind curl. Thus the transport stream function Ψ can be calculated by zonal integration, however from the Sverdrup theory it is not at all clear at which boundary to start the integration. From observations it is obvious that a boundary layer has to be expected at the western boundary (Gulf Stream). Therefore the integration has to be started at the eastern boundary where the

transport is zero then and satisfies the boundary condition (5.5). Integration in westward direction gives the stream function

$$\Psi(x,y) = -\frac{1}{\rho_0 \beta} \int_x^{x_{\text{east}}} \operatorname{curl} \boldsymbol{\tau}(x',y)\, \mathrm{dx}'.$$

According to (5.1) the wind field curl is given by

$$\operatorname{curl} \boldsymbol{\tau} = -\,\partial_y \tau_x = -\frac{\tau_0 \pi}{L_y} \cos\left(y \frac{\pi}{L_y}\right),$$

so the internal stream function can be determined:

$$\Psi(x,y) = \frac{1}{\rho_0 \beta} \frac{\tau_0 \pi}{L_y} \cos\left(y \frac{\pi}{L_y}\right) (x_{\text{east}} - x).$$

Because of the special choice of the wind field (5.1), this solution satisfies boundary conditions (5.5) on all boundaries except for the western border. Additionally it satisfies the free slip conditions at Northern and southern boundaries. The meridional transport arising from the given wind field is

$$V = \partial_x \Psi = -\frac{1}{\rho_0 \beta} \frac{\tau_0 \pi}{L_y} \cos\left(y \frac{\pi}{L_y}\right).$$

It is southward everywhere and takes its maximum value in the centre of the domain.

The Sverdrup balance is especially remarkable since the transports predicted by it are independent of the stratification in the flat bottom case. In the real ocean the bottom is not flat, consequently (5.4) contains an additional term taking into account the topography (JEBAR term, compare section 5.4). Additionally nonlinear terms omitted by us may become important and result in further differences between Sverdrup transport and real ocean transports. For discussion and comparison to observations see, for example, Schmitz et al. (1992), Pedlosky (1996).

The western boundary current

In order to close the streamlines on the west coast and to satisfy the remaining boundary conditions the viscosity term has to be restored:

$$\beta_0\, \partial_x \Psi = \frac{1}{\rho_0} \operatorname{curl} \boldsymbol{\tau} + A_h \nabla^4 \Psi.$$

Since the Sverdrup solution satisfies the boundary conditions in the North and the South, no boundary layers are expected at these boundaries. Considering eastern and western boundary layers, the approximation

$$\nabla^4 \Psi \approx \partial_{xxxx} \Psi$$

is valid, which follows from the assumption that the accommodation of the Sverdrup interior to the boundary conditions takes place in a thin layer of width D_{M} defined below whereas the changes in y-direction are on the scale of the basin width:

$$\frac{\Psi}{L_y^4} \ll \frac{\Psi}{D_{\mathrm{M}}^4}, \tag{5.8}$$

where D_{M} denotes the Munk layer width. This layer is expected to be much smaller than the basin width and later results will proof the validity of this assumption. For the given x-independent wind stress we can assume the solution in the form

$$\Psi(x,y) = \psi(x)\mathrm{curl}\,\boldsymbol{\tau}(y).$$

Substituting this ansatz into the differential equation gives an ordinary differential equation for $\psi(x)$. The solution is

$$\Psi(x,y) = \frac{\mathrm{curl}\,\boldsymbol{\tau}}{\rho_0\beta_0}(x-x_{\mathrm{E}})\left\{1 - \frac{2}{\sqrt{3}}\exp\left(\frac{x-x_{\mathrm{W}}}{2D_{\mathrm{M}}}\right)\cos\left(\frac{\sqrt{3}(x-x_{\mathrm{W}})}{2D_{\mathrm{M}}} - \frac{\pi}{6}\right) - \right.$$
$$\left. - \exp\left(\frac{x-x_{\mathrm{E}}}{D_{\mathrm{M}}}\right)\right\}, \tag{5.9}$$

where $D_{\mathrm{M}} = \sqrt[3]{A_H/\beta_0}$ denotes the boundary layer width. For $A_h = 2000$ m^2/s the Munk layer turns out to be 46 km wide which is very small compared to the basin width of 2000 km, thus the assumption (5.8) is justified. The three terms in the curly brackets of (5.9) correspond to the interior solution equal to the Sverdrup result, the correction at the western boundary and the correction at the eastern boundary.

5.3.2 Vertical structure

Now we return to the full equations for u, v, w in order to get some insight into the vertical structure and the Ekman pumping mentioned above. Again we start from the assumption that geostrophy holds in the interior far from the surface and all other boundaries, i.e. the velocity field there is given by

$$\boldsymbol{f} \times \boldsymbol{u}_g = -g\nabla\zeta.$$

Since ζ is a function of x and y only, it is immediately clear that the geostrophic part of the circulation is independent of depth.

Additionally it is assumed, that the geostrophic velocity field respects continuity:

$$\mathrm{div}\,\boldsymbol{v}_g = \nabla\cdot\boldsymbol{u}_g + \partial_z w_g = 0.$$

The surface boundary layer

The first boundary layer under consideration is the surface Ekman layer. As in the approximation (5.8) it is allowed to approximate the viscosity term far from lateral walls

$$\operatorname{div} \boldsymbol{A}\, \mathbf{grad}\, \boldsymbol{u} \approx A_v\, \partial^2_{zz} \boldsymbol{u},$$

where it is additionally assumed that A_v is constant. Thus the horizontal equations of motion are given by

$$\boldsymbol{f} \times \boldsymbol{u} - A_v\, \partial^2_{zz} \boldsymbol{u} = \boldsymbol{f} \times \boldsymbol{u}_g.$$

With boundary conditions (5.2) and $\boldsymbol{u} \to \boldsymbol{u}_g$ for $z \to -\infty$ the result is given by

$$u = u_g + \frac{\exp(z/D_{\mathrm{Ek}})}{\sqrt{A_v f}} \left\{ \frac{\tau_x}{\rho_0} \sin\left(\frac{z}{D_{\mathrm{Ek}}} + \frac{\pi}{4}\right) + \frac{\tau_y}{\rho_0} \cos\left(\frac{z}{D_{\mathrm{Ek}}} + \frac{\pi}{4}\right) \right\}, \quad (5.10)$$

$$v = v_g + \frac{\exp(z/D_{\mathrm{Ek}})}{\sqrt{A_v f}} \left\{ -\frac{\tau_x}{\rho_0} \cos\left(\frac{z}{D_{\mathrm{Ek}}} + \frac{\pi}{4}\right) + \frac{\tau_y}{\rho_0} \sin\left(\frac{z}{D_{\mathrm{Ek}}} + \frac{\pi}{4}\right) \right\}, \quad (5.11)$$

where $D_{\mathrm{Ek}} = \sqrt{2A_v/f}$ is the Ekman layer depth. This solution was first obtained by Ekman (1905) and has the shape of a spiral. On northern hemisphere the velocity at the surface shows an angle of 45 degrees to the right of the wind field and spirals down in clockwise direction with the magnitude decaying exponentially with an e-folding scale equal to the Ekman layer depth. For a relatively large vertical viscosity $A_v = 0.1$ m^2/s this layer is about 50 m deep, i.e. in most modelling approaches the Ekman layer is not properly resolved.

In the following we split up the total transport into an Ekman part and a geostrophic part:

$$\boldsymbol{U} = \boldsymbol{U}_{Ek} + \boldsymbol{U}_g.$$

The Ekman transport can be calculated from vertically integrating either the solution above or easier from integrating the equation

$$\boldsymbol{f} \times (\boldsymbol{u} - \boldsymbol{u}_g) = A_v\, \partial^2_{zz} \boldsymbol{u}$$

vertically from the bottom of the Ekman layer to the surface. If wind stress is assumed at the surface and free slip at the lower bound, the Ekman transport is given by

$$\boldsymbol{U}_{Ek} = \int_{-D_{\mathrm{Ek}}}^{0} (\boldsymbol{u} - \boldsymbol{u}_g)\, \mathrm{dz} = \frac{1}{f\rho_0} \begin{pmatrix} \tau_y \\ -\tau_x \end{pmatrix}. \quad (5.12)$$

This transport is directed to the right relative to the wind direction with an angle of 90 degrees.

Ekman pumping

The divergence of the just calculated Ekman transport leads to a vertical velocity at the bottom of the Ekman layer. Since continuity is assumed to hold for the geostrophic part the same holds for the Ekman part and Ekman pumping can be derived from

$$\partial_z w_{\mathrm{Ek}} = \partial_z (w - w_g) = -\nabla \cdot (\boldsymbol{u} - \boldsymbol{u}_g).$$

We assume $w = 0$ at the surface, and the same condition for both geostrophic and Ekman part of the vertical velocity, $w_g = w_{\mathrm{Ek}} = 0$ in $z = 0$. The profile of the Ekman pumping is readily obtained by integration of the Ekman spiral (5.10)-(5.10). It is exponentially reaching the limit $\nabla \cdot \boldsymbol{U}_{Ek}$ (compare the sketch in figure 5.2). Thus indeed, the Ekman pumping at the bottom of the Ekman

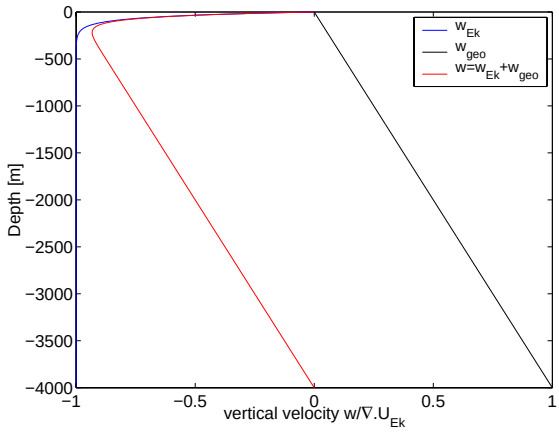

Figure 5.2: Sketch of Ekman pumping and geostrophic part of the vertical velocity. The full vertical velocity is given by the sum of both. The depth of the Ekman layer is 50 m.

layer is given by the divergence of the Ekman transport,

$$w_{\mathrm{Ek}}(-D_{\mathrm{Ek}}) \approx \nabla \cdot \boldsymbol{U}_{Ek}.$$

Cross differentiating the geostrophic equation gives together with continuity the z-derivative of w_g:

$$\partial_z w_g = \frac{\beta_0}{f} v_g. \tag{5.13}$$

This relation implies the coupling between Ekman- and geostrophic part of the flow. The velocity v_g is constant in depth, therefore the right side of (5.13) gives the slope of a straight line. In the flat bottom case $w = w_g + w_{\mathrm{Ek}} = 0$ in $z = -H$, consequently w_g at the bottom is given by the negative Ekman pumping and the value of v_g is fixed. The profile of the geostrophic vertical velocity w_g can be expressed as:

$$w_g(x, y, z) = \nabla \cdot \boldsymbol{U}_{Ek}(x, y) z/H, \tag{5.14}$$

where H denotes the depth of the basin.

Vertically integrating (5.13) gives the meridional geostrophic transport

$$V_g = \frac{f}{\beta_0} w_g(x,y,0) = \frac{f}{\beta_0} \mathrm{curl}\left(\frac{\boldsymbol{\tau}}{\rho_0 f}\right) = \frac{\mathrm{curl}\,\boldsymbol{\tau}}{\beta_0\rho_0} + \frac{\tau_x}{f\rho_0}.$$

Comparison to the Ekman transport (5.12) shows that the sum of meridional geostrophic and Ekman transport gives back the Sverdrup value

$$V_{Sv} = V_{Ek} + V_g.$$

It has to be stressed that only the sum above satisfies the no normal flow condition at the northern and southern boundaries. Thus the vertically resolved flow field with Ekman velocities at the surface and deeper flow given by geostrophy develops boundary layers at these boundaries.

Further boundary layers

The meridional component of the velocity field below the Ekman layer is given by

$$\begin{aligned} v_g = V_g/H &= \frac{\mathrm{curl}\,\boldsymbol{\tau}}{H\beta_0\rho_0} + \frac{\tau_x}{Hf\rho_0} \\ &= \frac{1}{H\rho_0}\left\{-\frac{\tau_0\pi}{\beta_0 L_y}\cos\left(\frac{y\pi}{L_y}\right) + \frac{\tau_0}{f}\sin\left(\frac{y\pi}{L_y}\right)\right\}. \end{aligned} \tag{5.15}$$

Consequently $v_g(x,\pm L_y/2,z) = \pm\tau_0/(H\rho_0 f) \neq 0$, i.e. boundary corrections are needed in the North and the South.

These corrections are obtained in the same way as in case of the Ekman layer above. In case of the northern boundary we are looking for a solution of

$$\boldsymbol{f}\times\boldsymbol{u} + A_h\,\partial^2_{yy}\boldsymbol{u} = \boldsymbol{f}\times\boldsymbol{u}_g$$

with boundary conditions

$$\begin{aligned} \partial_y u = 0 \quad &\text{for } y = L_y/2 \text{ (free slip)}, \\ v = 0 \quad &\text{for } y = L_y/2 \text{ (no normal flow)}, \\ \boldsymbol{u} \to \boldsymbol{u}_g \quad &\text{for } (y - L_y/2) \to -\infty. \end{aligned}$$

The solution turns out to be

$$\begin{aligned} u &= u_g + \exp(\eta)(v_g\cos\eta - v_g\sin\eta), \\ v &= v_g + \exp(\eta)(-v_g\cos\eta - v_g\sin\eta), \end{aligned}$$

where $\eta = (y - L_y/2)/D_{\rm N}$ and $D_{\rm N} = \sqrt{2A_h/f}$ denotes the northern boundary layer width. From the continuity equation an expression for the vertical velocity correction can be obtained:

$$\partial_z w_c \approx -\partial_y (v - v_g) = \text{const.}$$

$$\begin{aligned} w(x,y,z) &= -\partial_y v H(1 + z/H) \\ &= (H+z)\frac{2v_g(x,y)}{D_{\rm N}} \exp\left(\frac{y - L_y/2}{D_{\rm N}}\right) \cos\left(\frac{y - L_y/2}{D_{\rm N}}\right) + w_g. \end{aligned}$$

For A_h=2000 m^2/s the northern boundary layer is about 6 km wide. Model results of the wind-driven circulation in domains with vertical walls should contain oscillations in velocity components close to these vertical borders if the boundary layer is resolved.

5.4 Spin-up of a stratified ocean with topography

If the fluid is vertically stratified the theory of section 5.3 is applicable since the transport Ψ can be introduced in this case. However the stratification gives birth to baroclinic waves discussed in chapter 4 whose propagation speed is much slower than for the barotropic case. Correspondingly the relaxation to the Sverdrup balance takes longer time. If additionally the bottom is not flat, the stream function-vorticity equation contains an additional term describing the "Joint Effect of Baroclinicity and Relief" JEBAR introduced by Sarkisyan and Ivanov (1971). In inviscid case without bottom friction the stationary equation is

$$J(\Psi, f/H) = \underbrace{-H^{-2} J(E,H)}_{\rm JEBAR} + \text{curl}\,(\boldsymbol{\tau}/H), \tag{5.16}$$

where $H(x,y)$ denotes the water depth and E denotes the potential energy

$$E = g \int_{-H}^{0} z\rho \,\mathrm{dz}.$$

Equivalently this relation can be formulated in terms of the bottom pressure torque:

$$\beta\, \partial_x \Psi = J(P,H) + \text{curl}\,(\boldsymbol{\tau}), \tag{5.17}$$

where P denotes the bottom pressure

$$P = p_{\rm atm} + g \int_{-H}^{0} \rho \,\mathrm{dz}.$$

The spin-up of a stratified ocean initially at rest has been discussed in many papers. Anderson and Gill (1975) considered the two layered flat bottom case, whereas Anderson and Killworth (1977) investigated the spin-up of a two layered system with topography. In the following results of the latter paper and the resulting view of the spin-up process are summarised.

Anderson and Killworth (1977) formulate the problem as system of equations for the barotropic velocity $\bar{u}$ and the baroclinic velocity $\hat{u}$. These two equations are coupled, time scale $\hat{T}$ of $\hat{u}$ is connected to the speed of baroclinic Rossby waves thus much larger than the timescale $\bar{T}$ of $\bar{u}$, related to the speed of external Rossby waves.

The resulting equations show that topography is mostly felt by $\bar{u}$, at first by a term in the equation for $\bar{u}$, containing the topography and secondly via the coupling to $\hat{u}$. Initially for time of the order $\bar{T}$ much smaller than $\hat{T}$ the barotropic part $\bar{u}$ reaches the topography modified Sverdrup balance, whereas $\hat{u}$ is very small since it evolves at much larger time scales. Therefore the velocity field is mostly given by the barotropic part and shows a strong signature of the topography.

As time passes, baroclinic Rossby waves travel through the basin, $\hat{u}$ grows and slowly removes the topography influence in the equation for $\bar{u}$ since the coupling term partly cancels the topography term. Eventually both parts evolve and take the shape of the flat-bottom Sverdrup solution, that is they finally coincide, which is only possible if the flow in the lower layer is equal to zero.

The latter point also holds if the bottom is flat, i.e., the presence of stratification puts limitations to the possible circulation since eventually no nonzero vertical velocity is allowed at the interface between two layers. This implies the 'Sverdrup catastrophy': finally all circulation is contained in the upper layer, all other layers are at rest.

In terms of bottom pressure torque this result can be rephrased as follows. In general the initial density stratification together with the prescribed topography gives a nonzero bottom pressure torque. This leads to an accommodation process adopting the density field to the topography. The wind gives rise to an Ekman transport in the surface layer leading to Ekman pumping that deforms the isopycnals at all depths. The disturbance of isopycnals excites baroclinic modes of Rossby waves. These waves propagate westward through the domain and as these waves pass they influence the density field such that the bottom pressure gradient is adjusted parallel to the gradient of topography. This in fact cancels out the bottom pressure torque term in (5.17) and puts this equation into flat bottom form. Consequently the final solution for Ψ coincides with the flat bottom solution.

All this theory does not apply immediately to the experiments run with FEOM_0 since the model contains viscosity and diffusion that is absent in the reasoning above. Nevertheless it turns out that the statements above remain valid to a large extent as is seen in the model results below.

5.5 Results

In the following results from numerical experiments with FEOM_0 are presented. There are four experiments discussed below.

- wind-driven circulation in a homogeneous ocean with flat bottom (WDHF)
- Circulation in a homogeneous ocean with ridge (WDHR)
- Circulation in stratified fluid and flat bottom (WDSF)
- Circulation of stratified fluid in basin with a ridge (WDSR)

The relevant parameters are collected in table 5.1. In all cases model runs in

	WDHF	WDHR	WDSF	WDSR
topography	flat	ridge	flat	ridge
max. depth [m]	1000	4000	4000	4000
stratification	none	none	linear	linear
N [s^{-1}]	0	0	0.0031	0.0031
c_0 [m/s]	36.5	146.2	146.2	146.2
c_1 [m/s]	–	–	0.058	0.058
A_h/A_v [m^2/s]	2000/0.001	2000/0.0001	20000/0.001	20000/0.001
K_h/K_v [m^2/s]	–	–	2000/0.001	2000/0.001
D_{M} [km]	46.6	46.6	100.5	100.5
D_{Ek} [m] (center)	16.5	16.5	16.5	16.5
$D_{\text{N}}/D_{\text{S}}$ [km]	6.5/8.9	6.5/8.9	20.5/28.1	20.5/28.1
Δx range [km]	20-100	20-100	20-100	20-100
Δz range [m]	10-400	10-300	10-300	10-300
levels	7	20	20	20
Int. period	7500 d	229 d	3165 d	3290 d
time step [s]	21600	3600	1800	1800

Table 5.1: Parameters of the experiments concerning the wind driven circulation.

time stepping mode are discussed. In some cases (homogeneous density) also stationary solutions were computed but these were always very close to the final state of time stepped runs.

The integration period is from several to 20 years, integration is always started from the state of rest. The large integration periods are required because final equilibration occurs on a time scale of basin viscous modes.

5.5.1 Experiments without stratification

The aim of this section is to compare the flat-bottom solution for the Munk gyre of $FEOM_0$ to the theory of section 5.3.

LeProvost (1986) considered the Munk problem in grids with different structure and resolutions using a 2D finite element model. A 3D-solution is more difficult to obtain because additional boundary layers appear and the vertical structure has to be reproduced by the model.

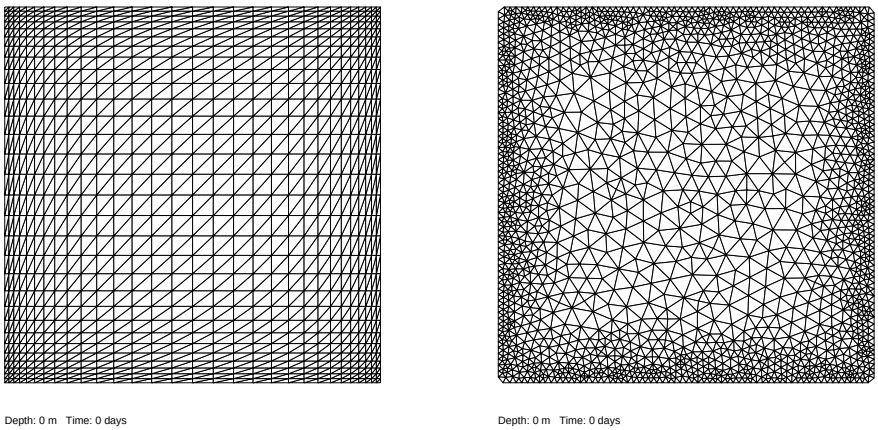

Figure 5.3: Regular and unstructured surface grid used in experiments investigating the wind-driven circulation. Both meshes show high resolution in boundary layers, and have similar numbers of grid points.

The surface triangulations used in later comparisons are shown in figure 5.3. A regular stretched grid and a completely unstructured surface mesh is used. In both grids the resolution close to the boundaries is increased in order to resolve boundary layers. The highest resolution is about 20 km $\hat{=}$ 1/5°. In comparison, the Munk layer width is about 46 km, the northern and southern boundary layers are 6.5 and 8.9 km wide respectively. Therefore the model might be able to represent the Munk layer, the northern and southern boundary layers however cannot be expected to be properly represented. In the interior the resolution is chosen rather coarse ($\sim$100 km $\hat{=}$ 1°).

Transports

The transport stream function of run WDHF diagnosed from the flow velocity field is plotted in figure 5.4, while figure 5.5 presents the difference between the model and theoretical Munk solution (5.9). Transports are given in Sverdrups, where 1 Sv = 10^6 m^3/s. Overall, we conclude that the Munk solution is reproduced reasonably well in both grids – figure 5.4 shows the presence of both the western boundary current and return loop of reasonable amplitude and width.

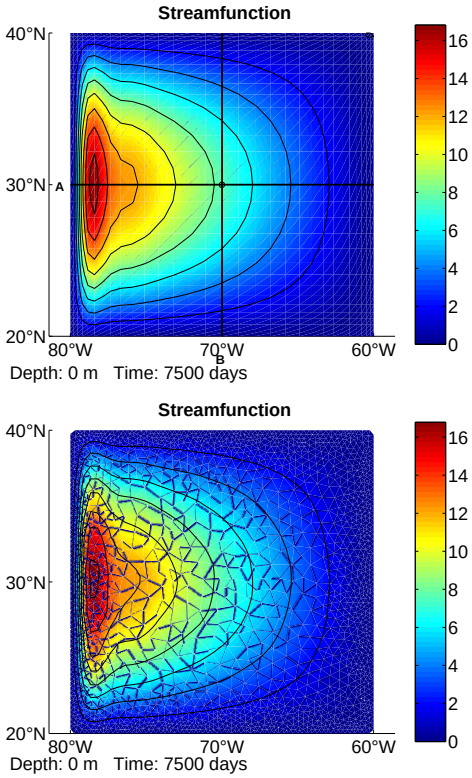

Figure 5.4: Transport stream function (in Sv) obtained after 7500 model days of integration in regular (left panel) and unstructured grid (right panel). The lines in the left panels are sections A and B which will be referenced later.

The southward return flow next to the western boundary current returns a part of the western boundary transport which consequently does not reach the Sverdrup interior. The existence of the return flow depends on the boundary conditions and the type of viscous operator. It is absent if viscosity is replaced by linear bottom drag friction (see Stommel, 1948).

The error between the model and theoretical solution is up to 5% which could partly be explained by the presence of viscosity, but mostly by discretisation errors (as the western boundary layer is still only within several grid intervals). The solutions obtained for structured and unstructured grids are similarly accurate as witnessed by figure 5.4. The error pattern is sensitive to the local grid size and thus looks patchy in the unstructured case.

Figure 5.6 shows the northward transport through the central zonal section A included in figure 5.4. The positions of extrema are accurately reproduced by the model.

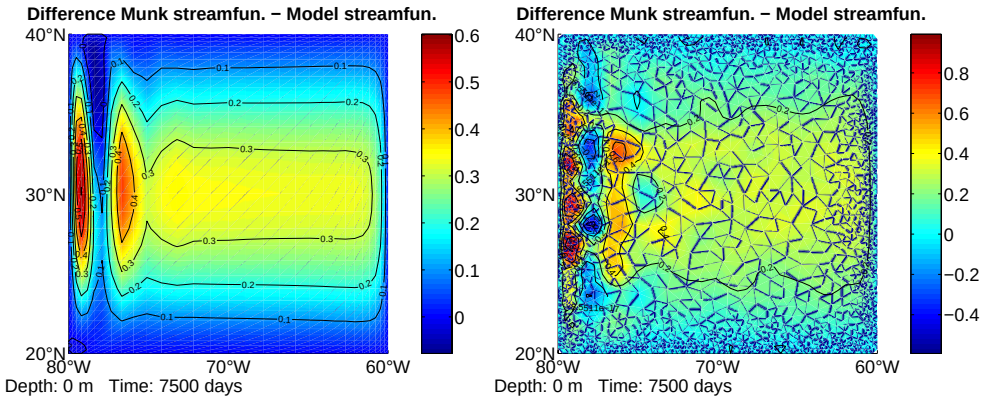

Figure 5.5: Difference Munk stream function - Model stream function (in Sv) in regular grid (left panel) and unstructured grid (right panel).

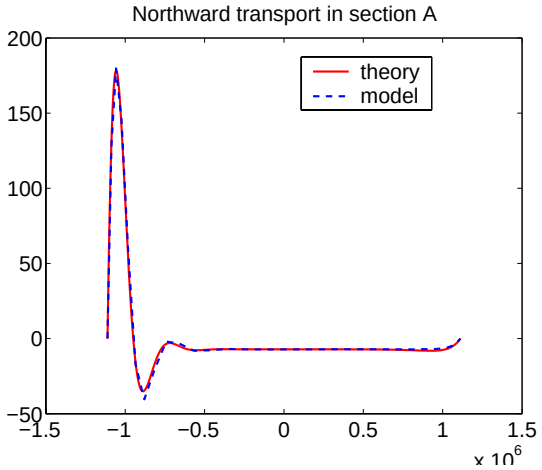

Figure 5.6: Northward transport (in $[m^2/s]$) in central zonal section A depicted in figure 5.4.

The vertical structure

In section 5.3.2 we saw that the vertical flow field far from lateral boundaries is divided into at least two regions: the Ekman layer at the surface and the geostrophic region below. Since the bottom boundary condition is free slip, the bottom boundary layer is weak and influences the solution only slightly.

The left panel of figure 5.7 shows the northward velocity (colour) together with the remaining components in vector form (arrows) for the flat bottom case in section A. The horizontal velocity components below the surface layer are shown to be independent of depth.

In order to get an impression of the model's ability to represent the Ekman transport, the horizontal flow field in the lowest layer is subtracted from from the field in all layers. The vertically integrated result in section B is shown in

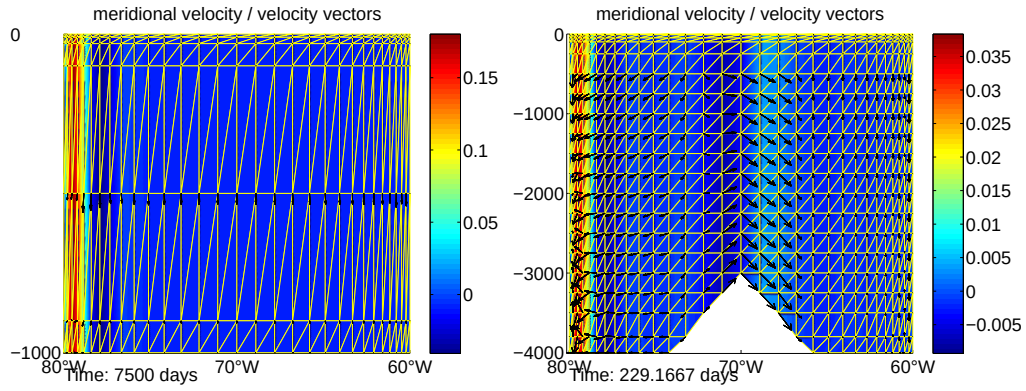

Figure 5.7: Northward velocity (colour, in [m/s]) and vectors of other components in section A (see figure 5.4) for unstratified experiments with flat bottom and a ridge. The vertical axis and vertical velocity component are scaled by the same factor. Note that the depth of the basin in the right panel is four times as deep as in the left panel.

figure 5.8. It is compared to the prediction from equation (5.12) which does not take into account boundary layers. The coincidence is good except close to the northern and southern walls.

Northern boundary layer

It was already pointed out that northern and southern boundary layers are less than 10 km wide and cannot be resolved properly. However the model shows the predicted behaviour to a certain extent as shown in figure 5.9 in 900 m depth. The sinus shaped interior Sverdrup flow (compare equation (5.15)) is represented rather well. The boundary layers have to return the transport arising from the divergence of the Ekman transport in the surface layer.

As the total transport given by the model is correct, the boundary layers are able to return the appropriate volume. Although figure 5.9 shows that the unresolved boundary layer flow cannot be represented correctly the fluid exchange in boundary layers is integrally correct.

The vertical structure of the vertical velocity is subject of figure 5.10. The left panel shows the vertical profile of the upward velocity below the central node marked in figure 5.4 by the crossing of sections A and B. The right panel shows the corresponding figure for the unstructured grid. In this case it was necessary to calculate the mean over the surrounding nodes. This is due to formulating the problem in weak form and absence of a regularising operator in horizontal directions in the equation for w. Consequently the solution can only be expected to be free of computational modes in weak form, i.e., in a mean sense. The Ekman pumping given in equation (5.14) is reproduced very well. There is

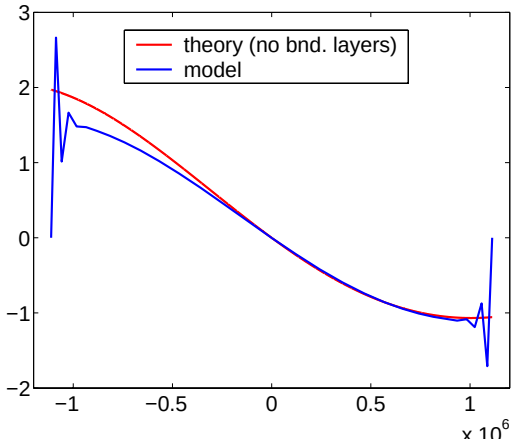

Figure 5.8: meridional Ekman transport (in m^2/s) in section B (see figure 5.4). The theoretical curve does not take into account boundary layers which occur since the transport in equation (5.12) obtained from the wind stress does not satisfy the no normal flow condition.

only one layer of nodes in the surface Ekman layer, nevertheless there is a nice correspondence between theory and model in figures 5.10 and 5.8. Haidvogel and Beckmann (1999) state that one layer of nodes in the Ekman layer is sufficient for reproduction of the Ekman transport in difference models. From the results above it can be concluded that this statement applies also to the Finite Element model. However as seen in figure 5.10 the model Ekman layer extends over at least 2 layers.

Homogeneous flow with topography (experiment WDHR)

The dynamically important part of pressure in homogeneous fluid is given by the surface height alone and the horizontal flow field is independent of depth outside the Ekman layer even if topography is present. In experiment WDHR the wind stress is applied to the model domain with a ridge in meridional direction shown in the right panel of figure 5.7. The topography is independent of y. The density is constant and the same figure shows the depth independent structure of the horizontal velocity components. Also visible is the good representation of the vertical velocity on the sloping bottom region which follows exactly the boundary condition and leads to a flow parallel to the bottom. Here the advantage of the tetrahedral discretisation takes effect.

Since the bottom is not flat, the vertical velocity does not vanish at the bottom and Sverdrup's theory cannot be applied. However it can be shown that free geostrophic flow of homogeneous fluid is parallel to f/H contours (see e.g. Mellor, 1996). In the presence of wind forcing and viscosity, a balance holds between the Jacobian $J(\Psi, f/H)$ on one side and the wind curl plus viscosity on

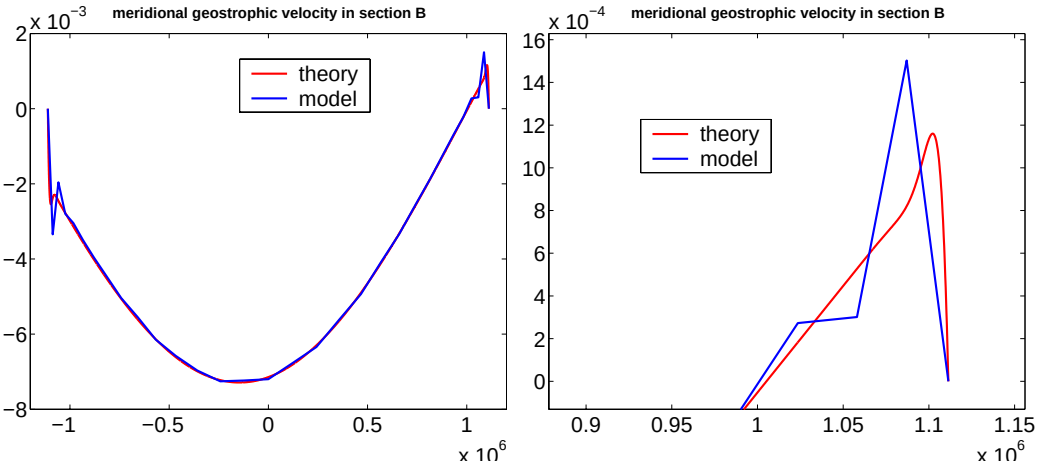

Figure 5.9: Meridional geostrophic velocity component (in [m/s]) in section B (see figure 5.4) at a depth of 900 m. The right panel shows a zoom of the boundary layer region close to the northern wall.

the other side. Figure 5.11 shows the transport stream function in the basin with ridge together with the contours of f/H. The transport is slightly smaller than in the flat-bottom case.

5.5.2 Spin-up of stratified fluid with topography

Experiments WDSF and WDSR are concerned with the problem of ocean spin-up due to wind stress suddenly applied to the surface of a stratified ocean. Analogous numerical experiments were considered in Olbers and Eden (2003) in a comparison of the models MOM and BARBI.

The basin is either a flat bottom one (WDSF) basin or furnished with the ridge as shown in the right panel of figure 5.7 (WDSR). The stratified case requires a finer vertical resolution than the homogeneous one and therefore experiment WDSF was run with 20 layers compared to 7 layers in WDHF.

Section 5.4 summarised some findings of theoretical and numerical approaches to this problem, and the spin-up process passes through the following stages:

- Initially the flow field is dominated by the barotropic part which shows a strong imprint of the topography
- while time passes baroclinic Rossby waves travel through the basin and influence the pressure field such that bottom pressure gradients become oriented parallel to the gradient of topography.
- Finally the influence of topography is removed in the solution – it resembles the flat bottom situation.

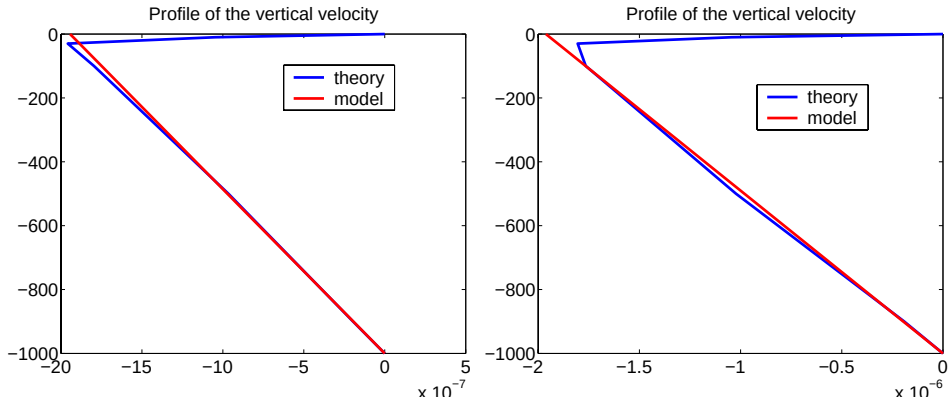

Figure 5.10: Profile of vertical velocity (in [m/s]) below the central surface node (intersection of sections A and B in figure 5.4). Right panel shows the result obtained with regular grid, in the left panel the mean value over nodes neighbouring the central node is calculated. These results coincide well with the predicted linear behaviour beneath the surface boundary layer.

First we compare the initial stages in WDSF and WDSR. Figure 5.12 shows the stream functions after 2.5 days. The solution with topography (right panel) shows a strong imprint of the ridge. In both cases the transports are still rather small.

Also the vertical flow field after 5 days through the central zonal section (figure 5.13) shows the predicted structure. It is barotropic in nature and of comparable magnitude. After several years however the situation changes drastically. As seen in figure 5.14 the stream function of both experiments becomes rather similar and resembles the shape of the homogeneous Munk solution (see figure 5.4). Also the magnitude and structure of the transport across the central zonal section (figure 5.15) compares well to the Munk solution. In the flat-bottom case the maximum is apparently too low, a reason for that behaviour might be attributed to differences in the shape and setup of boundary layers. The vertical structure follows the theoretical predictions of section 5.4. The circulation is finally concentrated in the upper half of the basin (figure 5.16).

Figures 5.17-5.24 show the evolution of sea surface height, bottom pressure and transports in upper and lower half of the basin for the different experiments.

Independent of the presence of topography the initial contours of sea surface height and bottom pressure show similar shape. Consequently the circulation patterns close to the surface and in deep layers are similar (figure 5.17), in case of experiment WDSR with some influence of the ridge (figure 5.19). As time passes baroclinic Rossby modes alter the shape of isopycnals and finally the deep pressure field is completely decoupled from the sea surface height (figure 5.18). In the presence of topography bottom pressure isolines become oriented along isobaths as can be seen especially in the right half of the lower panel in figure

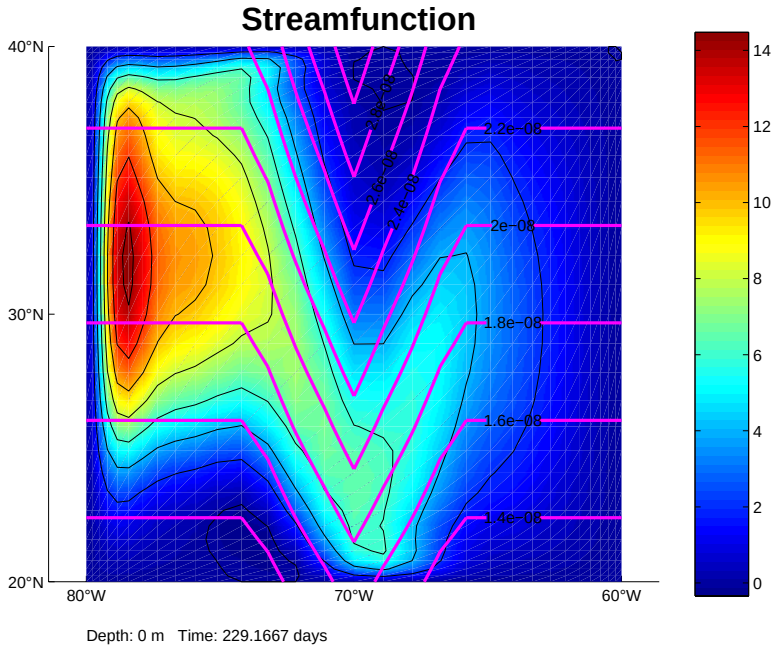

Figure 5.11: Transport stream function (in Sv) in experiment WDHR together with contours of constant f/H. The streamlines differ strongly from those of the flat bottom case shown in figure 5.4 and are oriented along the f/H-contours.

5.20.

The transport in lower and upper half of the basin shows similar stages during spin-up. Initially flow field integrated over the lower 2000 m shows a magnitude comparable to the integral over the upper 2000 m (figures 5.21 and 5.23). After 9 years of integration however the flow in the lower half becomes negligible compared to the upper transport (figures 5.22 and 5.24). In experiment WDSR additionally the influence of topography is clearly present initially, no traces of the ridge are visible in upper as well as lower half in later stages of the experiment.

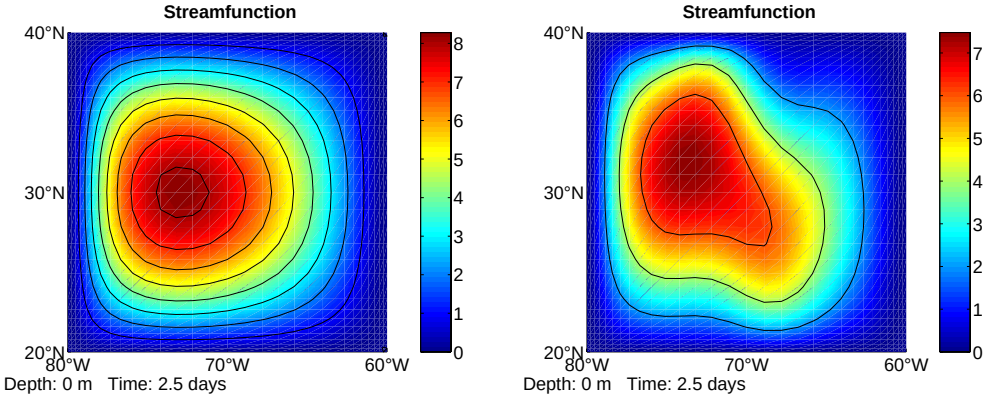

Figure 5.12: Comparison of initial transport stream functions (in Sv) of experiments WDSF (left panel) and WDSR (right panel). The latter shows a strong influence of topography.

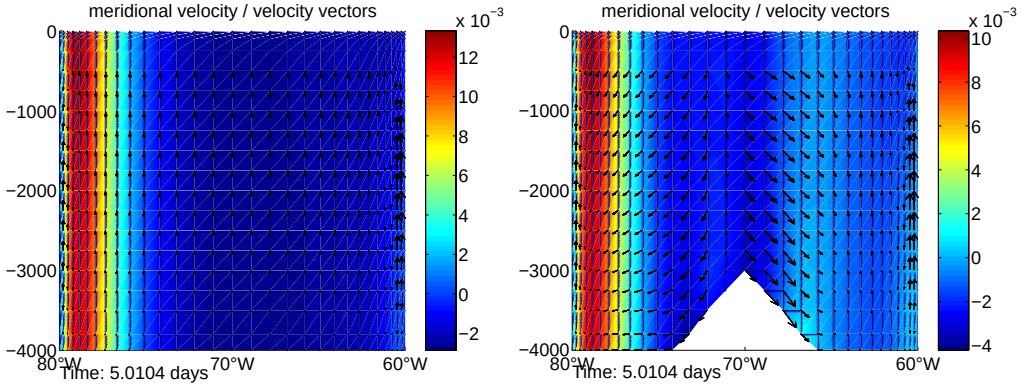

Figure 5.13: Velocity field (in m/s) in the central zonal section showing the barotropic nature of the initial flow field. Once again the vertical axis as well as the vertical velocity component are scaled.

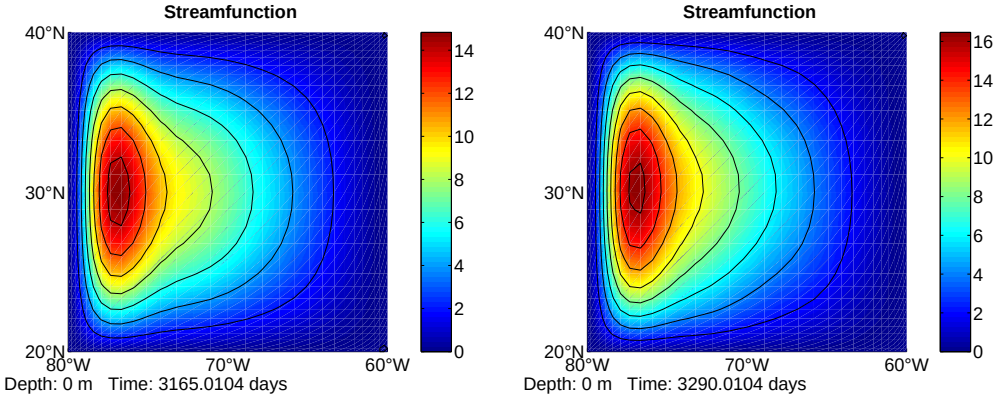

Figure 5.14: As in figure 5.12 but after several years of integration. The shape of the flat bottom solution (left panel) is quite similar to the solution with topography (right panel).

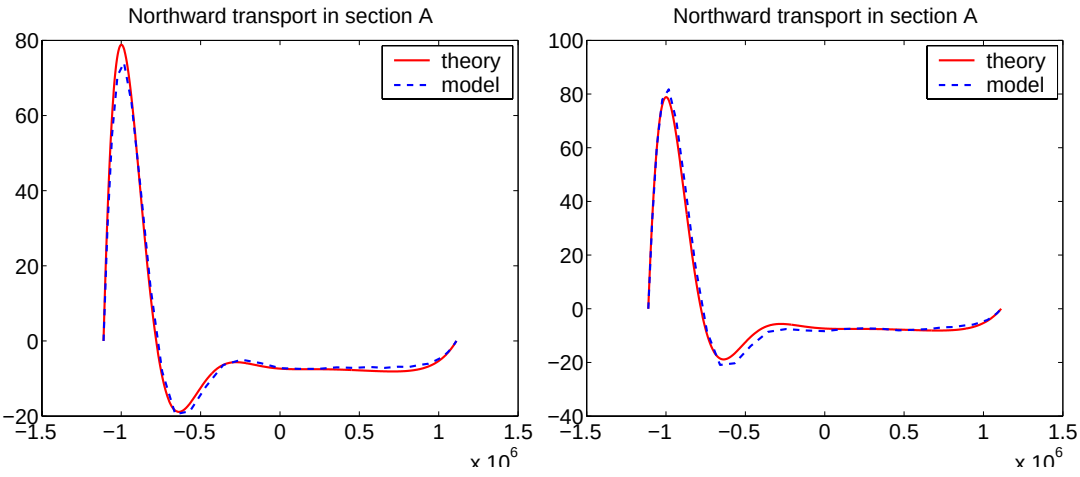

Figure 5.15: Final northward transport across the central zonal section in experiments WDSF (left panel) and WDSR (right panel) in comparison to the Munk solution (compare also figure 5.6)

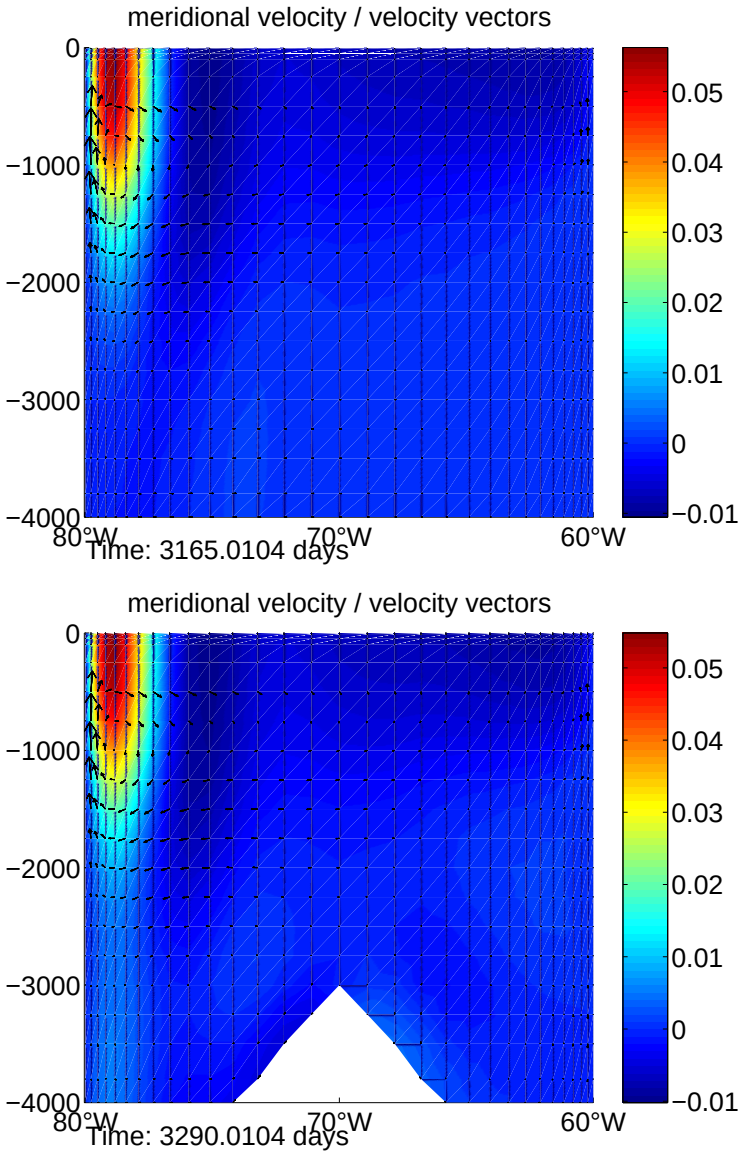

Figure 5.16: As in figure 5.13 after 9 years of integration. The circulation is concentrated in the upper half of the basin in WDSF (left panel) as well as in WDSR (right panel).

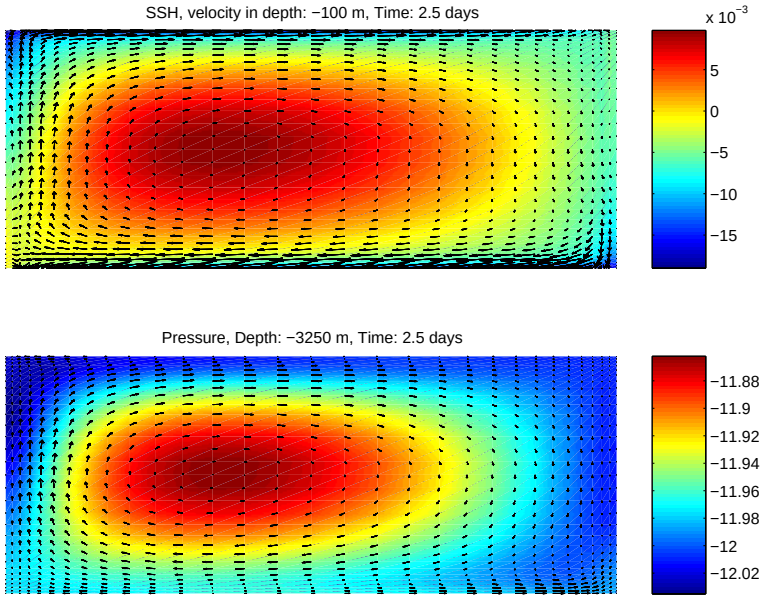

Figure 5.17: Sea surface elevation and velocity field in 100 m depth (upper panel) in experiment WDSF after 2.5 days of integration. The lower panel displays pressure and velocity field in 3250 m depth. At this stage the pressure and SSH show similar contours. Consequently also the flow fields are similar, a significant difference is present only in the lower right corner where upper and deep flow are in opposite directions.

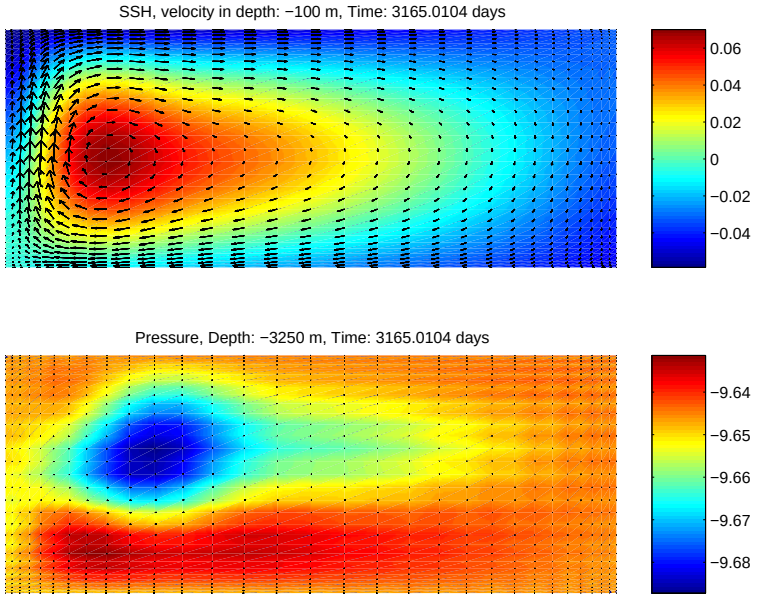

Figure 5.18: As in figure 5.17 but after about 9 years of integration. After this time the deep pressure field is completely decoupled of the SSH. Also the magnitude of the velocity is just a small fraction of the upper values.

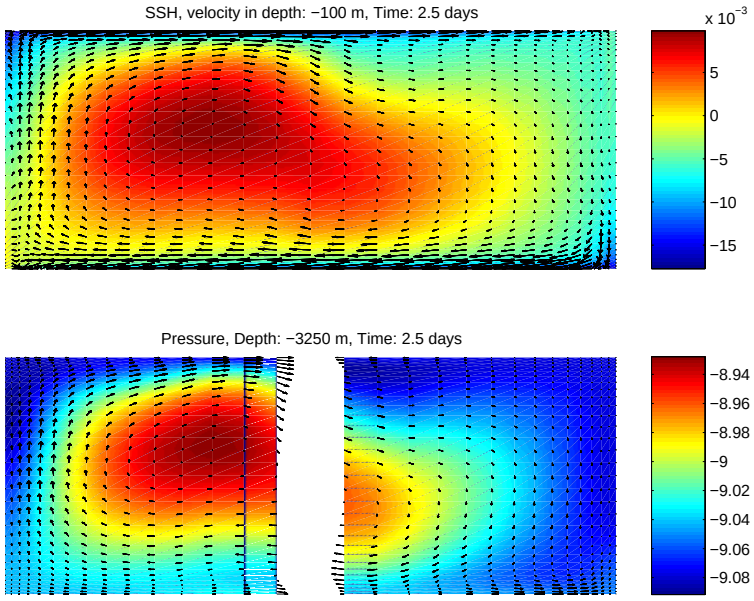

Figure 5.19: As in figure 5.17 but for experiment WDSR with topography. Also in this case SSH and deep pressure field show initially very similar contours despite the presence of topography. The flow field shows the same difference in the lower right corner as in the flat bottom case.

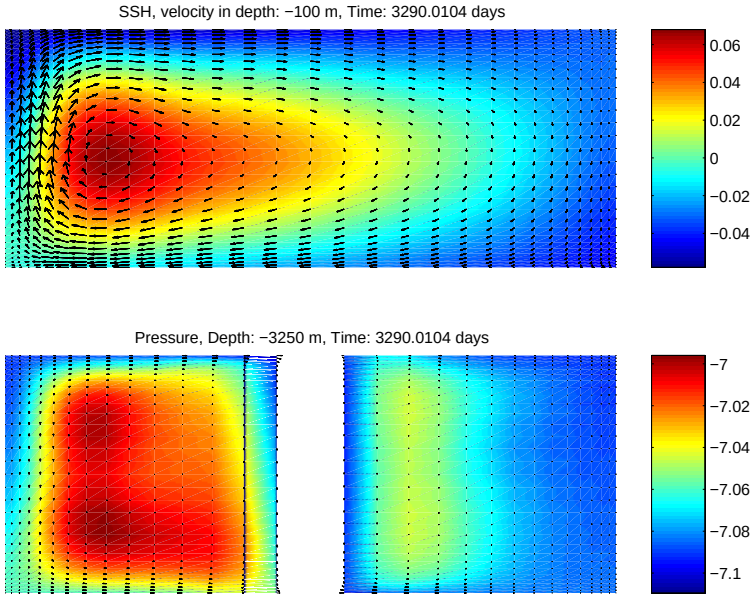

Figure 5.20: As in figure 5.19 but after about 9 years of integration. Now the deep pressure field is completely decoupled from the surface pressure. Especially on the right side of the ridge the pressure contours are oriented along the contours of topography.

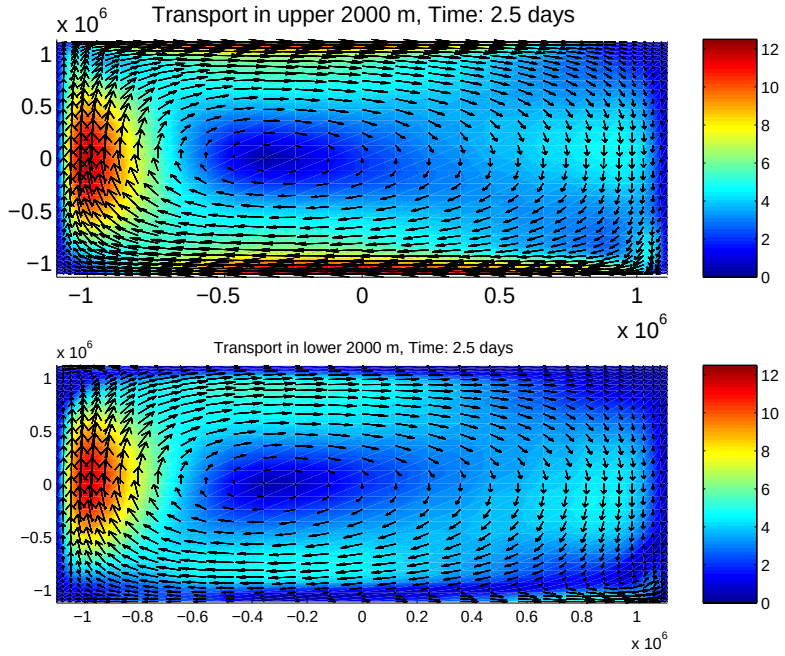

Figure 5.21: Transport (in m^2/s) of upper 2000 m (upper panel) and lower 2000 m (lower panel) in experiment WDSF after 2 days. Colours show the magnitude, arrows point into the direction of the transport. Both panels show comparable transports

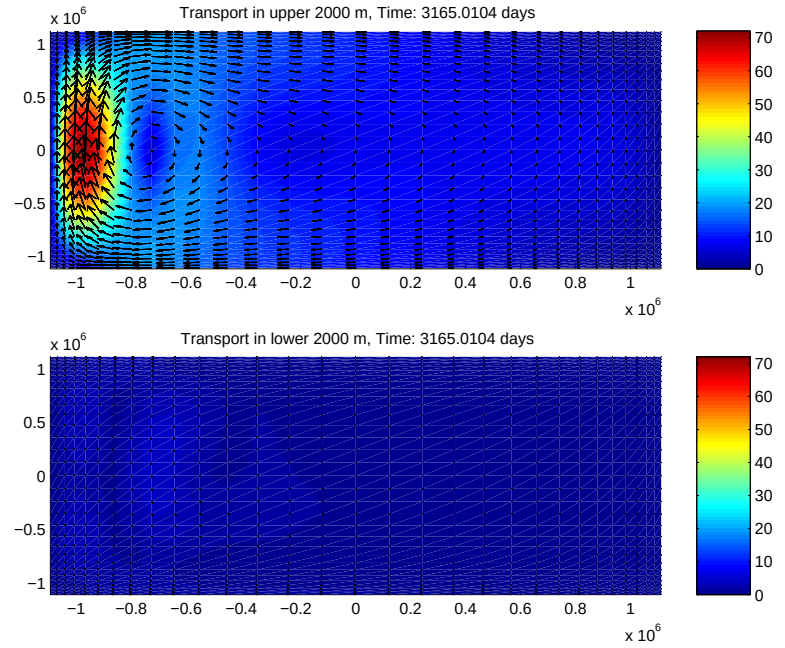

Figure 5.22: As in figure 5.21 but after about 9 years of integration. The transport of the lower half is negligible compared to the upper part.

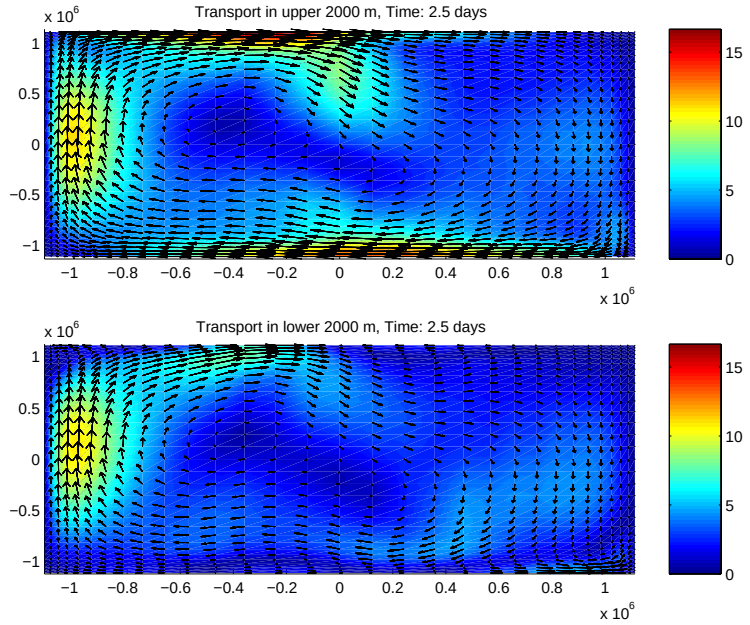

Figure 5.23: Transport (in m^2/s) of upper 2000 m (upper panel) and lower 2000 m (lower panel) in experiment WDRF after 2 days. Colours show the magnitude, arrows point into the direction of the transport. Both panels show comparable transports. A signature of the ridge is clearly visible in the flow field.

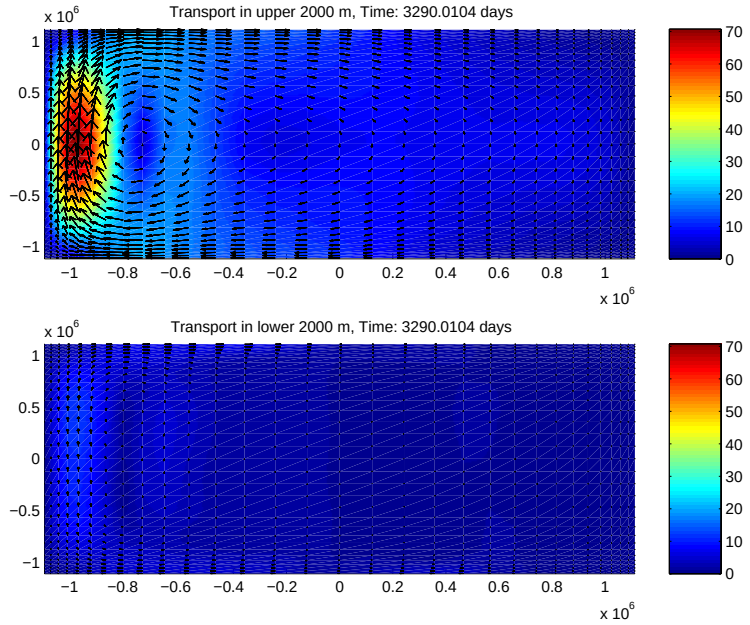

Figure 5.24: As in figure 5.23 but after about 9 years of integration. The transport of the lower is negligible compared to the upper part. Traces of the presence of the ridge are not visible in both panels.

Chapter 6

Idealised Overflow Experiment

6.1 Introduction

The thermohaline circulation is a fluid motion driven by density differences due to variations in temperature and salinity. This mechanism leads to a worldwide ocean circulation known as the conveyor belt circulation which transports huge amounts of heat and mass.

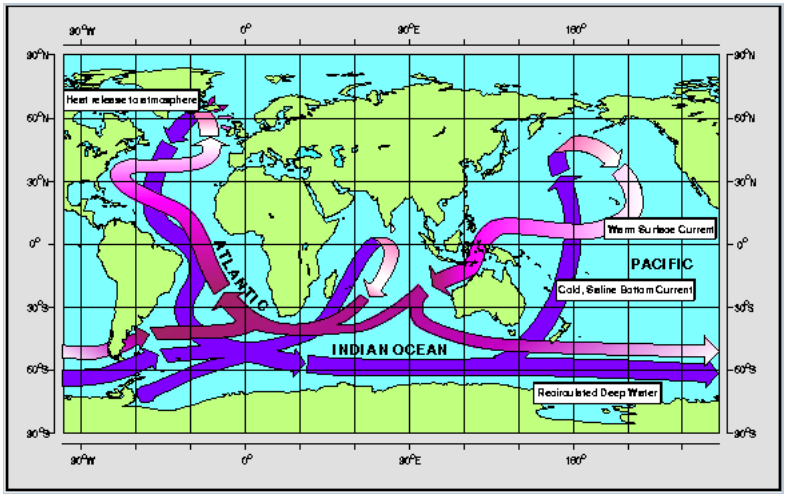

Figure 6.1: Schematic diagram of the 'Global Conveyor Belt' (after W. Broecker modified by E. Maier-Reimer)

One of the major questions in ocean modelling is the reason for the long term stability of the global water mass distribution. This problem can be traced back to small scale processes which describe the production of water masses in their source regions and determine the way cold and dense water reaches the deep ocean. Here flow in narrow straits and canyons and even more overflow over a ridge and the subsequent fate of the dense plume along the continental shelf break is of dominant importance.

In the North Atlantic basin, for example, several highly localised regions are responsible for the deep water path of the thermohaline circulation. The dense water formed in the Nordic Seas by loss of heat to the atmosphere and ice formation passes several straits (Denmark Strait, Iceland-Scotland ridge) into the North Atlantic, where it becomes a part of the deep western boundary current heading southward below the Gulf Stream. The overflow of warm but saline water from the Mediterranean Sea through the Strait of Gibraltar produces the Mediterranean salinity tongue and sets the temperature-salinity structure of a large region of the North Atlantic at mid depths. Relaxation to climatological values of salinity is required in the Gulf of Cadiz by many models, as they are not able to properly simulate the Mediterranean overflow which in particular influences the ability of models to reproduce the Azores Current.

The overflow problem is difficult for modelling as the topography and coastal lines of narrow straits make high resolution necessary. Another difficulty is the simultaneous description of the gradual sinking of the water with only a slow increase in thickness of the plume. It can be partly solved with bottom following sigma coordinates which, on the other hand, lead to too large entrainment and dilution. Geopotential coordinates (with stepwise representation of the bottom) have a problem of getting the flow along the topography and several receipts of parameterising and implementing bottom boundary layers have been proposed (Beckmann and Döscher (1997); Killworth and Edwards (1999)).

Finite elements provide flexible choice of resolution and therefore are well suited for resolving an overflow sub domain without changing the resolution of the ocean interior. Additionally they suggest freedom in combining z- and terrain following vertical levels and allow for a realistic representation of topography even in z coordinate (analogously to cut cells). FEOM_0 relies on the tetrahedral discretisation and possesses all these properties. However, its skill in representing overflows has not yet been tested. We present a series of specially arranged experiments.

This task is facilitated by the DOME (Dynamics of Overflow Mixing and Entrainment) project conceived by Robert Hallberg, James Stephens, and Peter Killworth. It suggests a suite of test problems from simple to more complex circumstances designed to detect strengths and weaknesses of numerical ocean models and lead to their improvement with respect to this important problem. DOME working notes are available at the home page
http://www.rsmas.miami.edu/personal/tamay/DOME/dome.html, whereas details on the idealised specifications are given in Hallberg et al. (2001).

The DOME project consists of three phases. Phase I considers a fully idealised scenario, whereas Phases II and III are concerned with more realistic simulations and the impact of overflow processes in global models. The idealised setup is meant to provide a unique framework in which a comparison of different models is most meaningful since the physical and geometrical situation is very well defined. In the following we consider this idealised (Phase I) setup and present

results obtained with $FEOM_0$ that allow comparison to other models as well as to laboratory experiments.

Our goal is to investigate the performance of $FEOM_0$ with respect to the resulting path of the plume, the obtained overflow transport in magnitude and variability as well as mixing and entrainment properties. Even in the simplest setup of DOME Phase I the overflow problem depends on too many parameters to be addressed in a single study. Here we will be limited to the following questions:

- What is the performance of the hydraulic control theory in predicting the transport and the pattern of the density field across the embayment?

- What is the sensitivity of the dense water pathways and transport variability to the bottom friction and stratification of the ambient water?

The outline of this chapter is as follows: section 6.2 contains information about the general setup of the experiment, the choice and implementation of boundary conditions. In section 6.3 some details on the parameters of $FEOM_0$ are given and section 6.4 discusses the results obtained in different experiments.

6.2 Experimental setup

The process considered in the following is intense mixing of a dense water plume on a slope of given constant inclination. The model domain is depicted in figures 6.2 and 6.3. Into the lower part of the northernmost boundary of the embayment region a given transport of dense water is injected. This plume of water reaches the slope and descends under the influence of Coriolis force and gravity. The interior is either homogeneous or linearly stratified in temperature. The equation of state is linear and depends only on temperature with a constant thermal expansion coefficient set to 0.2 kg/(m^3°C). On the slope, mixing and entrainment changes the properties of the plume. In case of a stratified interior the plume reaches the depth of neutral buoyancy and does not descend any further.

The topics of interest discussed later are the path of the plume, the dependence upon stratification, the role of bottom boundary conditions and mixing/entrainment observed in the simulations.

The most important parameters of this experiment specify the geometrical setup, the density structure in embayment and interior and the numerical resolution. The geometrical setting is depicted in figure 6.2 and the parameters are listed in table 6.1. Some are prescribed by the DOME specifications while others are free. The last column shows the values chosen in the experiments described below. The density difference in the embayment is set to 2 kg/m^3. The corresponding reduced gravity g_o determines the value of the Rossby radius $L = \sqrt{g_o h}/f \approx 24.5$ km that is resolved by the grid.

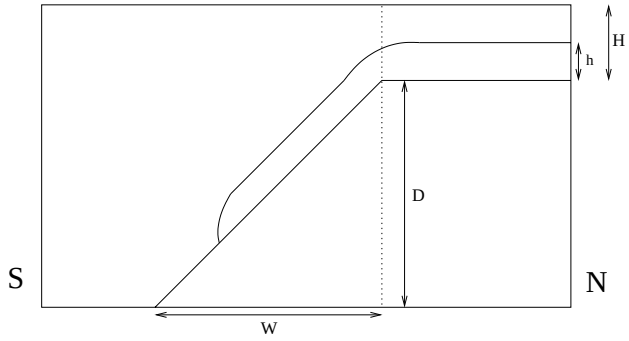

Figure 6.2: Meridional section across the model domain including the most important geometrical quantities

param.	description	DOME spec.	experiments
W	Width of slope	free	300 km
D	Depth of slope	3000 m	
α	$\alpha = D/W$	free	0.01
H	Depth of embayment	600 m	
h	height of inflowing dense water	300 m	
f	Coriolis parameter (f-plane)	10^{-4} s^{-1}	
g_o	reduced gravity in overflow region	free	0.02 m/s^2
g_i	reduced gravity in the interior	free	0 or 0.02 m/s^2
Δx_{min}	highest horizontal resolution	free	20 km
Δz_{min}	highest vertical resolution	free	50 m

Table 6.1: Definition of parameters. Some of them are prescribed by the DOME specifications, others are free to choose.

6.2.1 Inflow boundary condition

The northern boundary of the sill is open. There is no consistent way to formulate boundary conditions there that would ensure directly a given inflow rate. The reason is that a prescribed velocity and temperature (density) distribution at the inflow open boundary could be dynamically inconsistent and would over- or under define the problem. On recognising this fact we allow for a sufficiently long sill so that any inconsistency between the dynamics and boundary is mediated due to finite viscosity and diffusivity in the model. We require that the inflow velocity and temperature distribution are geostrophically balanced and that the inflow satisfies the mass balance constraint. The geostrophically balanced inflow conditions are illustrated in figure 6.4. The dense water density is given by ρ_2, the density distribution of the lighter water ρ_1 is not prescribed in the outflow area. The position of the inflow upper boundary $\eta(x)$ is held fixed, and constant velocity v_{in} is taken such that the transport of the dense water equals some quantity Q_{in} that is sufficiently high. Initially $\rho_1(x, z)$ =const, and the geostrophic balance

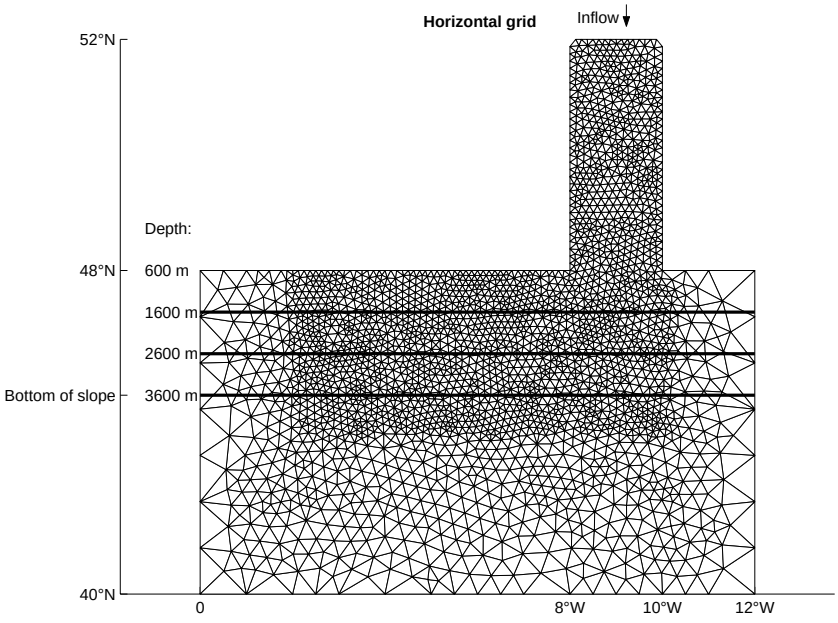

Figure 6.3: Horizontal extent of the model domain with isolines of depth and the horizontal grid

requires that the slope of interface $\partial_x \eta$ and the slope of sea surface elevation $\partial_x \zeta$ are constant:

$$\partial_x \zeta = -\frac{f\rho_0}{g\rho_1} v_{\text{in}} > 0, \quad \partial_x \eta = \frac{2f}{g_o} v_{\text{in}} < 0.$$

Here ρ_0 denotes the global mean density and $g_o = g(\rho_2 - \rho_1)/\rho_0$ is the reduced gravity in the sill. The slopes $\partial_x \zeta$ and $\partial_x \eta$ are positive and negative respectively, since v_{in} is negative.

In order to accelerate the fluid initially, the velocity and density field in the embayment are initialised in the same way as shown in figure 6.4. Such flow does not satisfy the dynamic equations on the downstream end of the sill and thus undergoes a stage of accommodation after integration has begun. It is accompanied by cross-isopycnal mixing. As a result, the dense and light water become partially mixed already in the embayment, and the shape of isopycnals deflects strongly from the initial one. The dense water that has entered into the sill is partially returned back through outflow and the dense water transport Q leaving the sill at its downstream edge is always less than Q_{in}.

In the model, the initial sharp inclined boundary between dense and light fluids is implemented by tilting the mesh.

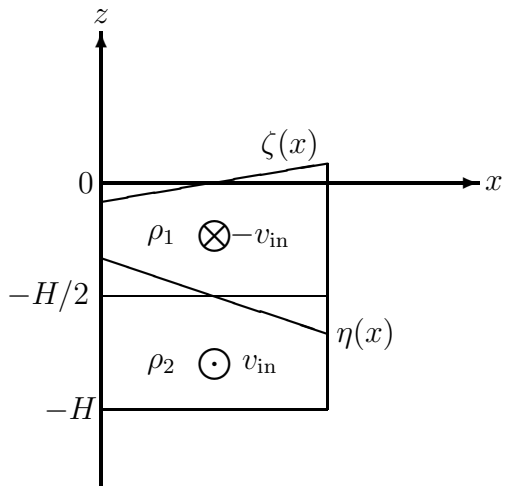

Figure 6.4: Geostrophically balanced inflow conditions with outflow above the inflow. This profile is initially applied to the whole embayment. The area of in- and outflow are equal. In the lower part velocity and density ρ_2 are prescribed, whereas in the outflow part only velocity is prescribed.

6.3 Model setup

6.3.1 The model domain and resolution

The horizontal grid is shown in figure 6.3. Highest resolution is placed in the embayment and along the path of the plume. The vertical grid at the eastern boundary (where the horizontal resolution is rather low) is shown in figure 6.5. There are 12 levels in total, the 6 levels containing the plume initially are following the topography exactly with a constant thickness of 50 m, whereas the vertical resolution in the remaining levels follow the slope like in a sigma grid.

6.3.2 Further model details

In the presented model runs no stabilisation techniques were applied, therefore restrictions on time step and diffusion/viscosity coefficients apply. The advection of momentum is omitted. Parameters and properties are given in table 6.2.

6.3.3 Numerical experiments

Three basic runs using the parameter values given in table 6.1 were aimed at investigating overflow rate, variability and plume path in dependence upon the

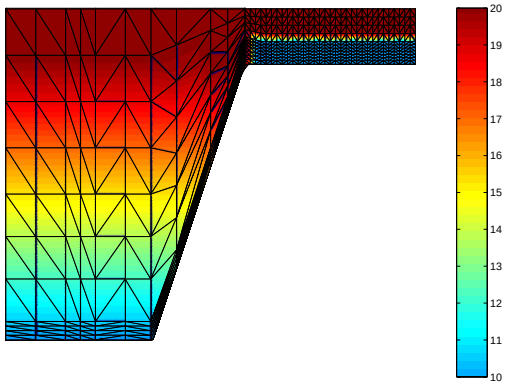

Figure 6.5: Side view of the model grid and initial temperature distribution (in °C) in experiments with stratified interior. In this case the largest density in the interior coincides with the overflow density.

Hor. visc./diff. Vert. visc./diff.	5000/500 m^2/s 0.0001/0.0001 m^2/s
Time step	30 min
integration period	32 days
momentum adv.	switched off

Table 6.2: Model parameters and properties

bottom boundary condition and the presence of stratification. These runs are:

- Run 1: No stratification, no slip, g_o=0.02 m/s^2, g_i=0
- Run 2: No stratification, quadratic bottom stress, g_o=0.02 m/s^2, g_i=0
- Run 3: Stratified interior, no slip, g_o=g_i=0.02 m/s^2

The quadratic stress in Run 2 is imposed as $\vec{\tau}_b = c\,\rho\,|\vec{v}|\vec{v}$ where c=0.003. All runs are integrated for more than 32 days and below we present the results obtained over days 17-32 when the essential part of the plume evolution happens. For visualisation the plume is marked with a passive tracer entering at the inflow boundary with concentration 1. The maximal temperature of the ambient water is 20°C . We arbitrarily identify the boundary of the plume with the 18°C isotherm. The reduced gravity of the plume used for estimates below is defined as

$$g_p = \frac{1}{D_p \rho_0} \int_{z_b}^{z_t} (\rho - \rho_{min})\,\mathrm{d}z \tag{6.1}$$

where D_p denotes the height of the plume (corresponds to the reference isotherm), ρ_0 is the mean density, z_b and z_t denote bottom and top vertical coordinate of

the plume, and ρ and ρ_{min} denote density of the fluid and the minimum density respectively.

Additionally to these basic runs we investigated the dependence of the overflow rate on the reduced gravity g_o and the Coriolis parameter f in the set of experiments with the following parameters:

Experiment Q_{g_o}	$f = 10^{-4}$ s^{-1}	$g_o = 0.01$, 0.015, 0.02, 0.025, 0.03 m/s^2
Experiment Q_f	$g_o = 0.02$ m/s^2	f = 2.5e-5, 5e-5, 1e-4, 2e-4, 3e-4 s^{-1}

In these experiments the mean transport over days 16-32 was determined.

Finally we conducted a dam break experiment to check the consistency of the prescribed inflow with the transport resulting in an experiment with closed walls and a certain reservoir of dense water in the embayment released initially.

6.4 Results

After the first time steps with accommodation processes in the embayment the plume reaches the edge of the slope and a state of constant transport of dense water is obtained.

6.4.1 Overflow transport

Magnitude and structure

DOME Phase I is connected to the problem of dense water flow in between two basins connected by a channel the width of which is large compared to the Rossby radius. This problem is considered in several theoretical and experimental studies starting in the 1970s with papers by Whitehead, Gill and others. According to Whitehead et al. (1974), in an inviscid two layer system with vanishing cross channel velocity component the overflow rate $Q(h, g_o, f)$ scales like

$$Q = c\frac{g_o\, h^2}{f} \tag{6.2}$$

In other words, it is hydraulically controlled and determined by the geometry of the sill. Since the assumptions of vanishing cross channel velocity and zero viscosity are not fulfilled in our setup a strict validity of (6.2) cannot be expected. However we calculated the mean transport for different values of g_o and f and found that the dependence (6.2) of the sill transport on these parameters holds to a large extent as can be seen in figure 6.6. The constant c in equation (6.2) was determined by a least squares fit. We find 0.31 for variable g_o and 0.33 for variable f.

Whitehead et al. (1974) also determined the shape of the interface of a stationary solution and found that when the interface is detached from the eastern

wall, it is parabola shaped and intersects the bottom at a distance proportional to the Rossby radius. In our case due to finite diffusivity, the boundary between dense and light water in the embayment cannot be exactly defined. Figure 6.7 shows a set of isopycnals characterising the transition zone. The isopycnals detached from the wall in the right panel of figure 6.7 resemble a parabola with a flat tangential at the western wall, whereas the isolines which are still connected to the eastern boundary combine the the parabolic western part with an exponential tail stretching to the eastern wall.

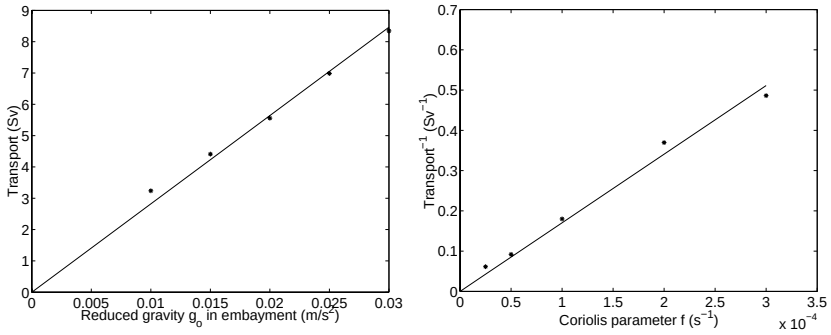

Figure 6.6: Mean transport (day 16-32) in experiments with varied values of g_o (left) and varied Coriolis parameter. The straight lines present the least squares fit to experimental data and correspond to c≈0.31 and 0.33 in the left and right panels respectively.

Thus we can conclude that the sill is sufficiently long for memory on the inflow condition to decay and the flow is dynamically balanced.

Two further observations are characteristic for a hydraulic control of the overflow. First the Froude number takes values of about 1 in the overflow region. The Froude number is defined as $Fr = \Delta v / \sqrt{g_p \, D_p}$ where Δv denotes the difference between mean plume velocity and mean ambient velocity and the other quantities are given in (6.1). Secondly, prescribing a higher inflow does not change the overflow rate considerably. For example an inflow transport increased by a factor of three changed the overflow transport only by 9.5%. Instead a return flow in the embayment with outflow of dense water develops.

Variability

In observations and numerical simulations of Denmark Strait overflow (Käse et al. (2003), Krauss and Käse (1998)) as well as in laboratory experiments related to the overflow problem the overflow transport is found to be strongly varying in time. Frequently a train of eddies is observed above the descending plume. Lane-Serff and Baines (1998) discuss possible mechanisms contributing to the formation of barotropic eddies. An important aspect is the "capturing" of ambient fluid by the plume, leading to vortex tube stretching on the way down the slope finally

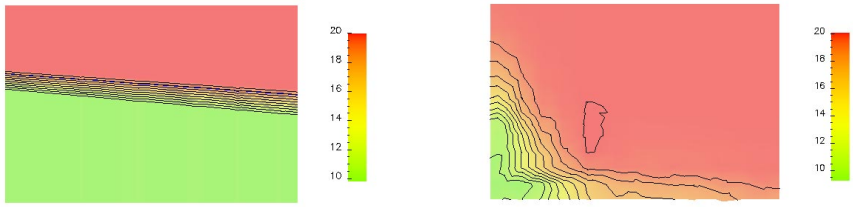

Figure 6.7: Temperature section across the embayment close to the sill initially and after 32 days (in °C).

forming eddies. Simultaneously the plume is decomposed into patches of dense water. They define the quantity $\Gamma = L\alpha/H$, where L denotes the Rossby radius and H is the total embayment depth and identify a range of this parameter where eddies exist.

Also in our experiments with homogeneous interior variability of the plume transport is observed. It could be traced back to the instability of the downslope edge of the plume which ends up in the plume decomposition into patches. The extent of this variability however depends on the bottom boundary condition. Figure 6.8 shows the vertically integrated marker in a snapshot after 26 days for homogeneous interior in runs 1 and 2 with different boundary conditions. In the first case in the left panel the plume breaks into patches whereas in the second case the plume height is modulated. This variability is also highlighted in the time series of the sill transport shown in figure 6.9. The time series shows variability of several days in both cases however the magnitude the fluctuations differs considerably for quadratic bottom stress and the extreme case of no slip.

Figure 6.10 displays the sea surface elevation (contour lines projected to the surface plane) in run 2 showing a train of eddies. Figures 6.10 and 6.11 show that these eddies correspond to patches of dense water. Figure 6.11 also presents the northward velocity component projected to a vertical section along the plume. Here the barotropic nature of the eddies becomes apparent. The eddies are predominantly cyclonic in most of the water column, whereas the circulation in the dense water patches is rather anticyclonic. This is broadly consistent with laboratory experiments (Lane-Serff and Baines, 1998), observations and other model results (Käse et al. (2003), Jungclaus et al. (2001)).

In experiments with stratified interior the vertical displacement is more constrained due to the presence of stratification, the parameter Γ defined above must be replaced by a quantity taking into account the interior reduced gravity g_i (see Lane-Serff and Baines (2000)). In our run 3 no variability is observed (figure 6.9), yet it could be present for other combinations of stratification, overflow transport

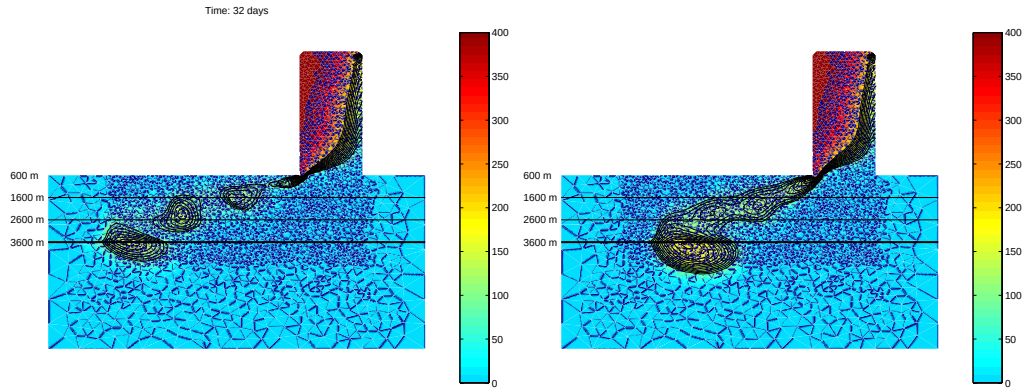

Figure 6.8: Comparison of the vertically integrated plume marker (corresponds to the total plume thickness) for quadratic stress (left figure) and no slip condition. In the latter case the angle of decent is slightly steeper.

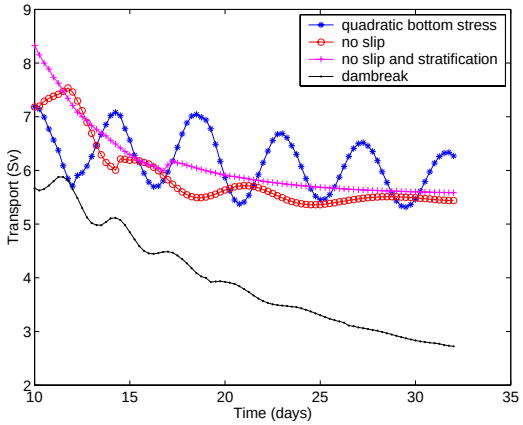

Figure 6.9: Time series of sill transport below the 18°C -isotherm from day 10 to 32 for different numerical experiments.

and friction as follows from (Jungclaus et al., 2001) and (Lane-Serff and Baines, 2000).

The transport time series of the dam break experiment is shown in figure 6.9. The resulting transport coincides initially quite well with the mean value achieved with inflow conditions. At later stages however the transport is reduced because the reservoir runs empty.

6.4.2 Path of the plume

Homogeneous interior

In the absence of stratification the plume turns to the right and descends at a constant angle. Again this angle depends on the bottom boundary condition. For

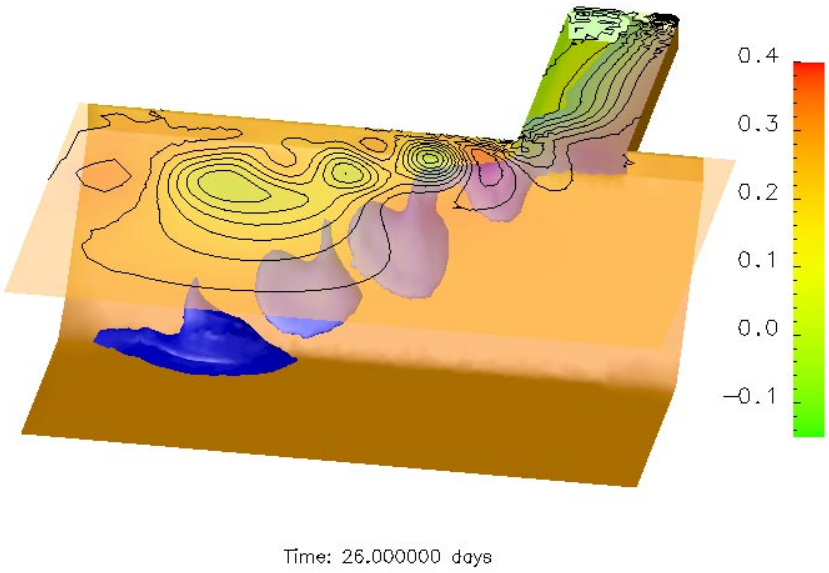

Figure 6.10: Three dimensional view of the 18°C -isosurface together with isolines of the sea surface elevation (given in m)

no slip conditions the descent is steeper than for quadratic stress (compare figure 6.8). This is reasonable, since the path results from a balance between Coriolis force, gravity and friction and for growing friction the path should deviate more and more from the frictionless solution along the slope at constant depth. This shows that a proper representation of the bottom boundary layer is necessary to correctly predict the path of the plume.

The propagation of eddies and plume is visualised in the Hovmöller diagram for the curl of the surface velocity in a section along the plume (figure 6.12). Lane-Serff and Baines (2000) state that the along slope velocity should scale with the Nof velocity $c_N = g_p \alpha / f$, where g_p is the reduced gravity of the plume and α the slope. It is the along slope velocity of an inviscid eddy of dense water on a slope, following from the balance between gravity and Coriolis force (see Nof (1983)). Included in figure 6.12 is the graphically determined velocity of eddy propagation. Experiments with two different values of f, showed that the inverse proportionality is well reproduced.

Stratified interior

In the presence of stratification the plume undergoes mixing on its way down the slope and finally reaches the depth of neutral density. Further descent is

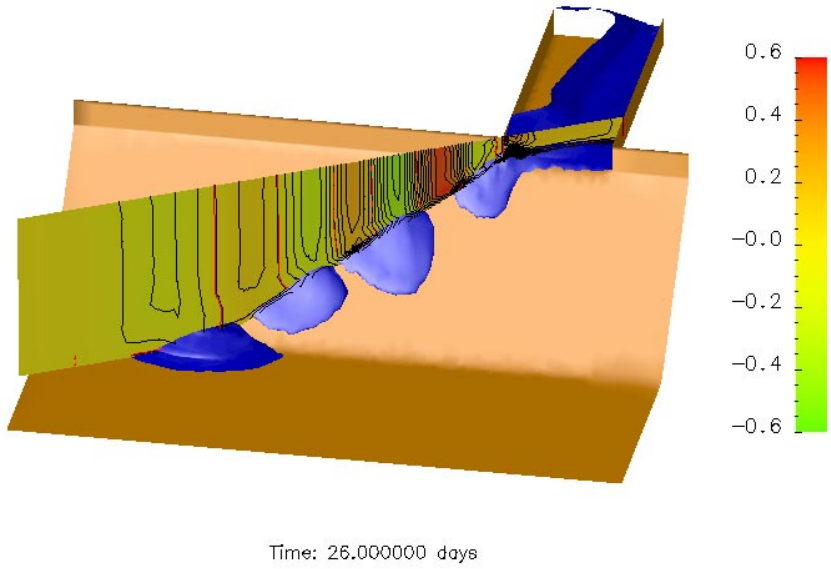

Figure 6.11: Temperature isosurface together with northward velocity component (in m/s) projected to a vertical section along the plume

prohibited and it spreads along the slope at constant depth. An isosurface of the plume marker (concentration=0.1) is shown in figure 6.13 after the level of neutral buoyancy is reached. After that the plume moves along the slope at constant depth. Since the density difference in the embayment and the density difference between surface and bottom of the interior water coincide, a descent without mixing would result in the plume reaching the bottom. Thus diffusion and divergence of sigma levels give rise to a higher extent of diapycnal mixing. However the amount of mixing can be reduced by tilting the diffusion tensor (see also section 6.4.3). Also replacement of the linear equation of state by the UNESCO formula will help in reaching a more realistic representation of the plume properties. However, the DOME Phase I setup requires a linear equation of state.

An interesting feature considering this along slope movement is shown in the Hovmöller diagram in figure 6.14. Although the sill transport remains constant (see figure 6.9) and the distance to the western boundary is still rather large, the plume slows down and rather turns into the interior of the model domain. A comparison with figure 6.12 shows that the plume in the homogeneous case slows down only after it reaches the bottom. The responsible process if stratification is present might be the propagation Kelvin waves along the boundaries bending up isopycnals and leading to a basin wide circulation in the interior which interacts

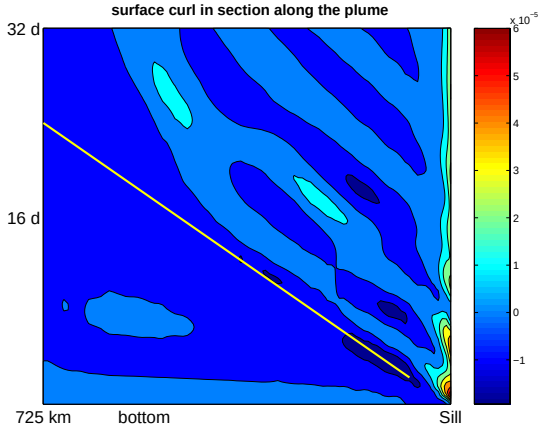

Figure 6.12: Eddy propagation in a Hovmöller diagram showing the curl (in s^{-1}) of the surface velocity in the section shown in figure 6.11 along the plume. The line shows the graphically determined velocity ($\approx$ 35 cm/s).

with the plume.

6.4.3 Mixing and entrainment

As Käse et al. (2003) point out, the process that we call entrainment is almost completely due to horizontal and vertical diffusion but nevertheless it is informative to have a look at the transport of the plume as it moves down the slope. The total integrated transport relative to different temperature isosurfaces is shown in figure 6.15. After the plume reaches the slope, water of low temperature is mixed away rather fast. The mixing might be reduced by tilting the diffusivity tensor so that mixing occurs mostly along isopycnals. This will be implemented in future versions of FEOM. On the other hand in the transport relative to the 18°C isosurface is enhanced by entrainment. These results agree qualitatively with transports of different density classes obtained in model studies of Denmark Strait Overflow by Käse et al. (2003). It is possible to define an entrainment coefficient from the slope of these curves and the model results with realistic topography just mentioned show an area of strongest entrainment. Such a region cannot be identified in figure 6.15, the mean entrainment relative to the highest temperature isosurface is rather smooth, which we attribute to the simplified geometry.

6.5 Conclusion

The Finite Element Ocean Model was applied to the idealised overflow setup suggested in the DOME inter comparison project. The experiments result in a reasonable path of the dense water allowing us to conclude that FEOM_0 performed

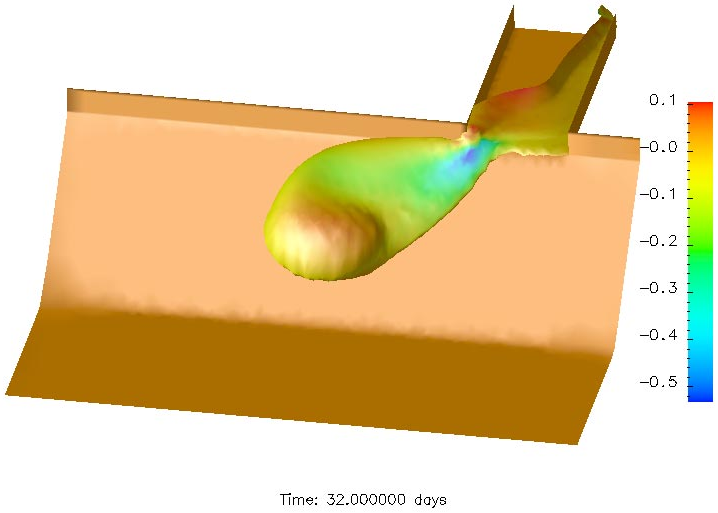

Figure 6.13: 0.1-Isosurface of marker in a snapshot. Projected to the surface is the along slope velocity component (in m/s)

well in this idealised case. In a series of runs with varied Coriolis parameter and reduced gravity, we found that the overflow transport satisfies the scaling suggested by results of the hydraulic control theory, which agrees with expectations of the DOME setup. A variability of several days was found in runs with homogeneous interior, in this case the plume is decomposed into patches of dense water corresponding to nearly barotropic eddies. The magnitude of variability depends on the bottom friction and ambient stratification and was strongly reduced in experiments with stratified interior (which damps such barotropic motions). We cannot exclude some sensitivity of the observed variability and entrainment to the excessive horizontal diffusivity and absence of rotation of the diffusivity tensor following the slope of isopycnals in the model setup used by us.

Clearly, the mesh used for simulations does not exploit the possibilities of FE as the geometry is intentionally simple. It is therefore of interest to proceed to Phase 2 and 3 of the DOME and investigate FEOM performance on a global mesh in a configuration with realistic coastal line and topography of the Denmark Strait. This is the topic for further research.

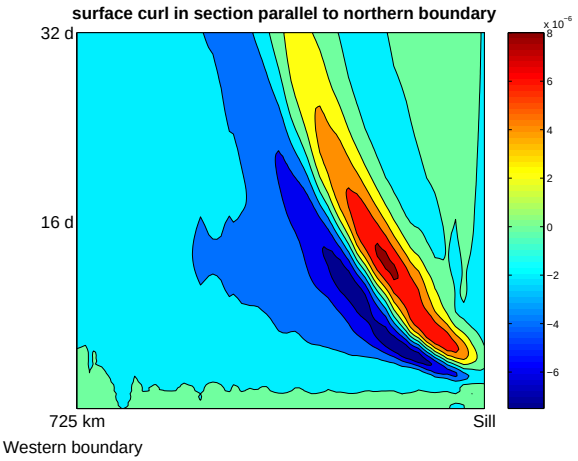

Figure 6.14: The same as in figure 6.12 but for the experiment with stratification in a section parallel to the northern boundary of the basin

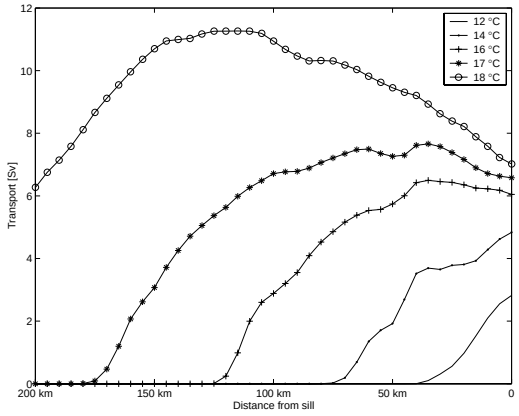

Figure 6.15: Transport integrated with respect to different temperature isosurfaces

Chapter 7

Summary and Conclusions

For convenience of the reader the following sections summarise the major results from the performed experiments in the model evaluation before the thesis closes with conclusions.

Wave propagation

The model ability to reproduce the propagation of baroclinic Rossby waves was tested by simulating the propagation of a temperature anomaly ranging from top to bottom in a stratified environment.

- The central part of the anomaly around mid-depth moves at the speed of the first baroclinic mode and the model reproduces the theoretically predicted propagation speed c_1 very accurately.

- Top and bottom parts of the anomaly travel with lower speeds of higher modes and the model's result coincides quite well with the theoretical value of c_2.

- The overall picture of ssh and velocity follows closely the results of MOM and BARBI given in Olbers and Eden (2003), including generation and propagation of the Kelvin wave in the initial phase, and subsequent propagation of Rossby waves.

Wind-driven circulation

The circulation driven by the prescribed wind stress in homogeneous and stratified basin with and without topography was simulated with FEOM_0 and compared to analytical and available numerical results. The focus of the comparison was not only on the horizontal transports, but also on the vertical structure of the resulting flow.

- The total transport given by Munk theory is reproduced by $FEOM_0$ accurately on both structured and unstructured grids in homogeneous and stratified environments.
- All vertical walls show boundary layers that grossly correspond to theoretical predictions. Although the northern and southern boundary layers are not properly resolved on the grids used they integrally return the predicted transport.
- Few layers of nodes within the Ekman layer are found to be sufficient to reproduce the integral Ekman transport. This result is in agreement with Haidvogel and Beckmann (1999).
- The spin up of stratified fluid in a basin with topography as simulated by $FEOM_0$ follows closely to the theoretical predictions and reproduces the main phases of the process.
  - Initially, on a time scale that is small compared to the time needed by baroclinic waves to traverse the basin the flow field shows a strong imprint of the bottom topography.
  - At intermediate time, the flow in the lower part of the basin becomes weaker whereas the topographic signature in the flow in the upper part of the basin gradually disappears.
  - Finally the stream function is very similar to the flat bottom case.
- The wind-driven circulation of $FEOM_0$ coincides well with that of MOM and BARBI given in Olbers and Eden (2003).

Idealised overflow experiment

An idealised overflow scenario corresponding to the specifications of the DOME intercomparison study was simulated with $FEOM_0$. According to this scenario, dense water descends along a slope of given inclination in a basin of prescribed geometry. Because of the flexibility of local refinement in $FEOM_0$, overflow regions might be a promising field of its applications. The most important results found for the DOME setup are:

- The overflow rate follows the laws of hydraulic control.
- In case of a homogeneous interior variability of several days shows up in the magnitude of the overflow rate.
- The path of dense water is affected by Coriolis force and forms an angle which depends on the bottom boundary condition. With increasing bottom friction increases also the angle between plume and the horizontal direction.

This agrees with theory: for zero friction the plume should follow the isobaths.

- In case of interior stratification the plume reaches the level of neutral buoyancy and moves further at constant depth.

Conclusions

Motivated by the complexity of ocean coastlines and bottom topography the goals of the thesis were the development and validation of the ocean circulation model based on finite element discretisation and capable of simulating the large-scale ocean circulation on temporal scales from years to decades. The main result of the thesis is the basic version of the Finite Element Ocean circulation Model ($FEOM_0$) developed by the author and, and the proof of its ability to simulate processes of geophysical relevance on unstructured grids.

The development of $FEOM_0$ showed that despite the considerable computational burden posed by the need of solving huge systems of linear equations, there are preconditioners and iterative solvers available that allow treatment of such problems. The maximum size of the problem dealt with in the thesis is 62640 3D nodes which is mostly explained by the need to treat a big number of test cases at different values of governing parameters. Using stabilisation techniques and separating the barotropic subproblem (as in the current version of FEOM used for studies of the North Atlantic circulation) strongly facilitates the solution and allows the treatment of problems with the number of nodes limited only by the available memory.

Another practical conclusion is the understanding that the computational effort on unstructured grids is not only determined by the need to solve large systems of linear equations, but also by the necessity of doing loops over all neighbouring nodes for each node when computing right hand sides of the governing equations. For this reason, $FEOM_0$ is always slower than models running on structured grids with the same number of nodes. The potential of $FEOM_0$ is in simulating cases where the variable resolution is really needed and exploited and in this case it could compare well with models based on structured grids.

Testing the model in a set of process studies exemplifying three important topics in the framework of geophysical fluid dynamics — baroclinic wave propagation, wind driven circulation and gravity currents (overflows) — has shown that $FEOM_0$ possesses a skill required by them, and that the use of unstructured grids generally results in similar accuracy of simulations and does not bias the solution (see summary of simulation results in the preceding sections). In particular, a common argument against unstructured grids is the would-be problem of wave scattering at abrupt changes of the nodal density. The experiments

concerned with propagation of baroclinic Rossby waves (initialised with a temperature anomaly) through a basin , discretized with a grid whose resolution changes abruptly along the path of the waves show that the problems arising therefrom are minor if the waves are well resolved in both parts of the grid.

Finite element models have been successfully applied before in oceanography to essentially 2D tidal and coastal problems. The results presented in this work indicate that three-dimensional large-scale ocean circulation is also a promising field for modelling with unstructured grids. An interesting direction for future work, which also coincides with phase II of the DOME project, could be the study of the Denmark Strait Overflow where the ability of FEOM_0 to resolve the coastlines and bottom topography could be exploited much more extensively than in the test cases considered above.

Bibliography

Adcroft, A., Hill, C., Marshall, J., 1997. Representation of topography by shaved cells in a height coordinate ocean model. Monthly Weather Review 125 (9), 2293–2315.

Anderson, D. L. T., Gill, A. E., 1975. Spin-up of a stratified ocean, with applications to upwelling. Deep-Sea Research 22, 583–596.

Anderson, D. L. T., Killworth, P. D., 1977. Spin-up of a stratified ocean with topography. Deep-Sea Research 24, 709–732.

Andrich, P., 1988. A multitasked ocean general circulation model. Reference Manual. LODYC, Paris.

Arakawa, A., 1966. Computational design for long-term numerical integration of the equations of fluid motion: Two-dimensional incompressible flow. part I. J. Comput. Phys. 1, 119–143.

Barnard, S., Barnier, B., Beckmann, A., Böning, C. W., Coullibaly, M., DeCuevas, D., Dengg, J., Dieterich, C., Ernst, U., Herrmann, P., Jia, Y., Killworth, P. D., Kröger, J., Lee, M.-M., LeProvost, C., Molines, J.-M., New, A. L., Oschlies, A., Reynaud, T., West, L. J., Willebrand, J., May 1997. DYNAMO Final Scientific Report.

Beckmann, A., Döscher, R., 1997. A method for improved representation of dense water spreading over topography in geopotential-coordinate models. J. Phys. Oceanogr. 27, 581–591.

Bleck, R., 2002. An oceanic general circulation model framed in hybrid isopycnic-cartesian coordinates. Ocean Modelling 4 (1), 55–88.

Bleck, R., Rooth, C., Hu, D., Smith, L. T., 1992. Ventilation patterns and mode water formation in a wind- and thermodynamically driven isopycnic coordinate model of the North Atlantic. J. Phys. Oceanogr. 22, 1486–1505.

Blumberg, A. F., Mellor, G. L., 1987. A description of a three-dimensional coastal ocean circulation model. In: Mooers, C. N. K. (Ed.), Three-dimensional Coastal Ocean Models. Vol. 4 of Coastal and Estuarine Sciences. pp. 1–16.

Bryan, K., 1969. A numerical method for the study of the circulation of the world ocean. J. Comp. Pys 4, 347–376.

Budgell, W. P., Oliveira, A., Skogen, M. D., 2003. Ocean modelling with unstructured triangular grids: Advection schemes. Ocean ModellingSubmitted.

Cushman-Roisin, B., 1994. Introduction to Geophysical Fluid Dynamics. Prentice-Hall Inc.

Danilov, S., Kivman, G., Schröter, J., 2004. A finite element ocean model: principles and evaluation. Ocean Modelling 6 (2), 125–150.

Davey, M. K., Hsieh, W. W., Wajsowicz, R. C., December 1983. The free Kelvin wave with lateral and vertical viscosity. J. Phys. Oceanogr. 13, 2182–2191.

Davis, T. A., 2003. A column pre-ordering strategy for the unsymmetric-pattern multifrontal method. Tech. rep., Dept. of Computer and Information Science and Engineering, Univ. of Florida, Gainesville, FL, USA, submitted to ACM Trans. Math. Software.

Davis, T. A., Duff, I. S., 1997. A combined unifrontal/multifrontal method for unsymmetric sparse matrices. Tech. rep., Computer and Information Science and Engineering Department, University of Florida.

Dobrindt, U., Mai 1999. Ein Inversmodell für den Südatlantik mit der Methode der finiten Elemente. Ph.D. thesis, Universität Bremen, (in german).

Dukowicz, J. K., 1995. Mesh effects for rossby waves. J. Comput. Phys. 119, 188–194.

Dukowicz, J. K., Smith, R. D., 1994. Implicit free-surface model for the Bryan-Cox-Semtner ocean model. J. Geophys. Res. 99 (C4), 7991–8014.

Ekman, V. W., 1905. On the influence of the earth's rotation on ocean currents. Arkiv för Matematik Astronomi och Fysik (Stockholm) 2 (11), 53pp.

FLAME Group, 1998. FLAME – A Family of Linked Atlantic Model Experiments, J. Dengg ed., AWI Bremerhaven, unpublished.

Gent, P. R., McWilliams, J. C., 1990. Isopycnal mixing in ocean circulation models. J. Phys. Oceanogr. 20, 150–155.

Gerdes, R., Köberle, C., Willebrand, J., 1991. The influence of advection schemes on the results of ocean general circulation models. Climate Dynamics 5, 211–226.

Gill, A. E., 1982. Atmosphere-Ocean Dynamics. Vol. 30 of International Geophysics Series. Academic Press.

Girault, V., Raviart, P.-A., 1986. Finite Element Methods for Navier-Stokes-Equations. Vol. 5 of Springer Series in Computational Mathematics. Springer.

Griffies, S. M., Böning, C., Bryan, F. O., Chassignet, E. P., Gerdes, R., Hasumi, H., Hirst, A., Treguier, A.-M., Webb, D., 2000. Developments in ocean climate modelling. Ocean Modelling 2, 123–192.

Hackbusch, W., 1993. Iterative Lösung großer schwachbesetzter Gleichungssysteme, second (1996) Edition. Vol. 69 of Leitfäden der angewandten Mathematik und Mechanik. B.G.Teubner.

Haidvogel, D. B., Beckmann, A., 1999. Numerical ocean circulation modelling. Vol. 2 of Series on environmental science and management. Imperial College Press.

Hallberg, R., Ozgokmen, T., Stephens, J., 2001. DOME - Dynamics of Overflow Mixing and Entrainment, idealized simulation specification, available at http://www.rsmas.miami.edu/personal/tamay/DOME/phase1-web.ps.gz.

Hallberg, R. W., 1995. Some aspects of the circulation in ocean basins with isopycnals intersecting the sloping boundaries. Ph.D. thesis, University of Washington, Seattle.

Hallberg, R. W., 1997. Stable split time stepping schemes for large-scale ocean modelling. Journal of Computational Physics 135, 54–65.

Hsieh, W. W., Davey, M. K., Wajsowicz, R. C., August 1983. The free Kelvin wave in finite-difference numerical models. J. Phys. Oceanogr. 13, 1383–1397.

Hughes, T. J. R., Franca, L. P., Hulbert, G. M., 1989. A new finite element formulation for computational fluid dynamics: Viii. the galerkin/least-squares method for advective-diffusive equations. Computer Methods in Applied Mechanics and Engineering 73, 173–189.

Iakovlev, N. G., 1996. A numerical model and preliminary results of calculations to reproduce the summer circulation in the Kara Sea. Izvestiya Atmos. Oceanic Phys. 32, 660–668, (Translated from Izvestiya AN, Fizika Atmosfery i Okeana).

Iskandarani, M., Haidvogel, D. B., Levin, J., 2003. A three-dimensional spectral element model for the solution of the hydrostatic primitive equations. Journal of Computational Physics 186, 397–425.

Johnson, C., 1990. Numerical solution of partial differential equations by the finite element method. Cambridge University Press.

Jungclaus, J. H., Hauser, J., Käse, R. H., 2001. Cyclogenesis in the Denmark Strait overflow plume. J. Phys. Oceanogr. 31, 3214–3229.

Kantha, L. H., Clayson, C. A., 2000. Numerical Models of Oceans and Oceanic Processes. Vol. 66 of International Geophysics Series. Academic Press.

Karypis, G., Kumar, V., 1998. Parallel threshold-based ILU factorization, available at:
http://www-users.cs.umn.edu/∼karypis/publications/Papers/PDF/pilut.pdf.

Käse, R. H., Girton, J. B., Sanford, T. B., 2003. Structure and variability of the Denmark Strait overflow: Model and observations. J. Geophys. Res. 108 (C6), doi:10.1029/2002JC001548.

Killworth, P. D., Edwards, N. R., 1999. A turbulent bottom boundary layer code for use in numerical ocean models. J. Phys. Oceanogr. 29, 1221–1238.

Kowalik, Z., Murty, T. S., 1993. Numerical Modeling of Ocean Dynamics. Vol. 5 of Advanced Series on Ocean Engineering. World Scientific.

Krauss, W., Käse, R. H., 1998. Eddy formation in the Denmark Strait overflow. J. Geophys. Res. 103, 15,525–15,538.

Lane-Serff, G. F., Baines, P. G., 1998. Eddy formation by dense flows on slopes in a rotating fluid. J. Fluid Mech. 363, 229–252.

Lane-Serff, G. F., Baines, P. G., 2000. Eddy formation by overflows in stratified water. J. Phys. Oceanogr. 30, 327–337.

LeBlond, P. H., Mysak, L. A., 1978. Waves in the ocean. Vol. 20 of Elsevier Oceanography Series. Elsevier Scientific Publishing Company.

Legrand, S., Legat, V., Deleersnijder, E., 2000. Delaunay mesh generation for an unstructured-grid ocean general circulation model. Ocean Modelling 2, 17–28.

LeProvost, C., 1986. On the use of finite element methods for ocean modelling. In: O'Brian, J. J. (Ed.), Advanced Physical Oceanographic Numerical Modelling. Vol. 186 of NATO ASI Series C: Mathematical and Physical Sciences. D. Reidel Publishing Company, pp. 557–580.

Lewandowski, R., 1997. Analyse Mathématique et Océanographie. No. 39 in Recherche en Mathématiques appliquées. Masson, Paris.

Lynch, D. R., Naimie, C. E., 1993. The M_2 tide and its residual on the outer banks of the Gulf of Maine. J. Phys. Oceanogr. 23, 2222–2253.

Marshall, J., Adcroft, A., Hill, C., Perelman, L., Heisey, C., 1997. A finite-volume, incompressible Navier Stokes model for studies of the ocean on parallel computers. J. Geophys. Res. 102 (C3), 5753–5766.

Mellor, G. L., 1996. Introduction to Physical Oceanography. Am. Inst. Phys. Press, New York.

Munk, W. H., 1950. On the wind-driven ocean circulation. J. Meteorol. 7, 79–93.

Myers, P. G., Weaver, A. J., 1995. A diagnostic barotropic finite-element ocean circulation model. J. Atm. Oceanic Technol. 12, 511–526.

Nof, D., 1983. The translation of isolated cold eddies on a sloping bottom. Deep-Sea Research 30 (2A), 171–182.

Olbers, D., Eden, C., 2003. A simplified general circulation model for a baroclinic ocean with topography. part I: Theory, waves, and wind-driven circulations. J. Phys. Oceanogr. 33 (12), 2719–2737.

Pacanowski, R. C., 1996. MOM2 documentation user's guide and reference manual. Tech. rep., GFDL Ocean Technical Report 3.2.

Pacanowski, R. C., Gnanadesikan, A., 1998. Transient response in a z-level ocean model that resolves topography with partial cells. Monthly Weather Review 126 (12), 3248–3270.

Pedlosky, J., 1987. Geophysical Fluid Dynamics, 2nd Edition. Springer.

Pedlosky, J., 1996. Ocean Circulation Theory. Springer.

Redi, M., 1982. Ocean isopycnal mixing by coordinate rotation. J. Phys. Oceanogr. 12, 1154–1158.

Roache, P. J., 1972. Computational Fluid Dynamics. hermosa publishers, Albuquerque N.M.

Saad, Y., 1996. Iterative Methods for Sparse Linear Systems. The PWS Series in Computer Science. PWS Publishing Company.

Salmon, R., 1998. Lectures on Geophysical Fluid Dynamics. Oxford University Press.

Sarkisyan, A. S., Ivanov, V. F., 1971. Joint effect of baroclinicity and bottom relief as an important factor in the dynamics of sea currents. Izw. Acad. Sci. USSR Atmos. Oceanic Phys. 7, 173–188.

Schmitz, W. J., Thompson, J. D., Luyten, J. R., 1992. The sverdrup circulation for the atlantic along 24^{circ}n. J. Geophys. Res 97, 7251–7256.

Schwarz, H. R., 1991. Methode der finiten Elemente, 3rd Edition. Vol. 47 of Leitfäden der angewandten Mathematik und Mechanik. B.G.Teubner.

Smith, R. D., Dukowicz, J. K., Malone, R. C., 1992. Parallel ocean circulation modeling. Physica D 60, 38–61.

Stommel, H. M., 1948. The westward intensification of wind-driven ocean currents. Trans. Am. Geophys. Union 29, 202–206.

Sverdrup, H. U., 1947. Wind-driven currents in a baroclinic ocean; with application to the equatorial currents of the eastern pacific. Proc. Natl. Acad. Sci 33, 318–326.

Thomasset, F., 1981. Implementation of Finite Element Methods for Navier-Stokes-Equations. Springer Series in Computational Physics. Springer.

UNESCO, 1981. Tenth report of the joint panel on oceanographic tables and standards. UNESCO Technical papers in Marine Sci. No. 36 -UNESCO, Paris.

Whitehead, J. A., Leetmaa, A., Knox, R. A., 1974. Rotating hydraulics of strait and sill flows. Geophysical Fluid Dynamics 6, 101–125.

Zienkiewicz, O. C., Taylor, R. L., 2000a. The Finite Element Method, 5th Edition. Vol. Vol. 1: The Basis. Butterworth Heinemann.

Zienkiewicz, O. C., Taylor, R. L., 2000b. The Finite Element Method, 5th Edition. Vol. Vol. 3: Fluid Dynamics. Butterworth Heinemann.

Acknowledgement

This thesis was written at Alfred Wegener Institute for Polar and Marine Research in Bremerhaven(AWI). The institute provided a sound background for the development of this work, including the chance for discussions on various scientific fields in an international community, computer facilities and opportunities to travel to conferences and summer schools.

Thanks to Prof. Dr. Dirk Olbers, who provided me with the opportunity of working at AWI, made many suggestions and gave helpful advices. I thank Prof. Dr. Wolfgang Hiller for being a reviewer of my thesis. Thanks to Prof. Dr. Jörn Bleck-Neuhaus, Prof. Dr. Alfred Schmidt, Dr. Matthias Prange and Torge Martin for being available for the defence of my thesis. My supervisor Dr. Jens Schröter was always available for fruitful discussions and comments. Dr. Sergey Danilov read all fragments of this work and I am very grateful for the insight I gained into various fields due to his explanations and patience. Also Dr. Gennady Kivman contributed much to my understanding of the finite element method. Dr. Stephan Frickenhaus from computing center helped a lot with the choice of appropriate solvers for sparse matrices which accelerated the work considerably. Concerning computer problems, issues and debugging Wolfgang Cohrs, Dr. Bernadette Fritzsch and Dr. Chresten Wübber were of great help. The same holds true for Dr. Martin Losch, a sparkling source of LaTeX, MATLAB and shell scripts, always interested in all sorts of questions. Dr. Carsten Eden from IfM Kiel provided me with his FLAME version together with the necessary namelists to run the comparison with $FEOM_0$. Additionally I profited from the experience Dr. Uwe Dobrindt had already gained in Finite Element modelling.

During the last years many people arrived in and left our "Arbeitsgruppe" but at all times the group provided an especially friendly atmosphere not only with respect to working. Besides people already mentioned there are Dr. Svetlana Losa, Dr. Lars Nerger, Dr. Christian Reick, Dr. Markus Schartau, Verena Seufer, Dr. Joanna Staneva, Dmitry Sidorenko and Dr. Manfred Wenzel responsible for this. Of course there were many more people not mentioned by name but nevertheless contributing much to the development of this work. I thank Dima and Ismael Núñez-Riboni for support and amusement in all kinds of work related and all kinds of not at all work related matters. It was a pleasure to spend after office hours filling offices with guitar music.